Numerical Investigation of the Performance and Flow Behaviour of Centrifugal Compressors

A Thesis Submitted to the University of Manchester for the Degree of Master of Philosophy in the Faculty of Engineering and Physical Sciences

2014

Yu Ang Wu

School of Mechanical, Aerospace and Civil Engineering

Contents

Abstract

Centrifugal compressor is of great importance in industries. High efficiency, high stage pressure ratio, wide operation range, easy to manufacture and easy to maintain make it prevalent in aerospace, automobile and power generation industries. The possibility in improving its efficiency has been pursued all the way along its path of development. Nowadays, energy-saving has been a key competitiveness for any power-consuming product. Dyson V2 centrifugal compressor is powered by a high speed electric motor, and provides suction power to the upstream cyclone separator to separate the dust particles from the air. It is highly desirable that the efficiency can be improved such that less electricity would be consumed. As the first step to improve its efficiency, it is essential to gain some knowledge on the flow phenomena involved, in essence, efficiency is the direct reflection of the quality of the flow field. The flow is viscous, highly unsteady, swirling and transitional inside Dyson V2 centrifugal compressor, strong interaction exists between different flow features, the compound effects of strong curvature, centrifugal force and Coriolis force make it very difficult to obtain an acceptable prediction. Theoretical approach is usually too ideal to take into account different flow features, experimental approach is too costly and generally time-consuming. With the rapid development of CFD techniques and the availability of high performance computers, computational approach is becoming one of the most popular tools during design and development phases.

In this work, computational approach has been employed to investigate the performance and the flow behaviour inside the Dyson V2 centrifugal compressor. Validation studies are first conducted to examine the capability of Star CCM+ solver, good agreements are obtained with the experimental data. After that, the flow field inside the Dyson V2 centrifugal compressor is analysed using steady simulation, which is relatively easy to conduct and feasible during the design phase. Different flow phenomena, including tip leakage flow, separation bubble, "jet-wake

structure" and corner separation are observed. Vortex roll-up process is identified, it is initialized near the impeller blade leading edge due to tip leakage flow, and grows in the axial part of the impeller, finally, it decays in the radial part of the impeller due to centrifugal force. A loss localization method is employed to identify the sources of significant loss generation, it is found that tip leakage flow is the most significant source of loss, it is initialized near the blade leading edge through vortex roll-up, and very difficult to control. The endwall loss and blade surface loss associated with boundary layer are significant near the impeller outlet and blade suction-side due to the high flow speed, corner separation induced loss in diffuser is also significant. Later, the effects of unsteadiness are investigated through unsteady simulation, it is shown that unsteadiness can help weaken or suppress flow separation and lead to reduced blockage and local loss generation. The impeller-diffuser interaction tends to slow down the high speed flow near the impeller blade suction-side and migrate the high speed flow from suction-side to pressure-side.

In literature, riblets have been extensively tested, although the physical mechanisms are not fully understood, it is definitely sure that riblets with proper size can help reduce the turbulent skin friction drag. In this work, riblets have been proposed to reduce the impeller hub endwall loss. However, riblets are of very small size, fully resolved simulation is extremely time-consuming and costly. Curve fitting is applied to correlate the available experimental data on riblets, an expression has been obtained to relate the wall shear stress reduction to non-dimensional spacing and yaw-angle. The riblets are designed and optimized based on the wall shear stress computed from steady simulation, the design value for wall shear stress reduction is around 4%. At the end, the riblets performance is assessed with unsteady simulation, it is confirmed that the riblets design based on steady simulation could perform very well, even under the effects of unsteadiness, a wall shear stress reduction around 4% could be achieved.

Acknowledgements

Declaration

No portion of the work referred to in this thesis has been submitted in support of an application for another degree or qualification of this or any other university or other institute of learning.

Restriction

This project is funded by Dyson Ltd., the Dyson V2 centrifugal compressor geometry and experimental results are supplied by Dyson, these materials are subjected to the confidential restrictions, and should not be distributed to public without the permission of Dyson Ltd.

Nomenclature

A	Area
C_b	Blade surface length
C_d	Dissipation coefficient
C_p	Pressure coefficient/Specific heat at constant pressure
C_{pd}	Base pressure coefficient
D	Diameter
D_H	Hydraulic diameter
div	Divergence
grad	Gradient
h	Height
I	Turbulence intensity
i	Internal energy
k	Thermal conduction coefficient/Turbulent kinetic energy
L	Length
l	Turbulence length scale
l_m	Mixing length
M	Mach number
$\dot{m}$	Mass flow rate
N	Rotational speed (rpm)
P	Power/Perimeter
p	Pressure
Q	Volume flow rate
Re	Reynolds number
Re_θ	Momentum thickness Reynolds number
r	Radius
$\dot{S}_a$	Total rate of entropy generation per unit area
s	Entropy/Spacing
T	Temperature
t	Thickness/Time
U	Rotational speed (m/s)
u_τ	Friction velocity
V	Absolute velocity
V_0	Blade surface velocity
W	Relative velocity
β	Clauser pressure gradient parameter
$β_2$	Backsweep angle
$γ$	Specific heat constant
δ	Boundary layer thickness
ε	Turbulent dissipation rate
$η$	Efficiency/Kolmogorov length scale
θ	Momentum boundary thickness

κ	Karman constant
μ	Dynamic viscosity
ν	Kinematic viscosity
ṽ	Eddy diffusivity
ξ	Entropy loss coefficient
ω	Rotational speed (rad/s)/Specific dissipation coefficient
ρ	Density
τ	Shear stress
τ_η	Kolmogorov time scale

Abbreviations

AW	Air Watt
CFD	Computational Fluid Dynamics
DNS	Direct Numerical Simulation
ERCOFTAC	European Research Community On Flow Turbulence and Combustion
FVM	Finite Volume Method
L2F	Laser-2-Focus
LA	Laser Anemometry
LES	Large Eddy Simulation
LSCC	Low Speed Centrifugal Compressor
MACE	Mechanical, Aerospace and Civil Engineering
PS	Pressure-Side
PIV	Particle Image Velocimetry
PJSW	Pressure-side Jet and Suction-side Wake
PWSJ	Pressure-side Wake and Suction-side Jet
RANS	Reynolds Averaged Navier-Stokes equations
RSM	Reynolds Stress Model
SA	Spalart Allmaras
SGS	Sub-Grid Scale
SS	Suction-Side
SST	Shear Stress Transport
TS	Tollmien-Schlichting

Superscripts and Subscripts

c	Cross-stream/Compressor
m	Main stream
r	Radial component
s	Static condition
t	Stagnation condition
w	Wake
θ	Tangential component
0	Stagnation condition
1	Impeller inlet
2	Impeller outlet/Diffuser inlet

3	Diffuser outlet
+	Non-dimensional quantity
*	Relative stagnation condition

List of Figures

Chapter 1

Chapter 2

Chapter 3

Chapter 4

Chapter 5

Chapter 6

Chapter 7

Chapter 8

Appendix A

Appendix B

List of Tables

Chapter 1

Introduction

1.1. Background

Turbomachine is a rotary device that exchanges energy with the working fluid through blade rotation. According to either extracting or adding energy, turbomachine can be broadly classified into two categories, turbine and compressor (air) or pump(water) respectively.

Turbomachine has gone through a slow and long process of development. The steam engine designed by the Heron of Alexandria is probably one of the first turbomachines, as shown in Figure 1- 1, the steam goes out from the ball as two opposite oriented jets, thus propelling force is produced from the conservation of momentum. Other forms of early turbomachinery application are windmills and waterwheels, which extract energy from wind and moving water respectively, then the retrieved energy can be applied to grind grain and pump water. Nowadays, some of them are still in operation and mainly for tourism purpose.

Human beings technologies develop rapidly, and most of them are power demanding, nowadays, more energy is required than ever before. Some of the most common turbomachines are gas turbine engine onboard aircraft (Figure 1- 2), hydraulic turbine in the dam, Dyson V2 centrifugal compressor in a Dyson handheld vacuum cleaner (Figure 1- 3), turbocharger inside a car, and even the heart pumps implanted in human body. Extensive research has been conducted on turbomachinery efficiency improvement, nowadays, the efficiency of large

turbomachine can reach as high as 97% (hydraulic pump), while that of small turbomachine is still relatively low, about 70%. The problem encountered by the small turbomachine is that the flow is subject to strong curvature, centrifugal force and Coriolis force, and the small cross-sectional area constrains the flow, as a result, the flow behaviour is very complicated, strong interactions exist between different flow features, what's worse, the small size makes the application of flow control devices prohibited. Flow features such as viscous, unsteady, three-dimensional, transitional and strong interaction make it difficult to obtain a reliable prediction, some of the physical mechanisms are still poor understood.

Figure 1- 1: Heron's steam rotor (Fransson, Hillon and Klein, 2000).

Figure 1- 2: Rolls-Royce Trent 1000 onboard a Boeing 787 dreamliner during flight.[1]

Figure 1- 3: Dyson V2 digital motor.[2]

Being used to efficiently transfer energy to the working fluid in the form of raised pressure level, compressor has been widely employed in aerospace, power generation and process industries. Various types of compressor exist, each suitable for a specific application. Axial flow compressor is capable of working with large amount of working fluid at one time with relatively small frontal area, which is very critical in aerospace application (drag consideration), although the stage pressure ratio is low, multi-stage arrangement could achieve overall pressure ratio as high as 40:1. In contrary, centrifugal flow compressor can only handle a limited amount of working fluid, while it can achieve stage pressure ratio as high as 8:1, majorly due to the contribution from the centrifugal force. A compromise between flow capacity and pressure ratio brings us to the mixed flow compressor. Figure 1- 4 presents a sketch of different types of compressors.
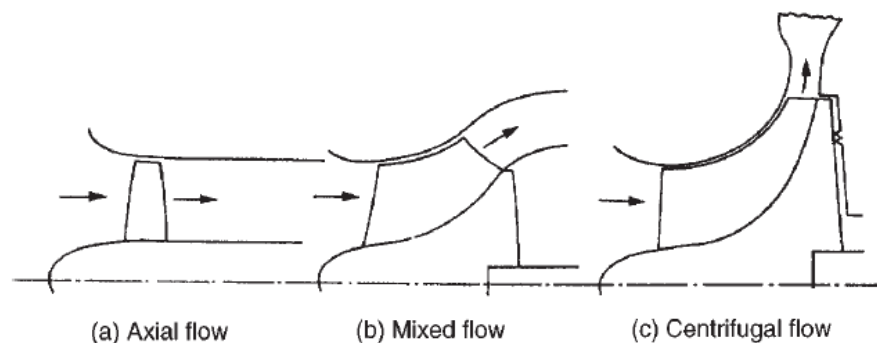
Figure 1- 4: Different types of compressors (Dixon, 2010).

Turbomachine has been an integral part of our life, wide application and power-consuming make it stringent to improve its efficiency. Tremendous amount of

efforts have been expended to improve the turbomachinery efficiency, and it will continue in the foreseeable future. Centrifugal compressor, as a kind of turbomachine, has evolved from low efficiency, poor designed to high efficiency, 3D well designed machine, however, small centrifugal compressor is still of relatively low efficiency due to its inherent complex flow interaction. So it is essential to understand the flow behaviour involved. Recently, Computational Fluid Dynamics (CFD) gains its popularity in both research and engineering design due to its relatively low cost, short return cycle and the capability in revealing more flow features compared to theoretical and experimental approaches. The development of CFD techniques enables the designer to have a more comprehensive view on the flow behaviour involved and the general performance.

1.2. Motivation and Objectives

Dyson V2 centrifugal compressor is a well designed small size centrifugal compressor. It is equipped inside a Dyson handheld vacuum cleaner to provide suction power to the cyclone separator, which is designed to separate dust particles from air stream. A schematic is given in Figure 1- 5. It will be beneficial to have improved suction power efficiency, as the first step, it is of great importance to understand the flow behaviour inside and to explore the possible ways to reduce the loss generation.
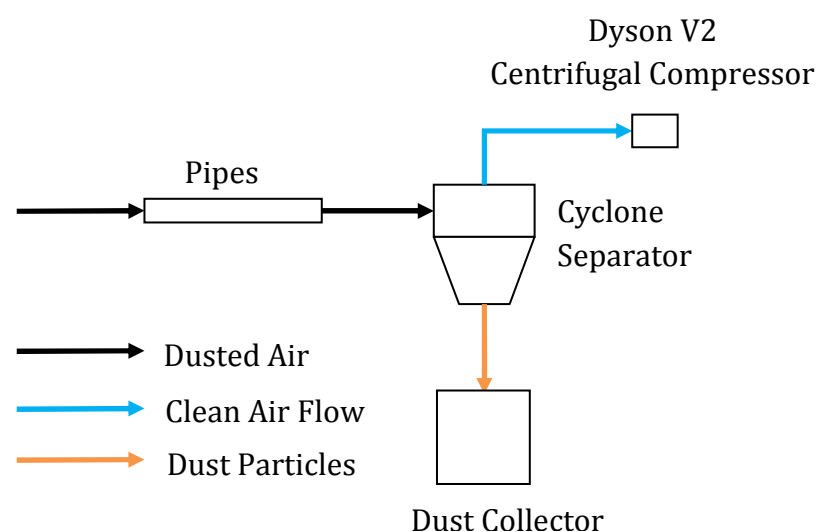
Figure 1- 5: Schematic of Dyson Vacuum Cleaner System.

The objectives of this work is to analyse the performance and flow behaviour of Dyson V2 centrifugal compressor, find regions of high loss and investigate the effect of unsteadiness, at the end, it is thus possible to provide methods for improving the Dyson V2 centrifugal compressor performance.

1.3. Outline of Thesis

The whole thesis is subdivided into several chapters.

Chapter 2 intends to introduce the basic compressor theory, including the performance characteristics, commonly observed flow phenomena and sources of loss generation, after that, the existing experimental and numerical works on centrifugal compressor are reviewed. At the end, riblets, as a kind of passive flow control devices, have been surveyed and reviewed in details.

Chapter 3 introduces the turbulence modelling materials, at the beginning, the Navier-Stokes equations and RANS are described, then different RANS models are discussed and compared as well as the corresponding formulations.

Chapter 4 describes the method of investigation for this work, first of all, the assumptions made in this work are given as the basis for the following studies. Then a brief introduction to the turbomachinery modelling techniques is provided, followed by the discussion on grid generation and numerical conditions. At the end, the loss localization method is introduced, with the explicit expressions, it is possible to identify regions of high local loss generation.

The solver validation is given in Chapter 5, experimental data are available for Dyson V2 centrifugal compressor and ERCOFTAC centrifugal compressor with regard to performance and flow field respectively. Single passage steady simulation is conducted for performance validation with Dyson V2 centrifugal compressor, while full annulus unsteady simulation is performed for flow field validation with ERCOFTAC centrifugal compressor.

Detailed flow field analysis on Dyson V2 centrifugal compressor is conducted in Chapter 6 using steady simulation. The general flow behaviour with regard to the performance is presented, distinct flow features are identified. Loss localization

method has been applied to spot regions of high local loss generation, the important sources of loss generation are identified. Wall shear stress distribution and hub skin friction lines are obtained and will be used for riblets design in chapter 8.

In chapter 7, full annulus unsteady simulation is performed, the effect of unsteadiness on Dyson V2 centrifugal compressor performance and flow field is discussed. Particular attention has been paid to the variation in wall shear stress on hub, this information will be used in chapter 8 to assess the riblets performance under the effects of unsteadiness.

Chapter 8 presents some further discussions on the application of riblets, including operation regimes, optimization and yaw-angle effect. An explicit expression has been obtained by conducting curve fitting on experimental data to relate the wall shear stress reduction to the non-dimensional spacing. Later, riblets are proposed to be applied to the Dyson V2 impeller hub to reduce the hub endwall loss, steady simulation results are used to design the riblets, at the end, the riblets performance is assessed using unsteady simulation.

Finally, conclusions are drawn in chapter 9, discussions on future work are also made to shed light on possible further developments in the future.

Chapter 2

Literature Review

2.1. Introduction

In this chapter, a brief introduction to the compressor theory will be given at first, including the general performance characteristics and centrifugal compressor components, the typical flow phenomena occurred in centrifugal compressor and loss generation, with emphasis on centrifugal compressor with unshrouded impeller and vaned diffuser. After that, existing works on centrifugal compressor are discussed to shed light on the current status of research on centrifugal compressor, including both experimental and numerical approaches. At the end, riblets surface is introduced as a passive flow control method, existing works on riblets performance in case of flat plates, pipes and compressors are also reviewed.

2.2. Centrifugal Compressor Fundamentals

2.2.1. Compressor Performance

Compressor is an equipment to increase the energy of the working fluid, its performance has to be assessed according to several general performance parameters, such as isentropic efficiency, pressure ratio, operation range, pressure coefficient and etc, details are given as follows.

Isentropic Efficiency

Isentropic efficiency is a parameter relating the real process to the ideal isentropic process, which is free from heat transfer and loss, it characterizes how much entropy has been generated due to the loss(irreversibility) for the real process. Depending on whether the exhaust has been utilized or not, the isentropic efficiency can be classified into two subcategories, total-to-total isentropic efficiency(Eqn 2-1) and total-to-static isentropic efficiency(Eqn 2-2) respectively. The former is applied if the exhaust is used to produce further work, such as that for aircraft gas turbine engines, conversely, in the case of gas turbine in power generation station, the exhaust discharges into the atmosphere(in some cases, the exhaust is used for heating in houses) directly, the latter should be applied.

$$\eta_{t,t} = \frac{1 - \left(\frac{p_{t,2}}{p_{t,1}}\right)^{\frac{\gamma-1}{\gamma}}}{1 - \frac{T_{t,2}}{T_{t,1}}} \qquad \text{Eqn 2- 1}$$

$$\eta_{t,s} = \frac{1 - \left(\frac{p_{s,2}}{p_{t,1}}\right)^{\frac{\gamma-1}{\gamma}}}{1 - \frac{T_{t,2}}{T_{t,1}}} \qquad \text{Eqn 2- 2}$$

Pressure Ratio

Compressor works to increase the static and total pressure of the working fluid, therefore, static and total pressure ratios are important performance parameters, however, higher static or total pressure ratio does not necessarily mean higher work output, which depends on the specific performance parameter for certain application. In the case of a reasonably well designed impeller, both static and total pressure of the working fluid at the outlet should be increased compared to those at inlet, the static pressure would also increase for diffuser due to the diffusion process, however, the total pressure would reduce for diffuser due to losses and lack of work input.

Operation Range

In most cases, compressor would not work at a fixed operation condition, instead, it will operate at different mass flow rates and speeds according to the loading condition and application, these make the compressor a rather dynamic machine, generally, it should possess high efficiency at a variety of operation conditions. More importantly, it has to be able to withstand sudden unstable inflow conditions and restore the original state as soon as possible.
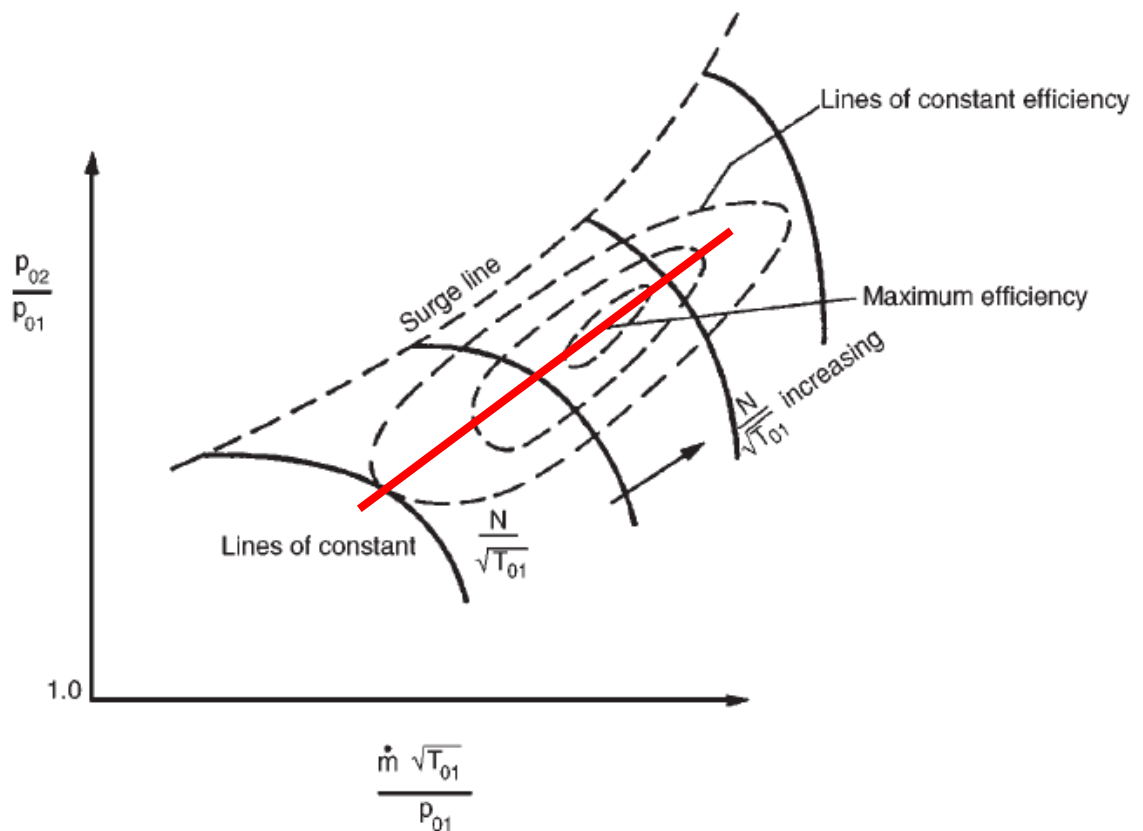
Figure 2- 1: Performance characteristic of a compressor (Dixon, 2010).

The whole operation could be summarised in a performance map(as shown in Figure 2- 1), with which some of the operation conditions could be described easily, the lines of constant efficiency are in the form of closed curves, which could be called the efficiency islands. Referring to Figure 2- 1, the compressor should work at the maximum efficiency point at the design operation condition, ideally, the operation path should pass through the peak efficiency point, as denoted by the red

line. At the design operation condition, the inlet flow should be well matched to the blade leading edge and go smoothly along the blade, as shown in part (a) Figure 2-2, the streamlines are shown in the rotating reference frame. Referring to part (b) Figure 2- 2, if the mass flow rate at the inlet is increased, while the rotation speed is kept constant, the blade incidence angle would reduce considerably, and the inlet and outlet velocity will be increased, thus lead to reduced static pressure, continuous increase in mass flow rate at inlet would bring the impeller to choke condition, for which the flow will reach the speed of sound at the throat, as a result, further increase in mass flow rate inside the impeller is not achievable. In contrary, a decrease in inlet mass flow rate at constant speed would reduce the inlet velocity, near leading edge separation may happen and cause stall (part (c), Figure 2- 2), the loss increases dramatically, more seriously, the compressor surge would occur and bring significant impact on the performance, stability and the blade life.

Pressure Coefficient

The pressure recovery coefficient is generally applied to assess the diffuser performance, it describes to what extent the diffuser inlet dynamic pressure could be converted into static pressure. Therefore, it is formally defined as the ratio of static pressure rise to diffuser inlet dynamic pressure, as given in Eqn 2-3.

$$C_{pr} = \frac{p_3 - p_2}{p_{t,2} - p_2}$$ Eqn 2- 3

Similarly, the pressure loss coefficient can be defined as:

$$C_{pl} = \frac{p_{t,2} - p_{t,3}}{p_{t,2} - p_2}$$ Eqn 2- 4

Suction Power

The general performance parameters has been introduced, there is one more application specific performance parameter has to be introduced. The Dyson V2 centrifugal compressor is equipped inside a Dyson handheld vacuum cleaner, for
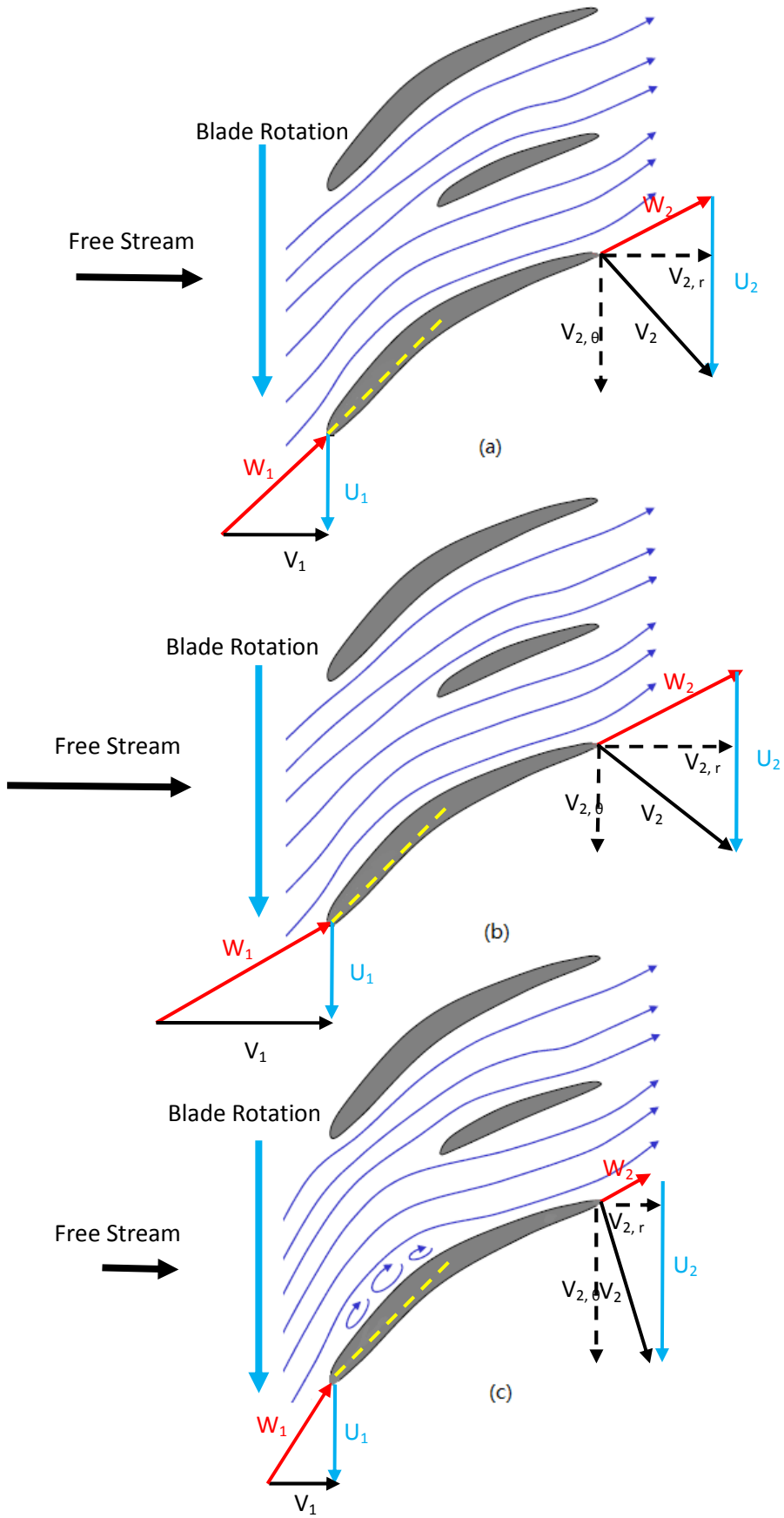
Figure 2- 2: General compressor flow streamline with velocity triangle.

which the suction power is the most critical performance parameter for determining suction capability. Suction power is defined as the product of total-to-static pressure rise and volume flow rate (as shown in Eqn 2-5), the suction power efficiency is also defined accordingly (Eqn 2-6).

$$P_{suc} = (p_{s,2} - p_{t,1}) \times Q \qquad \text{Eqn 2- 5}$$

$$\eta_{suc} = \frac{P_{suc}}{P_{tot}} \qquad \text{Eqn 2- 6}$$

Euler Work Equation

From the fundamental thermodynamic principle, it is possible to estimate the thermodynamic process happened inside a centrifugal compressor. The Euler work equation can be derived from steady flow energy equation and the conservation of angular momentum, as given in Eqn 2-7. Referring to Figure 2- 2, the Euler work is significantly less when the compressor operates at near choke condition, and the total pressure ratio is lower according to Eqn 2-9, while at the stall condition, the Euler work is much larger, as well as the total pressure ratio. An alternative form can reveal more physics involved in the energy transferring process, it is written as Eqn 2-8, the first term on the RHS, $1/2(V_2^2 - V_1^2)$, is the increase in absolute kinetic energy of the working fluid, this part of energy is not used by the impeller itself (used by diffuser), so it is also called external effect. On the other hand, the second and third terms relate the thermal process within the impeller, so they are termed the internal diffusion effect. More specifically, the second term, $1/2(U_2^2 - U_1^2)$, represents the increase in kinetic energy due to centrifugal effect, compared to axial compressor, centrifugal compressor has additional contribution from centrifugal force, which enables it to have much higher stage pressure ratio, and the third term, $1/2(W_1^2 - W_2^2)$, denotes the decrease in relative kinetic energy due to the effect of pure diffusion.

$$\Delta W_c = V_{\theta,2}U_2 - V_{\theta,1}U_1 \qquad \text{Eqn 2- 7}$$

$$\Delta W_c = \frac{1}{2}[(V_2^2 - V_1^2) + (U_2^2 - U_1^2) + (W_1^2 - W_2^2)] \qquad \text{Eqn 2- 8}$$

If there is no heat transfer and irreversibility (isentropic process), the isentropic total pressure rise could be related to stagnation temperature change. For a centrifugal compressor impeller with no-swirl inlet flow, the isentropic total-to-total pressure ratio can be expressed as Eqn 2-9.

$$\frac{p_{t,2}}{p_{t,1}} = \left(\frac{T_{t,2}}{T_{t,1}}\right)^{\frac{\gamma}{\gamma-1}} = \left(1 + \frac{V_{\theta,2}U_2}{C_p T_{t,1}}\right)^{\frac{\gamma}{\gamma-1}} \qquad \text{Eqn 2- 9}$$

Similarly, with the assumption of isentropic process, the total pressure should be constant throughout the diffuser. So the stage isentropic total pressure ratio is exactly the same as that of impeller, as given by Eqn 2-9.

2.2.2. Impeller

The impeller is the rotating component inside a centrifugal compressor, sometimes, it is also called the compressor wheel. Generally, it consists of a number of blades with complex profile and curvature, and mounted to the hub. The working fluid is accelerated to extremely high speed in the impeller, and flung outward with centrifugal force and Coriolis force produced due to rotation. The impeller design is critical, it determines whether or not the energy could be efficiently transported to the working fluid. Impeller can be further divided into two seamlessly merged sections, inducer and exducer respectively. Inducer is the axial section of the impeller, for which it largely determine the maximum flow capability. Exducer, on the other hand, is the radial section of the impeller, it limits the ability to accelerate the air at a given shaft speed.

Impeller could be categorized according to the types of blading, namely forwardswept, radial and backswept blade impeller, they are illustrated in Figure 2- 3 with outlet velocity triangles. The backswept impeller produces less Euler work at given shaft speed, but it has wider operation range and better stability, and it is usually required to operate at high speed. In contrast, the forwardswept impeller produces much higher Euler work, however, its operation range is limited due to the high outlet air speed and small flow angle, it is usually applied where high pressure ratio is required.
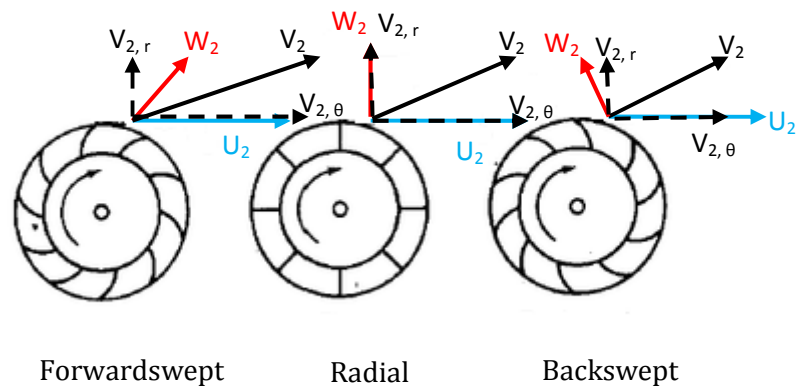
Figure 2- 3: Different types of impeller blading.

The impeller blade can be also categorized into shrouded and unshrouded types, shrouded impeller tends to have higher stress on the blade, thus requires stronger blade structure, which would undoubtedly increase the weight and limit the shaft speed to low level. Severe back flow can be observed in the clearance between the shroud and casing due to the pressure gradient between outlet and inlet. While unshrouded impeller is more common in recent designs, 3D blade can be relatively easier to incorporate, thus could improve the efficiency considerably. However, unshrouded impeller is prone to tip leakage flow, the interaction is much more complex, thus impact the efficiency. A trade-off study has to be conducted by the designer to determine the appropriate design for the specific application.

2.2.3. Diffuser

The air flow is of very high speed at the outlet of impeller, generally, almost half of the shaft power has been expended to raise the speed of the air. So it is of practical importance to use this part of energy, to serve this purpose, diffuser can be arranged downstream of the impeller to recover the otherwise wasted energy. The recovery is in fact a diffusion process, for which the flow has to be slowed done appropriately, otherwise, severe separation may present and cause deterioration in performance. The diffusion process can be completed with either vaneless diffuser or vaned diffuser, the former diffuses the flow by increasing the radius solely, while the latter employs the double effect of increasing radius and flow turning by vane curvature. Vaneless diffuser is subject to high skin friction loss and generally of low efficiency, while the operation range is very wide. Vaned diffuser, as a means to

improve the efficiency, is very sensitive to flow condition, the operation range is rather limited due to possible stall inception at the diffuser blade. On the other hand, the presence of vaned diffuser will cause impeller-diffuser interaction, which tends to distort the flow field significantly, the optimum spacing between the impeller blade and diffuser blade is a critical design parameter, which need to be determined carefully, otherwise severe loss can occur, and the compressor performance will be severely impacted.

2.2.4. Compressor Flow Phenomenon

Compressor flow behaviour is very complicated, viscous, highly unsteady and transitional, several flow patterns co-exist, some of them interact with each other, strong interactions exist in small size compressors in particular. Only some of the important flow behaviour will be introduced here, such as leading edge vortex, laminar separation bubble, tip leakage flow and etc, looking deep into any single flow phenomenon would take a lot of efforts, a comprehensive description is out of the scope of the current work. Therefore, an introductory description is given in this section, and a brief review will be given in section 2.3.

Leading Edge Vortex

It is well known that vortex shedding occurs in the case of flow around a cylinder, a horseshoe vortex is shed from the cylinder with two legs, and transported downstream. The underlying mechanism is supposed to be that the vortex rolls up under the induced adverse pressure gradient near the stagnation point. Similarly, the leading edge vortex is commonly observed in the wing-body junction situation, a special case is the blade-hub junction inside a centrifugal compressor. A illustration of the vortex system in a compressor passage is shown in Figure 2- 4, the leading edge vortex has two legs, pressure-side leg and suction-side leg respectively. The pressure-side leg tends to be convected towards the suction-side due to the secondary flow caused by pressure gradient between these two sides. Pressure-side leg and suction-side leg may interact with each other, and create even more complex vortex system inside the passage.
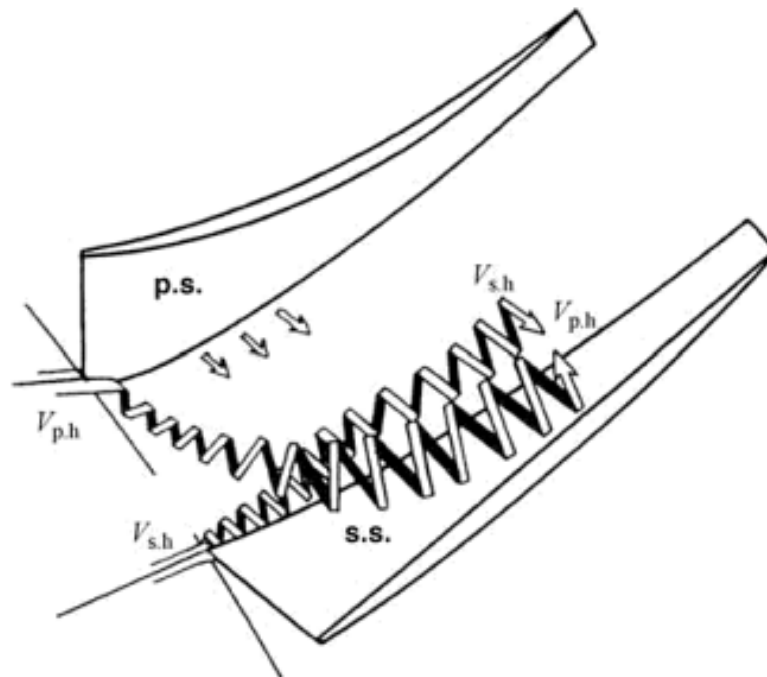
Figure 2- 4: Pressure-side and suction-side legs of horseshoe vortex (Chen, Papailiou and Huang, 1999).

Laminar Separation Bubble

In case of low Reynolds number flow, the flow may be laminar at the beginning, laminar-turbulent transition will occur at some point before the flow becoming fully turbulent. Transition is a very difficult and broad research topic, although a vast amount of efforts have been expended on it, the physical mechanism is still not fully understood at this moment, three different types of transition exist in literature, natural transition, bypass transition and separation induced transition respectively. Natural transition seldom happens inside a compressor, instead, bypass transition is common due to the high turbulence level at the inlet, and laminar separation bubble would appear in the case of low Reynolds number flow.

Laminar separation bubble is usually caused by the strong adverse pressure gradient, which could happen due to large local curvature near the blade leading edge. The initial laminar boundary layer cannot sustain the adverse pressure gradient, hence separates from the wall. The separated laminar flow is very sensitive to disturbances, and goes through transition to turbulent flow, if the transition point is close enough to the wall, the relatively high momentum

turbulent flow may reattach to the wall and forms a laminar separation bubble, otherwise the turbulent flow may not be able to reattach the wall, and thus causes complete separation of the flow. Figure 2- 5 illustrates the formation of laminar separation bubble, as indicated by the circulation zone.
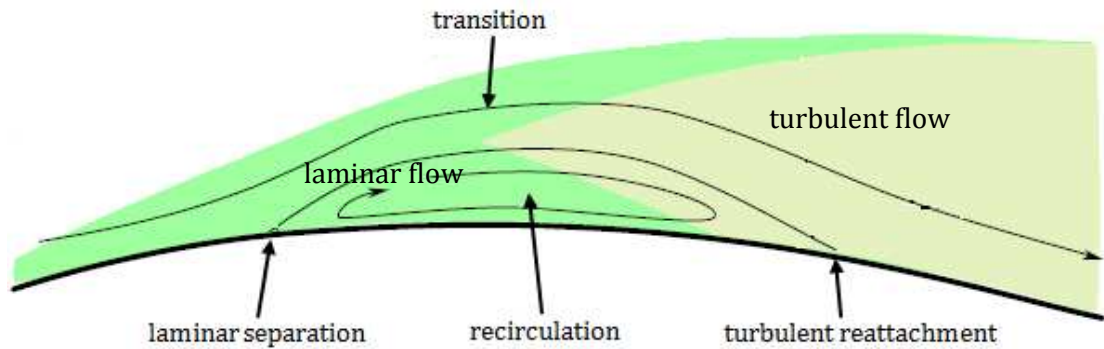
Figure 2- 5: Laminar separation bubble formation process.

Tip Leakage Flow

Tip leakage flow exists in both unshrouded and shrouded impeller due to the existence of unavoidable tip clearance between the blade tip/shroud and the casing. For the unshrouded impeller, the tip leakage flow is induced by the pressure difference between the suction-side and pressure-side of the blade, the flow leaks from the pressure-side to the suction-side under the pressure gradient, while in the case of shrouded impeller, tip leakage flow occurs due to the pressure difference between the blade trailing edge and leading edge, and exists inside the clearance between the shroud and casing. In centrifugal compressor, centrifugal force and Coriolis force also contribute to the tip leakage flow, however, the resultant effect is very complicated and varies for different impeller blading (forwardswept, radial or backswept). The leakage flow rate can be estimated with the pressure difference and contraction ratio, which is defined to take into account the contraction of the flow area due to blockage inside the clearance.

Tip leakage flow is always described as a source of disadvantage to the compressor performance, it can affect the compressor in different ways, first of all, the tip leakage flow produces significant loss regions near the blade tip, secondly, blockage can be created in the passage core region due to the separation and vortex roll-up.

A schematic on the unshrouded impeller tip leakage flow is presented in Figure 2- 6, the leakage flow behaves differently for blades with different blade thickness to tip clearance ratios (t/h). As proposed by Denton(1993), the leakage flow will separate from the pressure-side corner and reattach the blade tip inside the tip clearance if the aforementioned ratio t/h is greater than 4, otherwise, the leakage flow will separate and leak to the suction-side without reattachment.
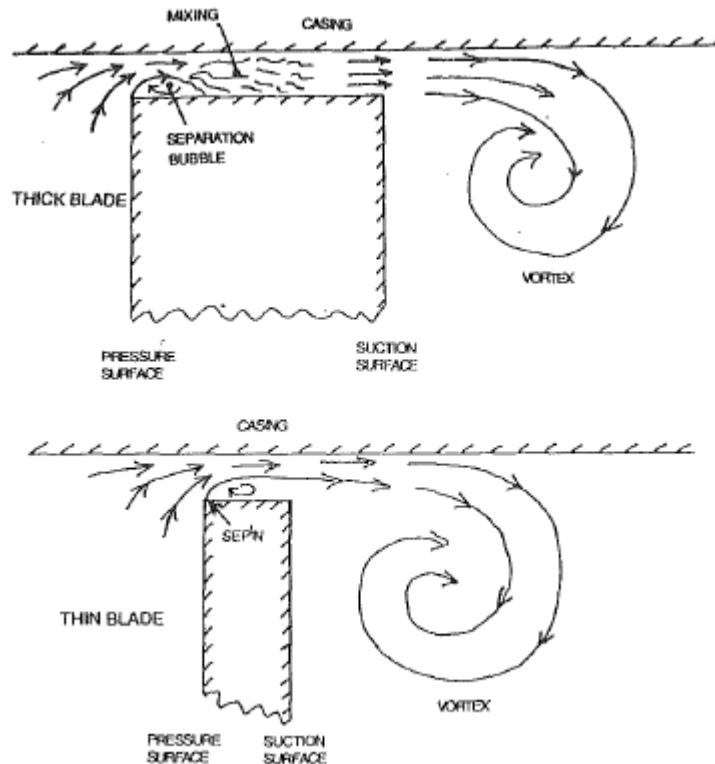
Figure 2- 6: Tip leakage flow for an unshrouded impeller (Denton, 1993).

Impeller-Diffuser Interaction

Impeller-diffuser interaction is the interaction between the rotating impeller blade and the downstream stationary diffuser blade, it does not happen inside a centrifugal compressor with vaneless diffuser. Two different interaction mechanisms exist, namely potential effect and viscous effect. If the diffuser blades are placed relatively far away from the impeller blade, the potential effect would dominate the impeller-diffuser interaction, and help to reduce the inflow non-uniformity at the diffuser inlet, while the viscous loss is relatively low, as a result, the gain from the potential effect may exceed the viscous loss, and thus bring

positive effect on the diffuser performance. On the other hand, if the spacing between the diffuser blade and the impeller blade is reduced too much, the viscous loss would increase to a very high level and overweighs the gain from the potential effect, thus deteriorates the diffuser performance. Except for the aforementioned effects on diffuser, impeller-diffuser interaction can also affect the performance of the upstream impeller in the form of unsteady loading, or even possibly initialize the stall inception. A careful investigation into the impeller-diffuser interaction has to be done by the designer to achieve better performance and higher operation stability for the compressor.

Jet-Wake Structure

Jet-wake structure is commonly observed at the impeller outlet, very similar to the mixing of parallel flows. It usually represents the non-uniform discharge flow at the impeller outlet due to the boundary layer development, tip leakage flow, centrifugal force, Coriolis force and strong curvature. In the case of vaned diffuser, the diffuser blade induced adverse pressure gradient will also affect the formation and characteristics of the jet-wake structure. Figure 2- 7 shows two types of "jet-wake structure" at the impeller outlet, Pressure-side Jet & Suction-side Wake(PJ&SW), Pressure-side Wake & Suction-side Jet(PW&SJ), respectively, in literature, other variants were also observed and only differed slightly.
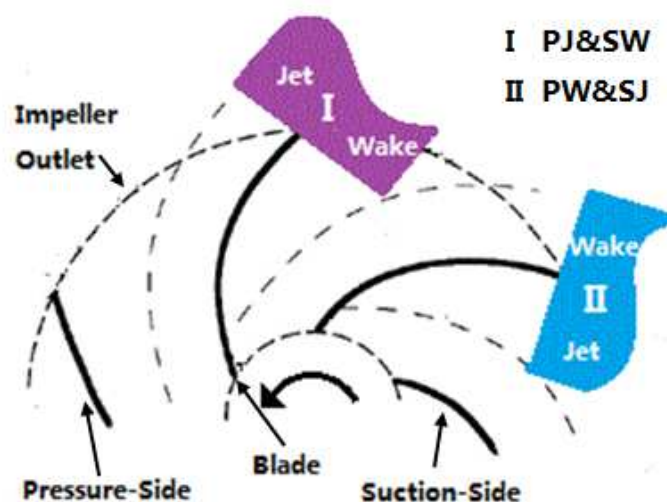
Figure 2- 7: Two types of jet-wake structures at impeller outlet.

Secondary Flow

In a broad sense, secondary flow is defined as the flow has its direction different from that of the main stream, the so called streamwise direction. It is a highly undesirable while common flow phenomenon inside a compressor passage. High loss and potential blockage are always associated with it. Figure 2- 8 illustrates the presence of secondary flow inside a compressor passage, major sources of secondary flow are the pressure gradient between the pressure-side and suction-side of the blade and the relative motion between casing and the impeller, majorly occurs inside the endwall boundary layers, other sources of secondary flow are the 90 deg bend of the flow passage from axial to radial direction, centrifugal force and Coriolis force for a centrifugal compressor.
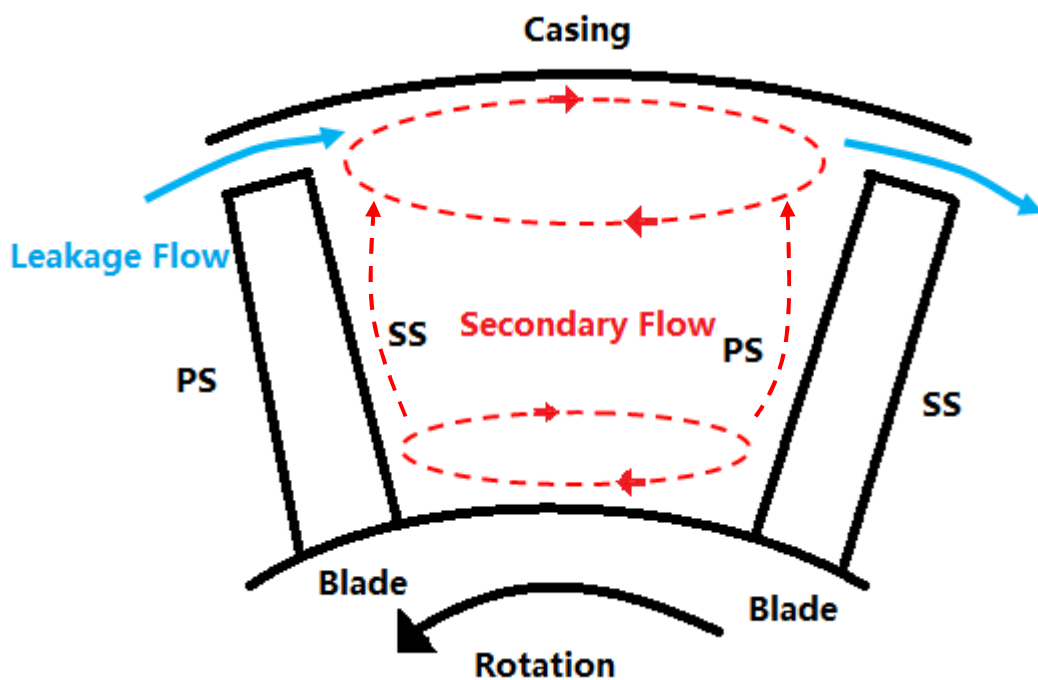
Figure 2- 8: Secondary flow in cross section normal to streamwise direction.

2.2.5. Losses in Compressor

In thermodynamics, entropy indicates the irreversibility of the thermodynamic process, it can only increase in nature. The loss in turbomachinery can be characterized by the entropy generation. Most of the past works have been concentrated on the modelling of the entropy generation, different models were

proposed to evaluate the entropy generation for different situations, such as two-dimensional boundary layer, fluid mixing, heat transfer and shock wave. A brief introduction on the major sources of losses is given as follows, some of the theoretical models are also described to help understanding the physical aspects. Please refer to Denton (1993) for a comprehensive review.

Entropy Generation

Entropy has been described by Denton (1993) as "smoke", which would be created where the flow undergoes an irreversible process. It cannot be destroyed and can only be convected downstream. Entropy can be generated due to different physical mechanisms, such as viscous effect, heat transfer and nonequilibrium process. In the case of compressor, the entropy generation due to heat transfer is generally of negligible level, however, strong coolant flow involved in turbines makes heat transfer a very significant mechanism of entropy generation and need to be considered with care. Nonequilibrium process, such as sudden expansion and shock wave, is very important, but it is not that relevant in the context of current work. Therefore, only entropy generation due to viscous effect will be discussed below.

Compressor flow is in fact a wall bounded flow, under the effect of diffusion, the boundary layer is very thick, thus imply high viscous dissipation involved. An expression has been derived by Denton (1993) to calculate the total rate of entropy generation for a two-dimensional boundary layer, as given in Eqn 2-10, the total rate of entropy generation per unit surface area is directly proportional to the shear stress, and can be obtained by integration through the boundary layer. From the calculation with boundary code developed by Cebeci and Carr (1978), Denton found that much of the entropy was created within the laminar sublayer and the logarithmic region. For practical use, it is usually more convenient to turn the entropy generation to a dimensionless dissipation coefficient, as defined in Eqn 2-11, where V_δ denotes the velocity at the edge of the boundary layer.

$$\dot{S}_a = \frac{d}{dx}\int_0^\delta \big(\rho V_x(s - s_\delta)\big)dy = \int_0^\delta \frac{1}{T}\tau_{yx}dV_x \qquad \text{Eqn 2- 10}$$

$$C_d = \frac{T\dot{s}_a}{\rho V_\delta^3} \qquad\qquad \text{Eqn 2- 11}$$

Schlichting (1966) correlated the experimental results and concluded that the dissipation coefficient for turbulent boundary layers is relatively insensitive to the state of the boundary layer. Denton (1993) compared the dissipation coefficient from Schlichting with that from Cebeci and Carr, and drew similar conclusions as Schlichting, further investigations on the dissipation coefficient for laminar boundary layer were conducted, it was found that the dissipation coefficient is sensitive to the state of the boundary layer, and the dissipation coefficient for laminar boundary layer is much less than that for turbulent boundary layer with Re_θ ranging from 300 to 500, which represents the transition region, thus pointed out the importance of transition prediction in loss estimation.

Another significant source of entropy generation due to viscous effect is the shear flow, the most common shear flows in turbomachinery are tip leakage flow and wake. Since there flows are generally turbulent and of high effective viscosity, what's worse, they are usually highly complex, thus make it very difficult to quantify the local entropy generation. However, the global entropy generation can be obtained relatively easily, as described by Denton (1993), a control volume method can be applied to predict the entropy generation, thus the mixing loss can be estimated without losing much accuracy, the upstream conditions are assumed to be known, and the downstream conditions are set to those of far downstream, for which the flow parameters restore to uniform conditions. A representative example of such mixing process is given by Denton, it is the mixing of two streams. With the assumption that one of the two streams is small, a simplified version is demonstrated by Denton, while the relevant theory was first proposed by Shapiro (1953). A schematic is shown in Figure 2- 9, where V_c is the cross-stream velocity, and α denotes the cross-stream angle. The entropy generated in this process can be expressed as Eqn 2-12 (for main stream), where the subscript c, m and t denote the cross-stream, main stream and stagnation condition respectively. C_p denotes the specific heat at constant pressure, M denotes the Mach number. A simplified expression can be obtained if the two streams have the same stagnation temperature, as Eqn 2-13. Eqn 2-12 and Eqn 2-13 are valid for both constant

pressure and constant area mixing. Denton suggested that the total entropy generation does not depend greatly on area and pressure through simple derivations. Referring to Eqn 2-13, it can be inferred that the total entropy generation rate is directly proportional to the velocity difference in the main stream direction. Further investigation on wake entropy generation was also conducted by Denton, the interested reader is referred to Denton (1993) for more details.

$$\Delta s = C_p \frac{m_c}{m_m}\left\{\left(1 + \frac{\gamma-1}{2}M_m^2\right)\frac{T_{t,c}-T_{t,m}}{T_{t,m}} + (\gamma-1)M_m^2\left(1 - \frac{V_c\cos\alpha}{V_m}\right)\right\} \quad \text{Eqn 2- 12}$$

$$Tm_m\Delta s = T\dot{S} = m_c(V_m^2 - V_m V_c \cos\alpha) \quad \text{Eqn 2- 13}$$
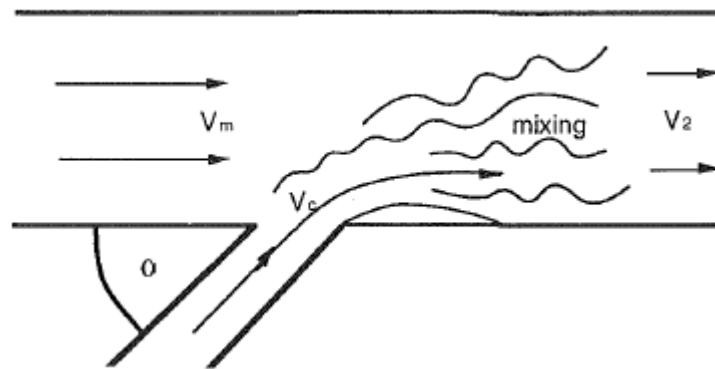
Figure 2- 9: Mixing of injected flow with main stream (Denton, 1993).

Profile Loss

The profile loss is also called two-dimensional loss in turbomachinery, including the quasi-two-dimensional loss near mid-span position and the wake loss arising at the trailing edge. The total entropy generation rate and dissipation coefficient have been given in Eqn 2-9 and Eqn 2-10 for two-dimensional boundary layer, a more useful expression for calculating the total entropy generation in the blade boundary layer was proposed by Denton (1993) as Eqn 2-14, where C_b is the total length of the blade surface, x is the distance along the blade surface, V_0 denotes the blade surface velocity. With the total entropy generation rate, the blade entropy loss

coefficient can be defined as Eqn 2-15, the inlet velocity is selected as the reference velocity.

$$\dot{S} = \sum C_b \int_0^1 \frac{C_d \rho V_0^3}{T} d(x/C_b) \qquad \text{Eqn 2- 14}$$

$$\xi_b = \frac{2\,T\,\dot{S}}{\dot{m} V_{ref}^2} \qquad \text{Eqn 2- 15}$$

Combining Eqn 2-14 and Eqn 2-15, the entropy loss coefficient can be related to the surface velocity distribution and dissipation coefficient as Eqn 2-16, where p denotes the pitch. With the knowledge of surface velocity distribution and dissipation coefficient, it is possible to estimate the blade entropy loss.

$$\xi_s = 2 \sum \frac{C_b}{p \cos \alpha_{ref}} \int_0^1 C_d \left(\frac{V_0}{V_{ref}}\right)^3 d(x/C_b) \qquad \text{Eqn 2- 16}$$

Referring to Eqn 2-16, it is noted that the entropy loss is directly proportional to the surface velocity distribution and the dissipation coefficient, thus more severe entropy loss seems to happen at the blade suction side due to relatively higher surface velocity distribution and much larger extent of turbulent boundary layer.

The effect of Reynolds number and surface roughness on the two-dimensional boundary layer loss is very complicated, in the laminar regime, the loss increases significantly with the decrease in Reynolds number due to the high dissipation coefficient ($Re_\theta < 300$), in the transition regime, the loss is mostly dependent on the surface velocity distribution, even the general trend is difficult to determine. In turbulent regime, the loss decreases with the increase in Reynolds number for very smooth blade, the effect of surface roughness is very significant in terms of increasing the loss. Koch and Smith (1976) conducted a detailed calculation on the loss in an axial compressor, and concluded that the loss increases significantly with the increase in surface roughness under high Reynolds number condition.

Wake loss accounts for a significant part of total profile loss. An expression for wake entropy loss coefficient is derived by Denton as Eqn 2-17, where C_{pd} is the

base pressure coefficient. The first term on the RHS denotes the loss due to base pressure acting on the trailing edge and is greatly affected by the trailing edge thickness, in the case of impeller with blunt trailing edge, it is obvious that the base pressure contributes significantly to the wake loss. The second term represents the mixing loss of the boundary layer before the trailing edge, and the last term represents the loss due to the boundary layer blockage effect at the trailing edge.

$$\xi_w = \frac{C_{pb}t}{w} + \frac{2\theta}{w} + \left(\frac{\delta^* + t}{w}\right)^2 \qquad \text{Eqn 2- 17}$$

Tip Leakage Loss

As described previously, the tip leakage loss is the product of tip leakage flow, which is induced due to the presence of pressure gradient at pressure-side and suction-side. Referring to Figure 2- 6, in the case of thick blade, the tip leakage flow mixes out inside the tip clearance, and consequently, the static pressure is increased as well as the entropy, on the other hand, if the blade is thin, the static pressure recovery is unlikely to happen inside the tip clearance, mixing occurs near the suction side corner. The difference in mixing process may give rise to different entropy generation, Storer (1991) found that most of the entropy generation occurs just near the point of leakage. Denton (1993) derived an expression for calculating tip leakage entropy loss coefficient for unshrouded blades with the assumption of incompressible flow, as given in Eqn 2-18, where C_D is the discharge coefficient, g is the tip clearance height, C is the chord length, h is the blade span, V_s and V_s denotes the suction-side and pressure-side velocity respectively. Referring to Eqn 2-18, the tip leakage entropy loss coefficient is directly proportional to the ratio of tip leakage area to inlet flow area, and greatly affected by the ratio of suction-side velocity to inlet velocity. Both increased tip leakage area and high suction-side velocity would result in higher tip leakage loss.

$$\xi_l = \frac{2C_D gC}{hp \cos \alpha_{ref}} \int_0^1 \left(\frac{V_s}{V_{ref}}\right)^3 \left(1 - \frac{V_p}{V_s}\right) \sqrt{\left(1 - \left(\frac{V_p}{V_s}\right)^2\right)} \frac{dz}{C} \qquad \text{Eqn 2- 18}$$

In fact, the effects of centrifugal force and Coriolis force have not been explicitly considered in Denton's derivation, however, they can be taken into account through correction on discharge coefficient C_D, which can be measured either from experimental or numerical simulation.

Endwall Loss

The endwall loss is the loss arising from the hub and casing boundary layer, and primarily occurs due to the endwall boundary layer separation, as well as very high speed flow. As described previously, secondary flow is common inside the compressor, and it tends to convect the low momentum fluid towards the corner and thus prompt potential separation. High speed flow commonly exists just before the diffuser, thus cause high endwall loss, Denton (1993) discussed that the endwall loss is high at the radial part of the casing near the impeller outlet and inside the diffuser for a centrifugal compressor with unshrouded impeller, while for the shrouded impeller centrifugal compressor, the endwall loss is relatively high at the axial part of the casing. In a small size centrifugal compressor, strong interaction exists between the aforementioned tip leakage flow and the endwall boundary layer flow, in general, high loss is generated from the interaction, however, as stated by Storer (1991), tip leakage flow can be beneficial, he showed that tip leakage flow could help re-energizing the near separation boundary layer at the suction-side casing corner, and thus prevent the corner separation and reduce the potential loss. The endwall loss is strongly affected by the incoming boundary layer and the geometry, as a result, it is very difficult to predict the endwall loss reliably with any theoretical model.

2.3. Existing Works on Centrifugal Compressor

Generally, there are three different approaches for investigating the centrifugal compressor, theoretical approach, experimental approach and numerical approach respectively. Theoretical approach is the most fundamental method, starting with the basic thermodynamic and fluid dynamic principles to construct a model, which could represent the real physics as much as possible, general assumptions are usually made according to the specific problem. Once the model has been

constructed, the prediction can be made in very short time, however, for most of the time, it is heuristic and empirical, rather than mathematical, the models are mostly based on 1D and 2D assumptions, it is too ideal to take into account the flow features such as vortex interaction, unsteadiness and etc, the whole picture of physical mechanism inside a centrifugal compressor is still far from complete. Experimental approach, as one of the basic tools, is essential to the development of centrifugal compressor, it has been applied historically and widely to investigating the performance, flow behaviour and understanding the physics involved, however, it has been used as a evaluation tool rather than a design tool for most of the time. Theoretical and experimental approaches for compressor performance evaluation are acceptable and essential, however, computational modelling is becoming more critical in the turbomachinery design phase, in certain cases, theoretical approach cannot provide accurate enough prediction, experiments are expensive and time-consuming, conversely, computational modelling could be done in relatively short time and provides more details about the flow field, thus reduces the design cycle, cost and helps improving the design. It is well known that the computational modelling is not valid without the support from related experiments, so it is always applied to complement experimental and theoretical approaches.

Early experiment on centrifugal compressor flow field was very difficult due to the unavailability of proper instruments, it was not until the end of 1950s that a representative experiment was conducted by Acosta and Bowerman (1957) thanks to the development of instruments, rotating pressure probe was employed to measure the flow field inside four low backsweep(β_2=23.5^o) 2D impeller and one low backsweep(β_2=17°) 3D impeller. Static pressure distribution, relative velocity and relative total pressure loss have been obtained, a high loss region was observed to exist at the suction side shroud corner. The 3D impeller was noted to have better inflow condition, this may due to design of inducer section on 3D impeller, the flow can match the blade smoothly.

Experimental investigations led Dean and Senoo (1960) to the well known "jet-wake structure" model, the flow discharge from the impeller outlet was observed to be unsteady and axially asymmetric. A theory was proposed based on the simplified model, the theoretical result was shown to be consistent with the

measurements. They believed that the "jet-wake structure" generally mixed out rather quickly and restore the uniform flow condition. Further investigation has been conducted by Eckardt (1975), who employed the Laser Anemometer (LA) to take measurements of flow field inside the Eckardt impeller, it was found that separation occurred at the suction-side shroud corner 50% chord position, and the separated region grew towards the impeller outlet, occupied about 20% of the passage cross-section at 70% chord position, and continued growing to 35% of the passage cross-section at 90% chord position, however, the separated flow only account for 15% of the total mass flow rate. Highly non-uniform flow with regions of low momentum and high momentum fluids were observed at the impeller outlet, thus confirmed the existence of "jet-wake structure". Later, Johnson and Moore (1980) investigated the effect of secondary flow on the convection of low rotary stagnation pressure ($p^* = p + 1/2\,\rho W^2 - 1/2\,\omega^2 r^2$) fluid and the formation of wake at the suction-side shroud corner, measurements on relative velocities and rotary stagnation pressures were taken on five cross-sectional planes between the inlet and outlet of the impeller, it was concluded that the convection of low rotary stagnation pressure fluid is critical to the formation of "jet-wake structure" at the impeller outlet.

Krain (1988) studied the flow field inside a newly design backswept impeller using Laser-2-Focus (L2F) technique, the distortion of through-flow pattern and the formation of secondary flow were attributed to the presence swirling flow inside the impeller. Separation was observed at the pressure-side near 50% chord position, and grew towards downstream, then the separated fluid moved to the middle of the passage at 70% chord position and occupied half of the passage cross section, and then the flow smoothed near the impeller outlet, "jet-wake structure" was clearly identified, however, it was different from the widely accepted classical "jet-wake structure" observed by Dean and Senoo (1960). A Low Speed Centrifugal Compressor (LSCC) was designed at NASA to duplicate the important features of high speed subsonic centrifugal compressor in a large low speed substitute, thus enables the flow field measurements with LA. Hathaway et al. (1993) conducted detailed experiments and numerical simulation on LSCC, it was found that the low momentum fluid near the blade surface migrated towards to blade tip, and

entrained in the tip clearance flow, and then this fluid is transported towards the pressure-side/shroud corner, finally, contributed to the formation of through-flow wake, which mixed out slowly, as a result, two different wakes were observed in the vaneless space, through-flow wake and viscous blade wake respectively.

Tip leakage flow plays an important role in the performance and stability of the centrifugal compressor, Pampreen (1973) discussed the design consideration for small centrifugal compressors, performance data were collected for 6 different centrifugal compressors to investigate the effect of tip clearance and Reynolds number, it was found that the correlation between the compressor performance and the tip clearance was rather irregular, however, on average, the compressor performance deteriorated by 3% with the increase in tip clearance by 10%, and tip clearance effect is more prominent for small centrifugal compressor compared to Reynolds number effect. Later, Klassen, Wood and Schumann (1977a; 1977b) confirmed the detrimental effect of tip clearance on the centrifugal compressor performance through experiments on two different high pressure ratio centrifugal compressor, it was concluded that the efficiency drops as the increase in tip clearance for all tested rotational speed and mass flow rate. Syed, Ma and Yang (2006) conducted numerical simulation on a unshrouded impeller centrifugal compressor to investigate the effect of tip clearance, which was varied from 0mm to 1mm. The efficiency was found to be the highest if there was not tip clearance, and worst with the largest tip clearance, and it was also found that the impeller and diffuser were affected differently by the tip clearance, the impeller efficiency peaked at smaller tip clearance, while diffuser efficiency peaked at larger tip clearance.

Mashimo, Watanabe and Ariga (1979) conducted detailed experiments on the tip leakage flow induced loss in a centrifugal compressor. Tip clearance, Reynolds number and operation conditions were varied independently, it was found that centrifugal compressor operating at large mass flow rate tends to have more efficiency drop due to the increase in tip clearance, and tip leakage loss is higher if the Reynolds number is increased, however, the effect was found to be minor. The underlying reason may be that the impeller operating at higher mass flow rate will experience higher blade loading, thus cause higher pressure gradient between the

blade pressure-side and suction-side. Similar conclusion has also been made by Senoo and Ishida (1987), who modified their original theory on the tip clearance loss of centrifugal impellers to include the variation of slip angle due to tip leakage flow, and validated with the experimental results in literature, good agreement was achieved. The efficiency was found to be less sensitive to the tip leakage flow for small flow rate centrifugal impeller, so was the high pressure ratio compressor at reduced shaft speed. Plamer and Waterman (1995) designed a two-stage high pressure ratio centrifugal compressor. Two different impellers were tested, one with 16 main and 16 splitter blades, and the other with 19 main and 19 splitter blade. The former tends to have relatively uniform meridional blade loading, while the latter has reduced loading near the blade trailing edge. It was found that the efficiency was relatively less sensitive to the tip clearance for the reduced loading impeller.

Ishida and Senoo (1981) measured the pressure distribution along the shroud for three types of centrifugal impeller at seven different tip clearances each, tip clearance ratio and static pressure rise due to the reduction in relative velocity are directly related to the tip clearance loss, it was inferred that the compressor performance could be improved by reducing the tip clearance at the leading edge, where the reduction in relative velocity is significant. To investigate the effect of tip clearance ratio on the input power, velocity distribution, relative flow angle, further experiments have been conducted by Ishida, Senoo and Ueki (1990) on two types of unshrouded centrifugal impellers at four different tip clearance each, one is radial impeller and the other is backward-leaning impeller, it was found that, for radial impeller, the input work, velocity distribution and relative flow angle were hardly changed at different tip clearances, while for the backward-leaning impeller, the input power and relative flow angle were reduced if the tip clearance was increased, the velocity distribution was not affected noticeably.

Farge, Johnson and Maksound (1989) studied the tip leakage flow inside an shrouded impeller with an internal tip clearance between the shroud and the blade tips. They found that the static pressure distribution is almost unaltered with the presence of tip clearance. The low momentum fluid from the suction side surface and tip leakage flow accumulated at the suction-side/shroud corner and

contributed to the formation of wake, which mitigated to the middle of the shroud at the impeller outlet due to the effect of tip leakage flow. While Liu, Ping and Zangeneh (2013) conducted numerical simulation on the Eckardt impeller to investigate the effect of tip leakage flow, three different tip clearance size configurations were examined, 0%, 2.9% and 4.96% of exit width respectively. It was found that there is clear correlation between the blade loading and tip leakage flow distribution, the magnitude of the blade loading was reduced with the increase of tip clearance size, while the shape of the blade loading curve did not change greatly. A small amount of loss occurred inside the tip clearance, instead, much of the loss happened due to the formation of tip leakage vortex.

Schleer, Song and Abhari (2008) investigated the effect of large tip clearance on the onset of instability inside a highly-loaded centrifugal compressor, time-resolved static pressure measurements were taken along the shroud surface for two different tip clearance configurations, tip leakage vortex was identified as a region of high pressure deviation originating from the leading edge, they found that the trajectory of this vortex was strongly affected by the mass flow rate and the tip clearance size. The tip leakage vortex tended to move upstream when the mass flow rate was reduced, and touched the blade pressure-side at sufficiently low mass flow rate, further reducing the mass flow rate caused the tip leakage vortex trajectory to be perpendicular to the rotation axis, and initialized the inlet tip recirculation, and ultimately led to the disappearance of tip leakage vortex and rotating stall inside the diffuser. It seems that there is a relation between the tip leakage flow and the rotating stall inception, Tomita et al. (2013) studied two centrifugal compressor with different operation range widths using both experimental and computational methods. It was found that, in the case of narrow operation range compressor, the amplitude of blade passing pressure fluctuation decreased rapidly as the inlet mass flow rate was reduced, while for the counterpart, the amplitude of blade passing pressure fluctuation decreased gradually. Blockage due to tip leakage vortex breakdown was observed for the latter only, it was concluded that the blockage was actually beneficial, it worked to stabilize the flow field, and delayed the occurrence of rotating stall.

Another very important phenomenon inside a centrifugal compressor with vaned diffuser is the impeller-diffuser interaction. The unsteadiness induced due to the diffuser vanes would distort the certain potion of the impeller flow field, and cause fluctuating forces on the impeller blade; at the same time, the wake shedding from the impeller blade would affect the diffuser flow field. Early work on the potential effect of diffuser vane on the impeller flow field was conducted by lino and Kasai (1985). The most critical parameter determining the impeller-diffuser interaction is the radial spacing, as pointed out by Rodgers (1982), Clements and Artt (1989), Gottfreid and Fleeter (2002), the existence of an optimum radial spacing for peak performance is also identified.

More detailed flow measurements and numerical simulation would help to reveal the flow features of the impeller-diffuser interaction. Arndt et al. (1990) investigated the impeller-diffuser interaction by conducting experiment on a centrifugal compressor, with two-dimensional impeller and vaned diffuser. The flow coefficient and number of diffuser blade were varied, as well as the gap between the impeller blade trailing edge and the diffuser blade leading edge. It was observed that large pressure fluctuations occurred in both diffuser and impeller and were the same order of magnitude as the total pressure across the compressor. For diffuser, the largest pressure fluctuation occurred on the suction-side near the blade leading edge, while the largest pressure fluctuation occurred at the blade trailing edge for impeller. The flow coefficient was found to have opposite effects for impeller and diffuser, the increase in flow coefficient tends to cause increase in impeller pressure fluctuation and reduction in diffuser pressure fluctuation. It was also found that the increase in diffuser blade would reduce the impeller pressure fluctuation significantly.

Ubaldi et al. (1996) made detailed flow measurements in the so called ERCOFTAC centrifugal compressor to investigate the influence of diffuser vanes induced unsteadiness on the impeller flow. Local defects of radial velocity and pressure fluctuations were observed due to the presence of diffuser vanes. The periodic interaction between the diffuser vane induced unsteadiness and the nonuniformities of impeller relative flow gives rise to the unsteady work transfer (implied from Euler work equation) and local reverse flow. The diffuser vane

induced pressure fluctuations actually affect the pressure level in the whole impeller. Recently, numerical simulation was conducted on the ERCOFTAC centrifugal compressor by Petit and Nilsson (2013), comparison was made between the computed results and experimental data, good agreement was achieved.

Shum, Tan and Cumpsty (2000) found that larger viscous loss is associated with tip leakage flow with the presence of impeller-diffuser interaction using numerical simulation, the effects of impeller-diffuser interaction on the flow field at impeller outlet can be summarized as reduced blockage, reduced slip and increased loss. The reduction in radial spacing could help to reduce the blockage and slip, however, too small the radial spacing would bring large viscous loss and overweigh the benefits. It is thus proved the existence of an optimum radial spacing for peak performance. They also found that the effect of impeller-diffuser interaction on impeller is much more significant than that on diffuser. They concluded that the beneficial effects of impeller-diffuser interaction are mainly attributed to the reduced blockage and reduced slip associated with tip leakage flow.

Ziegler, Gallus and Niehuis (2003) investigated the effect of impeller-diffuser interaction on the diffuser performance, the radial spacing was varied between 4 and 18%. They found that the reduction in radial spacing results in slightly increase in the impeller work input, while the diffuser performance is improved in terms of pressure recovery coefficient and total pressure loss coefficient. They attributed the improved diffuser performance to the unloading of the highly loaded vane pressure-side, which tends to bring more homogeneous flow field. Further study has been conducted by Boncinelli et al. (2007) numerically, two centrifugal compressors with different radial spacing was simulated with both steady and unsteady simulation. The computed results were validated against the experimental data from Ziegler, Gallus and Niehuis. They found that the unsteadiness from the impeller-diffuser interaction could actually bring the high energy fluid at the vane suction-side to the pressure-side, thus unloads the highly loaded pressure-side and suppresses the pressure-side separation, as a result, the total pressure loss is reduced.

2.4. Existing Works on Riblets

Riblets surface is a surface with a collection of microgrooves or longitudinal ribs along the same direction, either streamwise or cross-stream. The height and spacing are the most critical design parameters determining its performance, denoted by h and s respectively. Height is the distance between the peak and base, and spacing is the distance between two adjacent peaks. Different riblets configurations are designed by employing different cross-section shapes, such as sawtooth, scalloped, blade and trapezoidal base riblets. An illustration is given in Figure 2- 10. Riblets work by manipulating the near wall flow structure inside the boundary layer, therefore, the geometry of riblets is often non-dimensionalised using the near-wall flow parameters characterizing a turbulent boundary layer, i.e.

$$s^+ = \frac{su_\tau}{\nu} \qquad\qquad \text{Eqn 2- 19}$$

$$h^+ = \frac{hu_\tau}{\nu} \qquad\qquad \text{Eqn 2- 20}$$

Where $u_\tau = (\tau_0/\rho)^{0.5}$ is the friction velocity and ν is the kinematic viscosity, ρ is the fluid density and τ_0 is the local wall shear stress. Most of the works on riblets are conducted through experiments, only a few related numerical simulation are available due to the extremely high computational cost of DNS and the inability of LES & RANS in predicting the flow field accurately. The existing numerical simulations with DNS are primarily on the investigation into the physical mechanisms.

2.4.1. Turbulent Skin Friction Drag Reduction

The concept of riblets for turbulent skin friction drag reduction has been studied extensively at NASA Langley starting from 1970s, e.g. Walsh and Weinstein (1978); Walsh (1980). Due to the great benefits implied from these results, turbulent skin friction drag reduction using riblets has been a very active research field for two decades.
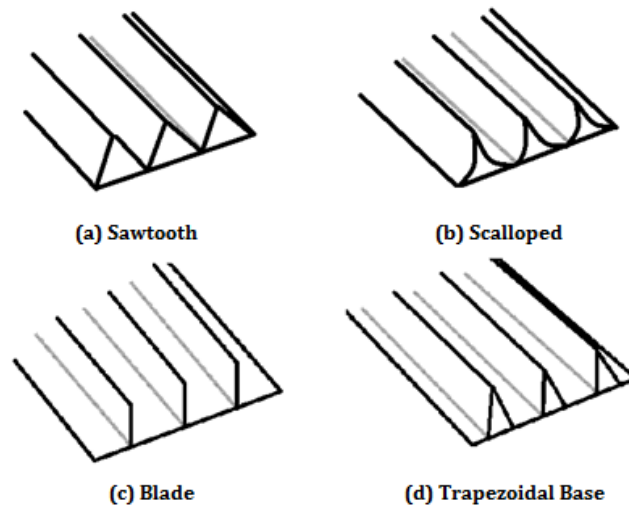
Figure 2- 10: Different types of riblets.

Most of the tests have been conducted with riblets on flat plate, due to the relatively simple set-up and ease of taking measurements. Early works conducted by Walsh (1983) and Walsh & Lindemann (1984) reveal that drag reduction can be achieved with riblets as long as s^+ is below 30, and maximum drag reduction occurred around $s^+ \approx 15$. The maximum skin friction drag reduction of each type of riblets (sawtooth, scalloped and blade) was compared by Dean (2011) with the data obtained from Bechert et al. (1997a). A summary is given in Table 2- 1. The blade type riblets perform the best among the three with a maximum skin friction drag reduction of 9.9%, however, the structure is not that durable due to the requirement of very small blade thickness. Large blade thickness will harm the skin friction drag reduction performance. Sawtooth type riblets rank the last with a maximum skin friction drag reduction of 5%, and this structure is very durable. The scalloped type riblets performance lies between that of sawtooth and blade. Nevertheless, for three different types of riblets tested the maximum drag reduction all occurs around $s^+ \approx 16$. According to the studies by Bechert et al. (1997a), if the spacing between the sawtooth is kept the same, as the sharpness of the sawtooth is increased (trapezoidal base riblets), the performance of the riblets increases and approaches towards that of the blade riblets (see Figure 2- 11).

Riblet shape	Relative rank*	Maximum drag reduction**	Optimum geometry**	Comments
Sawtooth	3	5%	h/s ~ 1, α ~ 60°	Most durable
Scalloped	2	6.5%	h/s ~ 0.7	
Blade	1	9.9%	h/s ~ 0.5	Drag reduction increases as riblet thickness decreases. Durability is an issue.

*   1 corresponds to greatest drag reduction
** based on published data in Bechert et al., 1997

Table 2- 1: Comparison of optimum geometry of different riblets (Dean, 2011).

Wang et al. (2008) also studied the performance of sawtooth riblets and trapezoidal tip riblets with slight variations in their geometry (see Table 2- 2) in a water flow at a speed of 1.54 m/s. Particle Image Velocimetry (PIV) was used to take measurements of the near wall velocity distribution of both grooved surface and smooth surface. The loss of momentum method and Ludwieg & Tillman empirical formula were used to calculate the local skin friction coefficient. The results are shown in Table 2- 3. It is observed that the first three configurations could achieve total drag reduction, it is also noted that with a smaller spacing s, the drag reduction performance is improved. They concluded that the peak geometry has a great effect on the drag reduction performance. In the case of trapezoidal tip riblets, the total drag increased due to a larger wetted area. It is obvious that the non-dimensional spacing s^+ and the effectiveness of riblets are closely correlated.
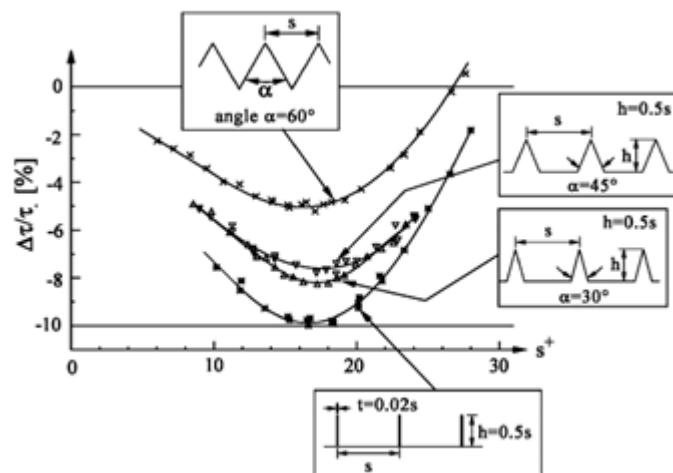
Figure 2- 11: Drag reduction performance of various rib geometries (Bechert et al., 1997a).
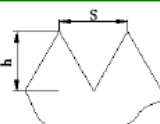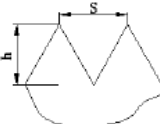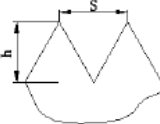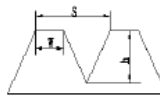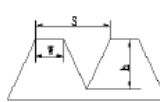
number	dimension	Section shape
1#	s=1.2mm h=0.8mm	
2#	s=1.0mm h=0.8mm	
3#	s=1.8mm h=0.8mm	
4#	s=1.8mm w=0.8mm h=0.8mm	
5#	s=1.2mm w=0.8mm h=0.8mm	

Table 2- 2: Different riblets surface configurations (Wang et al., 2008).

number	C_f by loss of momentum thickness	Drag reduction efficiency η	C_f by Ludwieg & Tillman	η
1#	3.070×10^{-3}	5.21%	3.544×10^{-3}	4.93%
2#	3.048×10^{-3}	5.89%	3.478×10^{-3}	5.67%
3#	3.099×10^{-3}	4.31%	3.575×10^{-3}	4.11%
4#	3.380×10^{-3}	-4.45%	3.919×10^{-3}	-5.11%
5#	3.343×10^{-3}	-3.20%	3.873×10^{-3}	-3.90%
Smooth plate	3.239×10^{-3}	——	3.728×10^{-3}	——

Table 2- 3: Drag reduction efficiency of different riblets configurations (Wang et al., 2008).

El-Samni, Chun and Yoon (2007) examined the low Reynolds number flow over thin rectangular riblets distributed uniformly at only one of the channel wall using DNS. The riblets drag reduction ratio was predicted with five different s^+ values. The results were compared with the experimental data from Bechert et al. (1997a), as shown in Figure 2- 12. Good agreement has been achieved. The maximum drag

reduction was obtained at $s^+ \sim 18$, which is very similar to that from Bechert et al. And the drag reduction can be achieved when s^+ is below about 30.
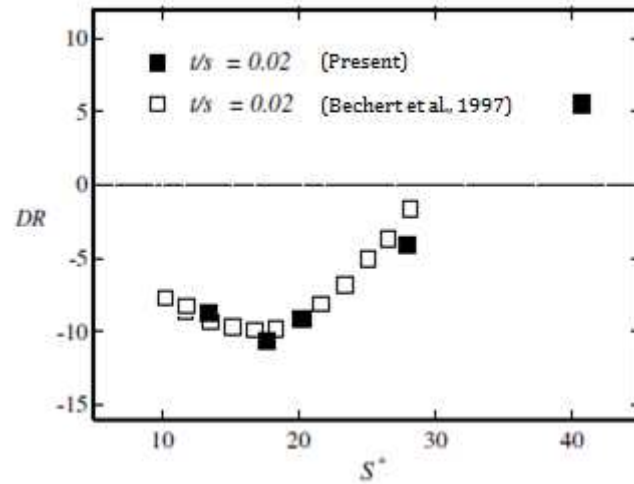
Figure 2- 12: Comparison of drag reduction ratio reproduced from El-Samni, Chun and Yoon (2007).

Other alternative riblets, such as asymmetrical riblets and rounded peak riblets (Walsh, 1982), brother-sister type riblets (Bechert et al., 1997b), have also been tested. But they do not show a significant improvement in drag reduction. Hence the results will not be discussed here.

The potential benefit of riblets has attracted a tremendous attention from the oil industries, because about 90% of the total drag in pipelines originates from the skin friction drag and even a minor reduction in the skin friction drag could result in a huge saving in the pumping power. Nitschke (1983) studied the airflow in a pipe fitted with riblets with rounded peaks and flat valleys. The drag reduction was evaluated from the pressure drop measurements over a length of 120 pipe diameters. A drag reduction was observed when the riblets spacing is between 8 and 23 wall units, with the maximum drag reduction of about 3% occurring at $s^+ \sim 11 - 15$. Liu et al. (1990) observed a maximum drag reduction of 5-7% at $s^+ \sim 11 - 16$ during their experiment in a fully developed turbulent flow in a water pipe with sawtooth riblets. Similar results were also obtained by Enyutin et al. (1995), a maximum drag reduction of about 6-7% was achieved at $s^+ \sim 14 - 18$. In a summary, the maximum drag reduction in a grooved pipe occurs when $s^+ \sim 11 - 18$

and the variation in the optimal s^+ may be attributed to the measurement uncertainties.

The effects of riblets on the performance of compressor have also been investigated by only a few researchers. Boese and Fottner (2002) conducted an experimental investigation of the loss behaviour of a highly loaded compressor cascade under the effects of riblets. Three riblets configurations with different sizes were first tested, a optimum size for riblets was obtained with the pressure measurements. Then a detailed flow visualization was conducted on the optimized riblets ($s^+ = 2h^+$), which are actually trapezoidal base riblets. The results show that the riblets mainly affect the suction-side boundary layer behaviour, a reduction in loss coefficient of 6-8% was achieved when $h^+ \approx 9$, and loss increases when h^+ is above 20. Later, Oehlert and Seume (2006) tested the machined trapezoidal base riblets fabricated by grinding and laser machining on NACA compressor blades, they found it was difficult to achieve the required accuracy by machining. A loss reduction about 3% was achieved by riblets on flat plate, while for compressor blade, only 1.5% reduction in loss was obtained. Lietmeyer, Oehlert and Seume (2013) conducted further tests on a NACA 6510 compressor blade with trapezoidal base riblets on pressure-side or suction-side or both sides. A profile loss reduction of 4% was obtained with the riblets on the suction-side, while a reduction of 1.01% was achieved with the riblets on the pressure-side, if riblets are applied on both sides, a loss reduction of 4.9% was obtained. Investigation of compressor blade under high pressure-side incidence showed that a loss reduction up to 7.2% was achieved with riblets on suction-side, this higher reduction was attributed to the elimination of suction-side separation bubble with riblets. It is noted that the application of riblets is the most effective when applied to suction-side. However, it should also be noted that all the riblets applications in compressor as given above are all applied to cascade only, for which the blades are completely stationary.

The effects of pressure gradient and yaw angle are very important in practical application, they have been investigated by many researchers. Sundaram et al. (1996; 1999) tested the effectiveness of riblets in drag reduction on two different airfoils up to moderate incidence angles in wind tunnels. The Clauser pressure gradient parameter, $\beta = \frac{\delta^*}{\tau_w} \frac{dp}{dx}$, was used to characterize the level of adverse

pressure gradient at various incidence angles. It was concluded that the effectiveness of riblets increases with the adverse pressure gradient up a certain value of β, beyond which the effectiveness is reduced, presumably due to the flow separation on the airfoil upper surface. The yaw angle has a significant effect on the magnitude of drag reduction. Walsh and Lindemann (1984) showed that at a yaw angle of 15 deg the maximum drag reduction is only reduced slightly, however, when the yaw angle increases to 30 deg, no drag reduction was observed. Coustols (1989) studied the yaw-angle effects with 3M riblets, he observed that the drag reduction was significantly reduced from 10 to 3% at a yaw angle of 20 deg. He also found that the drag reduction dropped from 7 to 3% for an axisymmetric body when the yaw angle increased from 0 deg to 20 deg. Similar conclusions on the effect of yaw angle have also been drawn by Sundaram et al. (1999).

A lot of work has been undertaken to understand the physical mechanism of riblets in turbulent skin friction drag reduction. Some hypotheses have been proposed. However, the physical mechanism is still an open question under extensive research. It is also possible that different physical mechanisms work together to make the riblets effective in reducing the turbulent skin friction drag.

Bacher and Smith (1985) pointed out that the flow field above the riblets surface will look like what is illustrated in Figure 2- 13. Due to the presence of riblets, a pair of counter rotating secondary vortex was generated between the peaks of riblets, just above the riblets. This pair of secondary vortices increased the skin friction drag at the peak of the riblets, but within a limited region. They weaken the primary streamwise vortex formed during the bursting process, as a result the fluid flow at the bottom of the riblets is at lower speed, and the skin friction drag reduction outweighs the increased drag due to the increased wetted area. Choi, Moin and Kim (1993) studied the turbulent flow over riblets (v-groove) with DNS to investigate the physical mechanism. They announced that their results are in good agreement with experimental results. The mean velocity profile shows upward and downward shifts in the log-law for drag decreasing and drag increasing cases respectively. They found that the differences in mean velocity and turbulence quantities are limited to the inner region of the turbulent boundary layer. In the case of drag reduction configuration, the velocity, vorticity fluctuations

and the Reynolds shear stresses above the riblets were reduced. They concluded that the viscous drag reduction happened to the riblets with small spacing is caused by the restricted streamwise vortices above the riblets such that only a limited wetted area is exposed to the high speed fluid. On the contrary, the streamwise vortices will be located in the riblets valleys for riblets with larger spacing. Similar physical mechanism has also been proposed by El-Samni, Chun and Yoon (2007).

With reference to Walsh (1982), Walsh (1983) postulated that the riblets act to reduce the intensity of the near-wall turbulence eruptions rather than reduce the frequency of eruptions. Choi (1989), on the other hand, proposed that the presence of riblets will impede the spanwise motion of streamwise vortices, hence disrupt and weaken the bursting process and result in a skin friction drag reduction. In contrary, in the case of laminar flow, the skin friction drag will increase due to the presence of riblets, which increases the wetted area considerably.
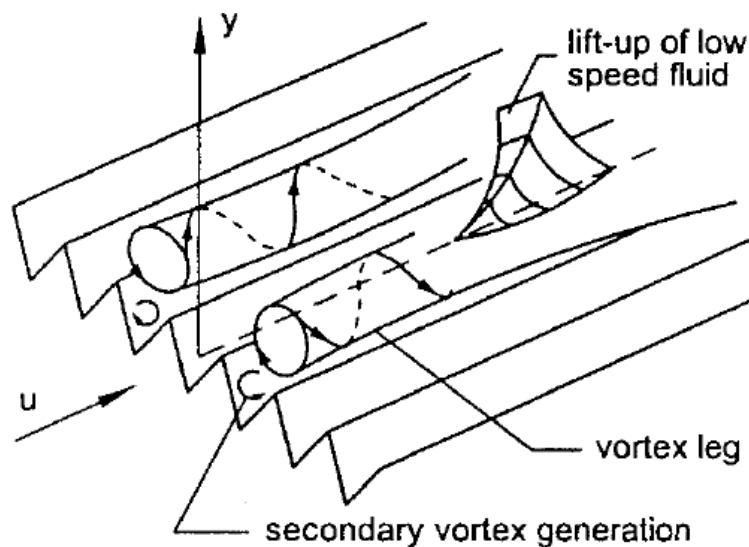
Figure 2- 13: Schematic of streamwise vortex interaction with riblets surface via viscous effects (Bacher and Smith, 1985).

2.4.2. Delay of Laminar-Turbulent Transition

As mentioned previously laminar-turbulent transition is a very important and extensively studied topic, nonetheless, the physical mechanism involved is still not fully understood. If the laminar-turbulent transition can be delayed, the direct benefit is the reduction in skin friction drag. The research into the effect of riblets

on laminar-turbulent transition is only conducted by a few researchers. Early works were done by Kozlov et al. (1990), Neumann & Dinkelacker (1991), the beneficial effects of riblets on delaying transition were found. A representative work was conducted by Grek, Kozlov and Titarenko (1996), the effect of riblets on the three-dimensional nonlinear structure occurring during laminar-turbulent transition was studied. This nonlinear structure is also called the Λ-structure. They found that the application of riblets would delay the transformation of Λ-structure into turbulent spot, thus shifts the transition point downstream. This finding is quite opposite to the effect of riblets on two-dimensional Tollmien-Schlichting (TS) waves, for which the disturbance is excited, thus induce early transition. In total, the riblets would help to stabilize the Λ-structure (nonlinear stage of transition) and destabilize the TS waves (linear stage of transition). Therefore, special attention has to be paid to the location of riblets. Further development can be found in Litvinenko et al. (2006) on the physical mechanism of delaying the transformation of Λ-structure.

2.5. Discussion

In this chapter, the general performance parameters and different flow phenomena of centrifugal compressor were introduced, the flow involved is complicated, distinct features like viscous, highly unsteady, swirling and transitional make it very difficult to obtain a reliable prediction. The effect of strong curvature, centrifugal force, Coriolis force and strong interaction further complicate the situation. The loss mechanisms in compressors were discussed with the help of theoretical models, it was shown that tip leakage loss is mainly related to the ratio of tip leakage area to inlet area and the ratio of suction-side velocity to inlet velocity, in other words, if the inlet condition is fixed, the tip leakage loss will be higher with larger tip clearance size and higher suction-side velocity. Two-dimensional profile loss and endwall loss are very similar, they are dependent on the state of the boundary layer and surface velocity. Wake loss is another kind of profile loss, it is closely related to the shape of the trailing edge and the state of the boundary layer. In the case of centrifugal compressor, two-dimensional profile loss seldom occurs, the blade surface loss is very similar to the endwall loss. In

literature, large amount of works have been done on centrifugal compressor, the flow behaviour varies for different geometries, therefore, it is essential to analyse the flow field for a different centrifugal compressor. Riblets surface is effective in reducing the turbulent skin friction drag and delaying laminar-turbulent transition. The concept of applying riblets to turbulent skin friction drag reduction has been pursued extensively, trapezoidal base riblets have been found to be the best considering the drag reduction performance and ease-of-manufacture. The discussion on riblets will be elaborated in chapter 8, where riblets have been proposed to reduce the hub endwall loss in Dyson V2 centrifugal compressor.

Chapter 3

Turbulence Modelling

3.1. Introduction

In most cases, it is not generally possible to depict the complete picture of natural and engineering flow without referring to turbulence theory. A turbulent flow is characterized by its chaos in both space and time. Osborne Reynolds is probably most famous for his findings on the difference of laminar and turbulent flows. In 1883, a series of experiments were conducted at the University of Manchester, coloured dye was steadily injected on the centreline of a pipe in which water was flowing (the interested reader is referred to the MACE website for a picture of the experimental apparatus). Reynolds found that the flow pattern was quite stable and the dye can be clearly identified even far downstream when the flow is at low speed, as the flow speed was increased, at certain point, the flow pattern underwent significant changes, the injected dye began to oscillate and mixed out. Figure 3- 1 presents a sketch of the distinct flow patterns, with which Reynolds classified the flow into two categories, laminar and turbulent flow respectively. The onset of the oscillating flow pattern was found to be related to the inertial and viscous forces, a non-dimensional number called Reynolds number was proposed to include the inertial and viscous forces, as defined in Eqn 3-1, where ρ denotes the fluid density, U denotes the fluid velocity, L denotes a length scale (denotes the pipe diameter here) and μ is the dynamic viscosity.

$$Re = \frac{\rho UL}{\mu} \qquad\qquad \text{Eqn 3- 1}$$

For pipe flow, the transition from laminar to turbulent flow could occur in a range of Reynolds numbers from approximately 2300 to 4000. For the flow to keep the state of laminar, the Reynolds number should be less than 2300, on the other hand, if the Reynolds number exceeds 4000, then the flow is turbulent.

Laminar flow
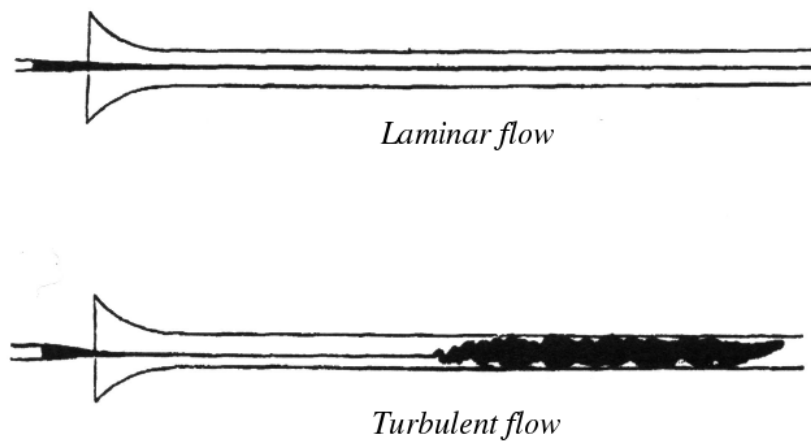
Turbulent flow

Figure 3- 1: Laminar and turbulent flow patterns (Reynolds, 1901).

The nature of turbulence is generally described through the energy cascade proposed by Richardson (1922), who hypothesized that turbulent flow contains lots of eddies with different sizes, eddies receive energy from the mean flow through the vortex stretch and other nonlinear processes and grow up to reach the integral length scale, which is of the same order of magnitude as the flow geometry. Then the large eddies break up into small eddies with the energy transfer taking place from large eddies to small eddies, this process continues until the smallest eddies reach the dissipative length scale, the energy is dissipated as heat, marking the completion of the turbulent energy transfer process. For a statistically steady flow, the energy dissipated at the smallest eddies has to be equal to the kinetic energy supplied by large eddies, and thus the dissipation rate should be independent of the viscosity. Kolmogorov (1942) proposed a length and time scale based only on the dissipation rate and viscosity, as given in Eqn 3-2 and Eqn 3-3 respectively, they are usually termed Kolmogorov scales.

$$\eta = \left(\frac{\nu^3}{\epsilon}\right)^{1/4} \qquad \text{Eqn 3- 2}$$

$$\tau_\eta = \left(\frac{\nu}{\epsilon}\right)^{1/2} \qquad \text{Eqn 3- 3}$$

Where ν denotes the kinematic viscosity, and ϵ denotes the dissipation rate of the smallest eddies.

With the drastically increased computational power nowadays, Computational Fluid Dynamics (CFD) is becoming an increasingly important technique for either fundamental research or engineering design. Compared to experimental method, the time cycle is much shorter and the cost is much lower for applying CFD method, not to mention the ability to simulate extreme condition which would not otherwise be able to deal with. Three different approaches exist, Direct Numerical Simulation (DNS), Large Eddy Simulation (LES) and Reynolds Averaged Navier Stokes (RANS) respectively. The selection of the appropriate approach would largely depend on the problem to be investigated and the availability of computational resources. DNS resolves all the scales, thus it is extremely computational expensive and time-consuming, but could accurately predict the motion of the smallest eddies, it is generally employed to investigate the underlying physical mechanism of the flow, but the application is limited to simple geometry and low Reynolds number flow, mostly in academic research, while RANS is the most popular approach for engineering application at this moment due to its low computational cost, it embodies Reynolds averaging and turbulence modelling techniques to simplify the original Navier-Stokes equations and solves for the mean flow parameters, thus all information about the eddies are lost, nonetheless, it is mean parameter that is important for most engineering designs. A compromise between DNS and RANS was made and bring about the LES, which simply filters out small eddies with certain filter size, only large eddies are directly computed, Sub-Grid Scale (SGS) model is used to compute the effects of small eddies. Compared to DNS, the computational cost of LES is significantly lower, however, it is still computational expensive and not generally affordable in engineering applications. In the current work, only RANS would be applied, so only the related topics would be introduced and discussed. The RANS equation will be first introduced, followed

by the formulation of a few eddy viscosity turbulence models and the Reynolds Stress Model (RSM).

3.2. Reynolds Averaged Navier-Stokes Equations

The fluid flow can be characterized by a set of partial differential equations, called Navier-Stokes equations, which are derived from the conservation of mass, momentum and energy equations. In Cartesian coordinate, the Navier-Stokes equations for incompressible, Newtonian fluid is given as:

$$\text{div}(\mathbf{u}) = 0$$

$$\frac{\partial(u)}{\partial t} + \text{div}(u\mathbf{u}) = -\frac{1}{\rho}\frac{\partial p}{\partial x} + \text{div}\left(\frac{\mu}{\rho}\text{ grad }u\right)$$

$$\frac{\partial(v)}{\partial t} + \text{div}(v\mathbf{u}) = -\frac{1}{\rho}\frac{\partial p}{\partial y} + \text{div}\left(\frac{\mu}{\rho}\text{ grad }v\right)$$

$$\frac{\partial(w)}{\partial t} + \text{div}(w\mathbf{u}) = -\frac{1}{\rho}\frac{\partial p}{\partial z} + \text{div}\left(\frac{\mu}{\rho}\text{ grad }w\right)$$

$$\frac{\partial(i)}{\partial t} + \text{div}(i\mathbf{u}) = -\frac{p}{\rho}\text{ div }\mathbf{u} + \text{div}\left(\frac{k}{\rho}\text{ grad }T\right) + \Phi$$

Eqn 3- 4

Where $S_{\blacksquare}$ is the source term, and Φ is given as:

$$\Phi = \frac{\mu}{\rho}\left\{ \begin{array}{c} 2\left[\left(\frac{\partial u}{\partial x}\right)^2 + \left(\frac{\partial v}{\partial y}\right)^2 + \left(\frac{\partial w}{\partial z}\right)^2\right] + \\ \left(\frac{\partial u}{\partial y} + \frac{\partial v}{\partial x}\right)^2 + \left(\frac{\partial u}{\partial z} + \frac{\partial w}{\partial x}\right)^2 + \left(\frac{\partial v}{\partial z} + \frac{\partial w}{\partial y}\right)^2 \end{array}\right\} + \frac{\lambda}{\rho}(\text{div }\mathbf{u})^2 \quad \text{Eqn 3- 5}$$

Where $\lambda = -\frac{2}{3}\mu$.

The aforementioned RANS equations can be derived from the Navier-Stokes equation with the Reynolds averaging technique, the instantaneous flow parameter can be decomposed into two part, mean component and fluctuating component respectively, as shown below:

$$u = U + u\prime \qquad \text{Eqn 3- 6}$$

Where U denotes the mean component, and u′ denotes the fluctuating component. RANS equations are given in Eqn 3-7.

$$\text{div}(\mathbf{U}) = 0$$

$$\frac{\partial(U)}{\partial t} + \text{div}(U\mathbf{U}) = -\frac{1}{\rho}\frac{\partial P}{\partial x} + \text{div}\left(\frac{\mu}{\rho}\text{ grad }U\right) + RS_x$$

$$\frac{\partial(V)}{\partial t} + \text{div}(V\mathbf{U}) = -\frac{1}{\rho}\frac{\partial P}{\partial y} + \text{div}\left(\frac{\mu}{\rho}\text{ grad }V\right) + RS_y \qquad \text{Eqn 3- 7}$$

$$\frac{\partial(W)}{\partial t} + \text{div}(W\mathbf{U}) = -\frac{1}{\rho}\frac{\partial P}{\partial z} + \text{div}\left(\frac{\mu}{\rho}\text{ grad }W\right) + RS_z$$

$$\frac{\partial(I)}{\partial t} + \text{div}(I\mathbf{U}) = -\frac{p}{\rho}\text{ div }\mathbf{U} + \text{div}\left(\frac{k}{\rho}\text{ grad }T_{RA}\right) + \Phi_{RA}$$

Where, RS_x, RS_y and RS_z are Reynolds stress terms, and given as:

$$RS_x = \frac{1}{\rho}\left[\frac{\partial(-\rho\overline{u'^2})}{\partial x} + \frac{\partial(-\rho\overline{u'v'})}{\partial y} + \frac{\partial(-\rho\overline{u'w'})}{\partial z}\right]$$

$$RS_y = \frac{1}{\rho}\left[\frac{\partial(-\rho\overline{u'w'})}{\partial x} + \frac{\partial(-\rho\overline{v'w'})}{\partial y} + \frac{\partial(-\rho\overline{w'^2})}{\partial z}\right] \qquad \text{Eqn 3- 8}$$

$$RS_z = \frac{1}{\rho}\left[\frac{\partial(-\rho\overline{u'w'})}{\partial x} + \frac{\partial(-\rho\overline{v'w'})}{\partial y} + \frac{\partial(-\rho\overline{w'^2})}{\partial z}\right]$$

It is noted that the Reynolds stresses, $\tau_{ij} = -\rho\overline{u_i'u_j'}$, are unknown, thus need to be solved or modelled explicitly. Reynolds Stress Model (RSM), which is described in section 3.4, solves all the Reynolds stresses with additional partial differential equations, in contrary, Reynolds Averaged Navier-Stokes (RANS) applies the Eddy Viscosity Model (EVM) which uses the analogy of laminar shear stress to model the Reynolds stresses by defining a term called eddy viscosity, more details will be given in the next section.

3.3. Eddy Viscosity Model

As mentioned previously, RANS equations are not closed by themselves, the Reynolds stresses have to be solved or modelled, this is often called the closure problem. Based on the Boussinesq hypothesis, which states that the Reynolds stress tensor is the product of eddy viscosity and mean strain rate tensor, as given in Eqn 3-9, the Reynolds stresses can be obtained once the eddy viscosity is known, further modelling is required to calculate the eddy viscosity, several approaches are available, such as mixing length model, Spalart-Allmaras, k-ε, k-ω and etc, more details are given in the following sub-sections.

$$\tau_{ij} = \mu_t \left(\frac{\partial U_i}{\partial x_j} + \frac{\partial U_j}{\partial x_i} \right) - \frac{2}{3} \rho k \delta_{ij} = 2\mu_t S_{ij} - \frac{2}{3} \rho k \delta_{ij} \qquad \text{Eqn 3- 9}$$

Where $S_{ij} = \frac{1}{2} \left(\frac{\partial U_i}{\partial x_j} + \frac{\partial U_j}{\partial x_i} \right)$ is the mean strain rate tensor, and δ_{ij} is the Kronecker delta.

3.3.1. Zero Equation Model

Zero-equation-model is also called algebraic turbulence model, there is no additional partial differential equation needed to be solved along with RANS equations. Prandtl (1925) proposed the mixing length hypothesis, which assumes that a fluid particle differs from that of its surroundings by a "mixing length distance", l_m, thus the eddy viscosity is approximated by a algebraic relationship with a multiple of mixing length distance and velocity gradient, as Eqn 3-10. Mixing length approach is simple and very efficient to solve, and usually could obtain acceptable prediction for two-dimensional flow with slow change in flow direction, however it is not that useful in terms of predicting flow with convection and diffusion, which involves the transport of turbulence, separation and circulation will be completely missed. In order to account for these flow phenomena, more details about the turbulence need to be resolved into the turbulence model.

$$\mu_t = \rho l_m^2 \sqrt{S_{ij} S_{ij}} \qquad \text{Eqn 3- 10}$$

3.3.2. One Equation Model

In this case, one additional partial differential equation will be solved, SA was proposed by Spalart and Allmaras (1992) to enable economical computation of external aerodynamics problems, it is one of the most widely used turbulence at this moment. In this approach, kinematic eddy viscosity parameter, $\tilde{v}$, is solved. The eddy viscosity is related to the kinematic eddy viscosity parameter through Eqn 3-11, where f_{v1} is the wall-damping function, which tends to unity for high Reynolds number flow, and approaches zero at the wall.

$$\mu_t = \rho \tilde{v} f_{v1} \qquad \text{Eqn 3- 11}$$

The transport equation to be solved is given as Eqn 3-12.

$$\frac{\partial(\rho\tilde{v})}{\partial t} + \text{div}\,(\rho\tilde{v}\mathbf{U}) = \frac{1}{\sigma_v}\,\text{div}\left[(\mu + \rho\tilde{v})\,\text{grad}(\tilde{v}) + C_{b2}\rho\frac{\partial\tilde{v}}{\partial x_k}\frac{\partial\tilde{v}}{\partial x_k}\right]$$
$$+C_{b1}\rho\tilde{v}\widetilde{\Omega} - C_{w1}\rho\left(\frac{\check{v}}{\kappa y}\right)^2 f_w$$

Eqn 3- 12

Where $\widetilde{\Omega} = \Omega + \frac{\check{v}}{(\kappa y)^2}f_{v2}$, Ω is the mean vorticity, and $\Omega = \sqrt{2\Omega_{ij}\Omega_{ij}}$ with $\Omega_{ij} = \frac{1}{2}\left(\frac{\partial U_i}{\partial x_j} - \frac{\partial U_j}{\partial x_i}\right)$, which is the mean vorticity tensor, σ_v, C_{b2}, C_{b1}, C_{w1} and κ are model constants, and given as follows:

$$\sigma_v = \frac{2}{3} \quad C_{b2} = 0.622 \quad C_{b1} = 0.1355 \quad C_{w1} = C_{b1} + \kappa^2\frac{1+C_{b2}}{\sigma_v} \quad \kappa = 0.4187 \quad \text{Eqn 3- 13}$$

Spalart-Allmaras (SA) model is specially designed for aerospace applications, and recently, it becomes popular in turbomachinery applications. One kinematic eddy viscosity parameter differential equation is solved along with RANS equations, thus the computational cost is slightly higher than the mixing length model. It is capable of predicting boundary layer flow very well even with adverse pressure gradient, and it works well in the wall bounded flow with mild flow separation. It is originally formulated as a low Reynolds turbulence model as stated by Spalart and Allmaras, so the first grid point should be placed close to the wall, with small y+ value, in theory, it is not that suitable for flow with complex geometries due to the difficulty in defining a proper length scale, moreover, it lacks sensitivity to transport process in rapidly changing flows.

3.3.3. Two Equation Model

For two equation models, two additional differential equations are solved, common two equation models are k-ε model, k-ω model and corresponding variants. Two equation model is generally most accurate than zero and one equation models, more information about the turbulence is taken into account, while they are more computational expensive.

k-ε Model

k-ε model is the most widely used turbulence model in engineering application, it can produce reasonably good results for free shear layer flows with small pressure gradients, and wall bounded flow with zero or mild pressure gradients, however, it has poor performance in the case of large adverse pressure gradients. The predictions of the model are insensitive to the free stream turbulence parameters.

The standard k-ε model proposed by Launder and Spalding (1974) has two model equation, for k and ε respectively. The formulation is given below:

$$\frac{\partial(\rho k)}{\partial t} + \mathrm{div}(\rho k \mathbf{U}) = \mathrm{div}\left(\frac{\mu_t}{\sigma_k}\mathrm{grad}\,k\right) + 2\mu_t S_{ij} \cdot S_{ij} - \rho\varepsilon \qquad \text{Eqn 3- 14}$$

$$\frac{\partial(\rho\varepsilon)}{\partial t} + \mathrm{div}(\rho\varepsilon\mathbf{U}) = \mathrm{div}\left(\frac{\mu_t}{\sigma_\varepsilon}\mathrm{grad}\,\varepsilon\right) + C_{1\varepsilon}\frac{\varepsilon}{k}2\mu_t S_{ij} \cdot S_{ij} - C_{2\varepsilon}\rho\frac{\varepsilon^2}{k} \qquad \text{Eqn 3- 15}$$

and the eddy viscosity is modelled as:

$$\mu_t = \rho C_\mu \frac{k^2}{\varepsilon} \qquad \text{Eqn 3- 16}$$

Where σ_k, σ_ε, $C_{1\varepsilon}$, $C_{2\varepsilon}$ and C_μ are model constants and needed to be estimated from experimental data. The general values are given as:

$$\sigma_k = 1.00 \quad \sigma_\varepsilon = 1.30 \quad C_{1\varepsilon} = 1.44 \quad C_{2\varepsilon} = 1.92 \quad C_\mu = 0.09 \qquad \text{Eqn 3- 17}$$

k-ω Model

k-ω model (Wilcox, 1988) was developed in parallel with the k-ε model, it uses specific dissipation rate ω as the second variable, the eddy viscosity can be expressed as Eqn 3-18. k-ω model has superior performance in terms of numerical stability in the viscous sublayer of wall bounded flow, this model does not require explicit wall damping function, it gives good agreement with experimental results for mild adverse pressure gradient flows. However, it is very sensitive to the free stream turbulence parameters, thus is unsuitable for certain complex applications.

$$\mu_t = \frac{\rho k}{\omega} \qquad \qquad \text{Eqn 3- 18}$$

The transport equation for k and ω is given as follows:

$$\frac{\partial(\rho k)}{\partial t} + \text{div}(\rho k \mathbf{U}) = \text{div}\left(\left(\mu + \frac{\mu_t}{\sigma_k}\right)\text{grad } k\right) + \left(\begin{array}{c} 2\mu_t S_{ij} \cdot S_{ij} \\ -\frac{2}{3}\rho k \frac{\partial U_i}{\partial x_j}\delta_{ij} \end{array}\right) - \beta^* \rho k \omega \qquad \text{Eqn 3- 19}$$

$$\frac{\partial(\rho \omega)}{\partial t} + \text{div}(\rho \omega \mathbf{U}) = \text{div}\left(\left(\mu + \frac{\mu_t}{\sigma_\omega}\right)\text{grad } \omega\right) + \gamma_1\left(\begin{array}{c} 2\rho S_{ij} \cdot S_{ij} \\ -\frac{2}{3}\rho \omega \frac{\partial U_i}{\partial x_j}\delta_{ij} \end{array}\right) - \beta_1 \rho \omega^2 \quad \text{Eqn 3- 20}$$

Where σ_k, β^*, σ_ω, γ_1 and β_1 are model constants, and are generally given as follows:

$$\sigma_k = 2.00 \quad \beta^* = 0.09 \quad \sigma_\omega = 2.00 \quad \gamma_1 = 0.553 \quad \beta_1 = 0.075 \qquad \text{Eqn 3- 21}$$

The k-ω Shear Stress Transport (SST) model (Menter, 1992a; 1992b; 1994; Menter et al., 2003) combines several desirable features of k-ε and k-ω models, k-ω model is used in the near wall region and the k-ε model is used near boundary layer edges and in free shear layers. The switching between k-ω and k-ε model is achieved by applying a model coefficients blending function. The SST modelling also modifies the eddy viscosity by forcing the turbulent shear stress to be bounded by a constant multiple of the turbulent kinetic turbulent energy in the boundary layer. This modification improves the prediction of flows with strong adverse pressure gradients and separation.

The transport equation for k is the same as Eqn 3-19, however, the specific dissipation rate transport equation is different and given as follows:

$$\frac{\partial(\rho \omega)}{\partial t} + \text{div}(\rho \omega \mathbf{U}) = \text{div}\left(\left(\mu + \frac{\mu_t}{\sigma_{\omega,1}}\right)\text{grad } \omega\right) + \gamma_2\left(2\rho S_{ij} \cdot S_{ij} - \frac{2}{3}\rho \omega \frac{\partial U_i}{\partial x_j}\delta_{ij}\right)$$
$$-\beta_2 \rho \omega^2 + 2\frac{\rho}{\sigma_{\omega,2}}\frac{\partial k}{\partial x_k}\frac{\partial \omega}{\partial x_k} \qquad \text{Eqn 3- 22}$$

Where $\sigma_{\omega,1}$, γ_2, β_2 and $\sigma_{\omega.2}$ are model constants. The model constants for the two transport equations are given as:

$$\sigma_k = 1.00 \quad \beta^* = 0.09 \quad \sigma_{\omega,1} = 2.00 \quad \gamma_2 = 0.44 \quad \beta_2 = 0.083 \quad \sigma_{\omega,2} = 1.17 \qquad \text{Eqn 3- 23}$$

Menter (1994) proposed a better expression for eddy viscosity with limiters, as given below:

$$\mu_t = \frac{\rho a_1 k}{\max(a_1 \omega; SF_2)} \qquad \text{Eqn 3- 24}$$

Where a_1 is a model constant, and $a_1 = 0.31$, S is the mean strain rate, and $S = \sqrt{2 S_{ij} S_{ij}}$. F_2 is a blending function.

3.4. Reynolds Stress Model

Second moment closure is also called Reynolds Stress Model (RSM), all the Reynolds stresses are solved by the corresponding partial differential equations. One-equation and two-equation turbulence models are all based on the Boussinesq's hypothesis. The Reynolds stresses cannot be correctly predicted in the case of highly swirling anisotropic flow. Only RSM can predict the flow with acceptable accuracy. In total, seven additional partial differential equations (including ε partial differential equation) are solved along with the RANS equations. The computational cost is much higher compared to other low order closures. Linear and nonlinear pressure strain relations are available and works with wall function. Early simulations on a selection of flows with RSM are reported in Launder et al. (1975), the RSM transport equation can be written as:

$$\frac{DR_{ij}}{Dt} = \frac{\partial R_{ij}}{\partial t} + C_{ij} = P_{ij} + D_{ij} - \varepsilon_{ij} + \Pi_{ij} + \Omega_{ij} \qquad \text{Eqn 3- 25}$$

Where $R_{ij} = -\tau_{ij}/\rho = \overline{u_i' u_j'}$, C_{ij} is the convection term, and the terms on the RHS denotes production, diffusion, dissipation, pressure strain and rotation, respectively. The convection, production and rotation terms can be derived and expressed in their exact form, given as follows:

$$C_{ij} = \frac{\partial\left(\rho U_k \overline{u_i' u_j'}\right)}{\partial x_k} = \text{div}\left(\rho \overline{u_i' u_j'} \mathbf{U}\right) \qquad \text{Eqn 3- 26}$$

$$P_{ij} = -\left(R_{im}\frac{\partial U_j}{\partial x_m} + R_{jm}\frac{\partial U_i}{\partial x_m}\right) \qquad \text{Eqn 3- 27}$$

$$\Omega_{ij} = -2\omega_k\left(\overline{u_j' u_m'}e_{ikm} + \overline{u_i' u_m'}e_{jkm}\right) \qquad \text{Eqn 3- 28}$$

Where ω_k is the rotation vector, and e_{ijk} is given as:

$$\begin{cases} e_{ijk} = 1 & \text{if } i \neq j \neq k \text{ and cyclic} \\ e_{ijk} = -1 & \text{if } i \neq j \neq k \text{ and anti} - \text{cyclic} \\ e_{ijk} = 0 & \text{if } i = j \text{ or } j = k \text{ or } i = k \end{cases} \qquad \text{Eqn 3- 29}$$

While the diffusion, dissipation and pressure strain terms are needed to be modelled. Launder et al. (1975) and Rodi (1980) reported the details for the most general models. Here, these terms are simply given as follows:

$$D_{ij} = \text{div}\left(\frac{\nu_t}{\sigma_k}\text{grad } R_{ij}\right) \qquad \text{Eqn 3- 30}$$

$$\varepsilon_{ij} = \frac{2}{3}\varepsilon\delta_{ij} \qquad \text{Eqn 3- 31}$$

$$\Pi_{ij} = -C_1\frac{\varepsilon}{k}\left(R_{ij} - \frac{2}{3}k\delta_{ij}\right) - C_2\left(P_{ij} - \frac{2}{3}P\delta_{ij}\right) \qquad \text{Eqn 3- 32}$$

Where the kinematic eddy viscosity is calculated with:

$$\nu_t = \frac{\mu_t}{\rho} = C_\mu\frac{k^2}{\varepsilon} \qquad \text{Eqn 3- 33}$$

And C_μ, σ_k, C_1 and C_2 are model constants, as given as:

$$C_\mu = 0.09 \quad \sigma_k = 1.0 \quad C_1 = 1.8 \quad C_2 = 0.6 \qquad \text{Eqn 3- 34}$$

The turbulent kinetic energy k is involved in Eqn 3-32, and can be calculated by summation of diagonal Reynolds stresses.

Finally, the last transport equation for dissipation rate is given as:

$$\frac{D\varepsilon}{Dt} = \text{div}\left(\frac{v_t}{\sigma_\varepsilon}\text{ grad }\varepsilon\right) + C_{1\varepsilon}\frac{\varepsilon}{k}2v_tS_{ij}\cdot S_{ij} - C_{2\varepsilon}\frac{\varepsilon^2}{k} \qquad \text{Eqn 3- 35}$$

Where $C_{1\varepsilon}$ and $C_{2\varepsilon}$ are model constants, and given as:

$$C_{1\varepsilon} = 1.44 \quad C_{2\varepsilon} = 1.92 \qquad \text{Eqn 3- 36}$$

3.5. Summary

In this chapter, a brief introduction to the turbulence modelling was given, with discussions on the capability of different turbulence models. Zero-equation model is too simple to include flow details, such that it is not suitable for applications involving transport of turbulence. SA model is a relatively new one-equation model, it can be applied to flow with mild separation, however, it is not able to deal with complex geometries due to the difficult in defining a length scale. Two-equation model is more computational expensive, more details about the turbulence can be taken into account, k-ε and k-ω models are among the most popular turbulence models, the variant k-ω SST model incorporates k-ω and k-ε models, k-ω model is used in the near wall region, and k-ε model is applied to regions far from the wall, the prediction in large adverse pressure gradient is improved with k-ω SST model. Zero-equation, one-equation and two-equation models are all based on the Boussinesq hypothesis, which states that the Reynolds stresses can be expressed with mean strain rates, while RSM is a second moment closure model, the Reynolds stresses are solved explicitly with 6 transport equations. Highly anisotropic flow with strong curvature and rotation can be predicted with very good accuracy. However, the computational cost of RSM model is extremely high, thus it is not always appropriate for certain applications. The most appropriate turbulence model should be selected according the specific application.

Chapter 4

Methods of Investigation

4.1. Introduction

This chapter presents the methods utilized in the investigation. First of all, the assumptions made for this work are given, followed by the introduction to the turbomachinery modelling methods, and then the grid generation process is described, it is critical to have a good quality mesh to obtain acceptable prediction results. After that, the general numerical conditions are described, including the turbulence parameter estimation, boundary condition and interface selection, at the end, the loss localization method is also discussed, and it will employed in the following chapters to identify the regions of high loss generation.

4.2. Assumptions

General assumptions are usually essential before starting an investigation, where simplification is generally required.

1. The centrifugal compressor flow field is assumed to be turbulent, in fact, the flow should be transitional, with regions of laminar and turbulent flows. However, it is generally difficult to predict the transitional flow reliably even with the in-house LES. Commercial solver will be employed in this work, considering the available computational resource and time, only simulation with RANS approach is feasible, full annulus LES would be extremely time-consuming and costly, or even not possible currently.

2. The inflow condition is assumed to be uniform without lose of generality.
3. No heat transfer is assumed to occur between the centrifugal compressor and the environment, the wall is assumed to smooth and adiabatic.

4.3. Turbomachinery Modelling Techniques

The simulation of centrifugal compressor would include the rotating impeller and stationary diffuser at the same time. In Star CCM+, two different approaches are available, Multiple Reference Frame (MRF) and sliding mesh. MRF is useful for steady simulation, while in order to capture the unsteadiness, a unsteady simulation with sliding mesh is essential.

Another problem usually involved in turbomachinery modelling is the impeller-diffuser pitch mismatch, different methods were proposed in literature, such as domain scaling, mixing-plane, phase-lag boundary and harmonic balance method, compared to the ordinary full annulus method, the application of these methods can reduce the computational cost dramatically, only one passage is used during the simulation, domain scaling and mixing-plane methods are relatively easy to implement, while phase-lag boundary and harmonic balance method are very difficult to program. Domain scaling method would scale either the impeller or the diffuser or even both to obtain equivalent pitch angles, and the solidity should be kept constant. One of the representative works is that of Rai and Madavan (1988). Domain scaling method can be applied to both steady and unsteady simulations, however, the scaling would inevitably cause certain level of inaccuracies. Mixing-plane method works to take the circumferential average of the flow parameters, and then passes the information to the next stage according to the interface area. It is only suitable for steady simulation due to the mixing out of unsteadiness at the interface. Phase-lag boundary was first proposed by Erdos and Alzner (1977), it is based on the basic assumption that relative position of impeller and diffuser determines the flow field inside the passage, in other words, the same relative position would give rise to the same flow field. The adjacent passages are approximated with a cyclic procedure, which asymptotically achieves the correct phase between all passage. Harmonic balance method utilizes the Fourier series to transform the unsteady time-periodic problem into steady state problem. It is only

applicable to flows with a regularly repeating flow pattern, Hall, Thomas and Clark (2002) present a detailed description of harmonic balance method.

In star CCM+, mixing-plane and harmonic balance method are available, however, to the author's knowledge, harmonic balance method is not fully developed in Star CCM+ Version 8.04, and the parallelization is not fully implemented. So in this work, steady simulation is conducted with mixing-plane interface and MRF, only one passage is simulated. And unsteadiness is predicted through full annulus unsteady simulation with sliding mesh.

4.4. Grid Generation

To obtain acceptable computational result, a good quality mesh is as important as the solver. Low quality mesh will generally cause convergence problem, while improperly clustered mesh would also produce unacceptable result. In principle, fine mesh should be clustered in the high gradient regions, relatively coarse mesh can be applied in far field regions or even be used artificially to damped out vortices, which otherwise may cause reverse flow at outlet. In this thesis, two types of grids are applied, multi-block structured mesh and polyhedral unstructured mesh respectively.

4.4.1. Block-Structured Mesh

It is well known that structured mesh has many advantages over others, especially, in turbomachinery applications. The cell can be aligned much better with the flow direction, thus reduce the numerical diffusion and aiding convergence. Therefore, block-structured mesh is used for the current work. The impeller blade is very similar to the airfoil, except for the blunt trailing edge, so C-mesh is applied to resolve the near wall boundary layer around the blade. H-mesh is applied in the upstream, downstream and inside the passage. In this unshrouded impeller simulation, the very small tip clearance has to be considered, CH-mesh is employed with several layers of cells to resolve the flow inside the tip clearance. A schematic is given in Figure 4- 1, the blocking strategy is very clearly demonstrated. During the mesh generation process, caution has to be taken to ensure that the first layer

of mesh is located with appropriate y⁺, and several layers of mesh has to be generated inside the boundary layer to resolve the near wall flow properly. Globally, the cell aspect ratio should be less than 10, except for the near wall cells, to resolve the boundary layer, the aspect ratio will be very large, and the cell growing ratio has to be less than 1.2 to achieve more stable and accurate result, although 1.3 is a acceptable value for certain cases. Similarly, the block structured mesh for the diffuser can be created with the blocking strategy shown in Figure 4- 2, the only difference is that there is no tip clearance, and the diffuser blade has curved leading and trailing edge, in the case, the O-mesh has to be applied to resolve the near wall boundary layer.
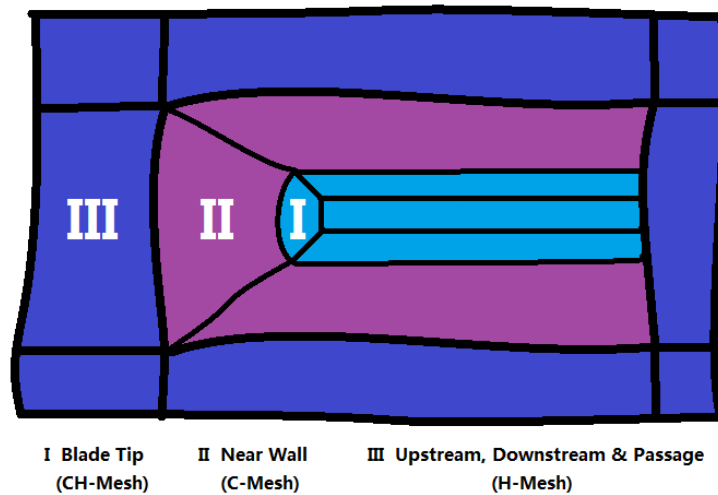

| I Blade Tip | II Near Wall | III Upstream, Downstream & Passage |
| (CH-Mesh) | (C-Mesh) | (H-Mesh) |

Figure 4- 1: Blunt trailing edge impeller blocking strategy.

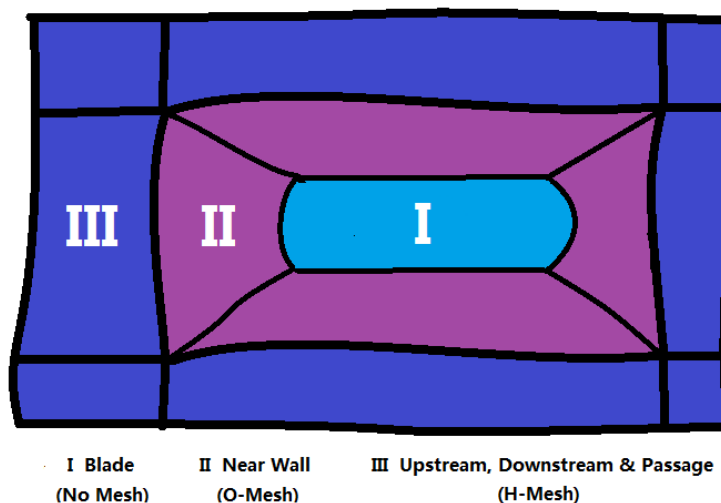| I Blade | II Near Wall | III Upstream, Downstream & Passage |
| (No Mesh) | (O-Mesh) | (H-Mesh) |

Figure 4- 2: Curved leading and trailing edge diffuser blocking strategy.

Ansys ICEM is a commercial grid generation package, which is available in the School of MACE, the University of Manchester. The meshing procedure is that, first of all, the fluid domain is split into a number of blocks, within which the mesh is structured; then the edge parameter is set for each edge of the blocks, and thus the block-structured mesh can be generated easily.

4.4.2. Polyhedral Unstructured Mesh

Polyhedral unstructured mesh is a relatively new concept, although general commercial unstructured solver can deal with it appropriately, the mesh generation itself is a difficult task. CD-adapco Star CCM+ has an embedded mesh generator, which is capable of generating structured, tetrahedral and polyhedral mesh automatically, with certain level of mesh optimization capability. According to CD-Adapco (Peric, 2004), polyhedral mesh can be more promising compared to tetrahedral mesh in terms of total number of cells and dealing with transport property gradient, therefore, polyhedral mesh is adopted in this work for comparison.

In Star CCM+, the polyhedral mesh can be generated together with surface remesher and prism layer. The mesh generation procedure in Star CCM+ is that, the surface mesh is generated at first, and is used as the basis for volume mesh generation. Prism layer mesh is generally employed to resolve the near wall boundary layer region, the prism layers will behave similarly to the structured mesh near the wall. Certain criteria have to be fulfilled to gain some certainty about the generated mesh, according to CD-adapco, the following three criteria should applied to polyhedral mesh, the volume change should be greater than 1E-3, the cell quality should be greater than 1E-6, and the skewness angle should be less than 85 deg. In the near wall region, the criteria for structured should be equally applied to the polyhedral prism layer.

4.5. Numerical Conditions

Numerical simulation is also called numerical experiment, very similar to the physical experiment, the numerical conditions have to be set up properly, such as

the turbulence parameters, boundary conditions, wall treatments and convergence criteria.

4.5.1. Turbulence Parameters Estimation

In order to obtain acceptable computational result, it is critical to have a good estimation of the turbulence parameters at the boundary. The general procedure is given as follows:

Turbulence Intensity Estimation

1. Calculating the hydraulic diameter

$$D_H = \frac{4A}{P} \qquad \text{Eqn 4- 1}$$

2. Calculating the hydraulic diameter based inlet Reynolds number

$$Re_D = \frac{\rho U_{inlet} D_H}{\mu} \qquad \text{Eqn 4- 2}$$

Where U_{inlet} is the inlet average velocity.

3. Estimation of the turbulence intensity

$$I \approx 0.16(Re_D)^{-1/8} \qquad \text{Eqn 4- 3}$$

Turbulence Length Scale Estimation

$$l = 0.07 D_H \qquad \text{Eqn 4- 4}$$

Then the turbulence parameters for different turbulence models can be estimated as follows:

Turbulent Kinetic Energy

$$k = \frac{3}{2}(U_{inlet}I)^2$$
<div align="right">Eqn 4- 5</div>

Turbulent Dissipation Rate

$$\varepsilon = C_\mu^{3/4}\frac{k^{3/2}}{l}$$
<div align="right">Eqn 4- 6</div>

Where C_μ is a model constant and equals to 0.09.

Specific Dissipation Rate

$$\omega = \frac{k^{1/2}}{C_\mu^{1/4}l}$$
<div align="right">Eqn 4- 7</div>

Eddy Viscosity Parameter

$$\tilde{v} = \sqrt{\frac{3}{2}}U_{inlet}Il$$
<div align="right">Eqn 4- 8</div>

4.5.2. Boundary Conditions

For a typical turbomachinery simulation, stagnation inlet and mass flow inlet boundary conditions could be applied, in this case, the mass flow inlet was selected in consideration of the available experimental conditions. The inflow direction was set to normal to the inlet surface, additionally, uniform velocity was used with the estimated turbulence parameters. In order to save the computational time, only a single passage was simulated for steady simulation, thus requires the use of periodic boundary condition at each side of the passage. In the case of full annulus unsteady simulation, there is no need for periodic boundary conditions. Static pressure is specified at the outlet, as well as the temperature.

4.5.3. Wall treatments

Wall treatment is an essential part of the simulation, and it can help predict the near wall flow field, which is usually very important due to the highly viscous and dissipative nature. In Star CCM+, three different wall treatments are available, high-y^+ wall treatment, low-y^+ wall treatment and all-y^+ wall treatment. High-y^+ wall treatment employs the wall function to account for the boundary layer, the near-wall cell should lie within the logarithmic region of the boundary layer. Low-y^+ wall treatment is suitable for low-Reynolds number turbulence model only, the viscous sublayer is assumed to be resolved with near-wall cells. All-y^+ wall treatment is recommended in Star CCM+ User Guide Version 8.04 (CD-adapco, 2013) and is a hybrid treatment, it behaves like high-y^+ wall treatment if the mesh is coarse, and like low-y^+ wall treatment if the mesh is fine enough, it is also capable of dealing with meshes of intermediate resolution. All-y^+ wall treatment is available for SA, k-ε and k-ω models, thus it is used for all simulations in this work.

4.5.4. Convergence Criteria

Numerical simulation is actually a process of solving partial differential equations with numerical method, which produces the approximated rather than exact solution, thus convergence criteria are required to assess whether the approximated solution has been close enough to the exact solution or not. In practice, the exact solution is always unknown, as a result, the difference between successive solutions is used as the convergence criterion, called residual. In CFD, convergence criteria are applied to ensure that the flow field is converged enough, thus produce meaningful flow field prediction. The continuity, momentum and energy residuals are usually monitored, when turbulence models are involved, the turbulence parameter residuals are also need to be taken into account. In this specific application, additional convergence criteria are selected as the torque produced by the rotating impeller and the airwatt. The residuals are generally required to be dropped below 1E-4 for convergence in this work, however, for steady simulation at off design condition, the criteria are relaxed to 1E-3, additionally, the torque and airwatt should flatten out for convergence.

4.6. Loss Localization Method

Although entropy generation has been introduced to quantify the loss occurred inside the turbomachinery, the local loss is more difficult to obtain, while it is the local loss that really affect the design. The knowledge on the position and magnitude of local losses can help the designer to improve the performance through local geometry modification, thus reduce the extent and magnitude of high loss regions.

There are two mechanisms that could be responsible for local entropy generation, e.g. shear strain and thermal gradient. Sciubba (1994) proposed to use these local flow quantities to express the entropy generation and split the entropy generation to two parts, viscous entropy generation and thermal entropy generation respectively, as shown in Eqn 4-9, where μ_e and k_e is the effective eddy viscosity and effective thermal conductivity respectively, and the entropy generation rate is calculated per unit volume, with unit $W/(m^3 K)$. The entropy generations due to viscous effect and thermal effect can be written more explicitly, as given in Eqn 4-10 and Eqn 4-11 respectively, where they are expressed as strain rate and thermal gradient in Cartesian coordinate system.

$$\frac{ds}{dt} = \dot{s} = \dot{s}_V + \dot{s}_T = \mu_e \frac{\Phi}{T} + k_e \frac{\nabla^2 T}{T^2} \qquad \text{Eqn 4-9}$$

$$\dot{s}_V = \frac{\mu_e}{T} \left\{ \begin{array}{c} 2\left[\left(\frac{\partial u}{\partial x}\right)^2 + \left(\frac{\partial v}{\partial y}\right)^2 + \left(\frac{\partial w}{\partial z}\right)^2\right] + \left(\frac{\partial u}{\partial z} + \frac{\partial w}{\partial x}\right)^2 \\ + \left(\frac{\partial u}{\partial y} + \frac{\partial v}{\partial x}\right)^2 + \left(\frac{\partial v}{\partial z} + \frac{\partial w}{\partial y}\right)^2 \end{array} \right\} \qquad \text{Eqn 4-10}$$

$$\dot{s}_T = \frac{k_e}{T^2} \left[\left(\frac{\partial T}{\partial x}\right)^2 + \left(\frac{\partial T}{\partial y}\right)^2 + \left(\frac{\partial T}{\partial z}\right)^2\right] \qquad \text{Eqn 4-11}$$

4.7. Summary

The methods of investigation related to numerical simulation were discussed in this chapter. At the beginning, the turbomachinery modelling methods were introduced. Single passage steady simulation and full annulus unsteady simulation

were employed to investigate the flow behaviour inside centrifugal compressor. Then the numerical conditions on the simulation set-up were described, the boundary conditions would be set to mass flow inlet (or velocity inlet for incompressible flow) and static pressure outlet. As recommended by Star CCM+ User Guide Version 8.04 (CD-adapco, 2013), the all-y^+ wall treatment would be employed throughout this work, the convergence criteria were also determined, the residuals should all drop below 1E-3, the torque and airwatt should flatten out for convergence. At the end, the loss localization method was also discussed, and could be used to identify the regions of high local loss generation.

Chapter 5

Validation of Star CCM+ Solver

5.1. Introduction

Centrifugal compressors are generally of complex geometry, strong curvature, effect of centrifugal force and Coriolis force complicate the flow field, as well as the interactions between different flow features. The flow is viscous, highly unsteady, swirling and transitional. Consequently, it is very difficult to obtain an acceptable prediction.

Star CCM+ is a commercial CFD solver available in the market, and becomes very popular recently, and it is selected as the solver for the current work. This chapter intends to give a brief introduction to Star CCM+ at first, and then solver validation is conducted to verify its capability in predicting the performance and flow field inside centrifugal compressors with the available experimental data.

5.2. CD-adapco Star CCM+ Solver

A number of commercial CFD packages are available on the shelf, Ansys CFX, Ansys Fluent, Numeca Fine, CD-adapco Star CCM+ and etc, they are generally of high cost and very powerful, it is not feasible to buy anyone of them personally. The School of MACE (the University of Manchester) has some of them installed on the Computational Shared Facility (CSF), such as CFX, Fluent and Star CCM+. CSF is a high performance computing cluster built for research groups in the university, it has about 5,000 processors at this moment. Considering the limitation on license,

Star CCM+ is selected for the current work, a maximum number of 64 processors and licenses can be used by any single user at one time under current restriction. Star CCM+ is a multidisciplinary, multifunctional and commercial numerical computation package developed by CD-adapco. Its ability to tackle problems involving multi-physics and complex geometries is unrivalled. Parallelization is implemented efficiently, and was tested up to 16000 cores. It gains its popularity in research communities and companies in recent years. Figure 5- 1 presents the NASA X-34 high angle of attack re-entry simulation results with Star CCM+, the shock wave can be captured properly. Figure 5- 2 shows a UAV with polyhedral mesh, which developed by CD-adapco to produce reliable simulation results with relatively less cells.
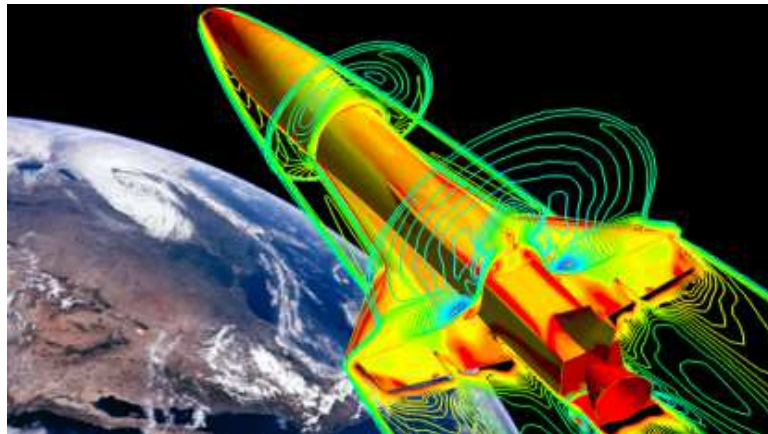
Figure 5- 1: NASA X-34 re-entry simulation with Star CCM+ (Courtesy of TLG Aerospace).
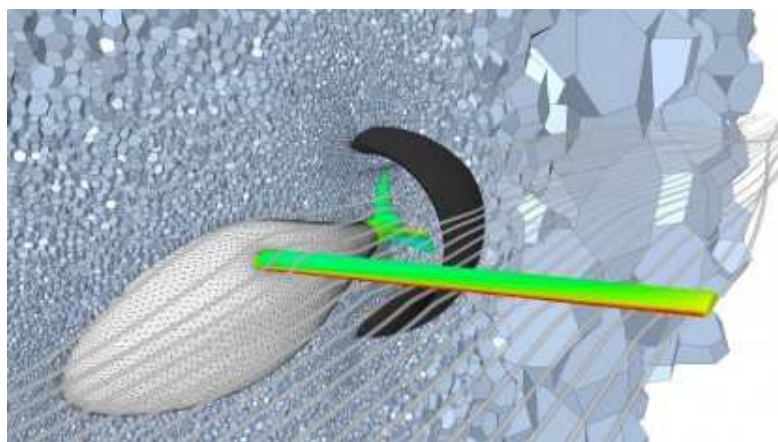

Figure 5- 2: Polyhedral mesh on a UAV (Courtesy of CD-adapco).

Star CCM+ is capable of dealing with both structured and unstructured meshes, both LES and RANS are available for computing turbulent flows. A number of RANS turbulence models are built-in, k-ε, k-ω, SA, RSM and their variants. Incompressible flow and slightly compressible flow can be handled with segregated solver with relatively lower computational cost, on the other hand, coupled solver is computational expensive, however, it can handle highly compressible flow with shock waves and etc. Multigrid method has been implemented to accelerate the computation. For more details, please refer to the Star CCM+ User Guide Version 8.04 (CD-adapco, 2013).

5.3. Validation with Performance Evaluation

Performance is generally the primary concern for a designer, it is the direct reflection of the flow field. The performance validation is conducted with Dyson V2 centrifugal compressor, the experimental data are obtained from Dyson Ltd.

5.3.1. Dyson V2 Centrifugal Compressor

Dyson V2 centrifugal compressor is of complex geometry, with 3D bladed impeller, radial diffuser and axial diffuser. It is of small size, and designed to rotate at
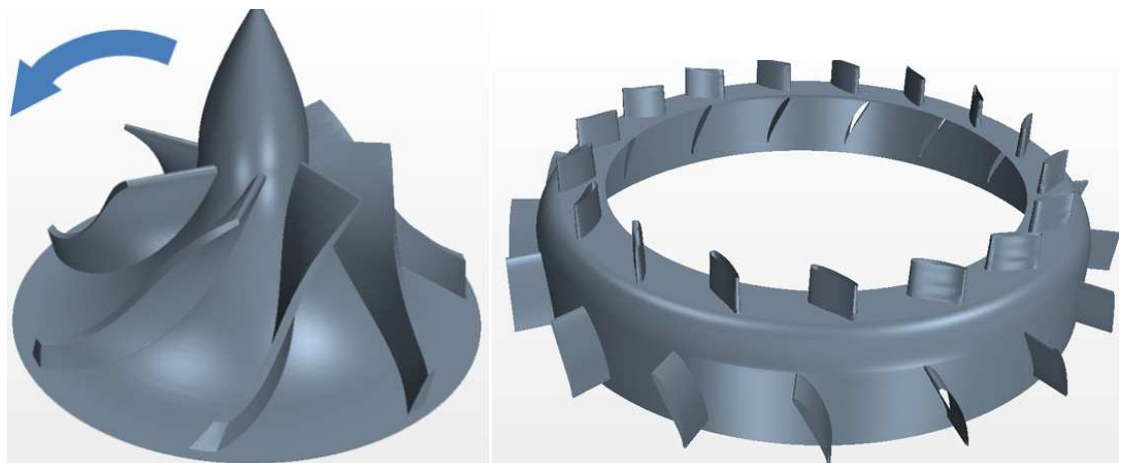

Figure 5- 3: Dyson V2 impeller configuration (including impeller and diffuser).

extremely high speed, as high as 104000 rpm, the impeller tip speed exceeds 100 m/s. As a result, the flow inside is extremely intricate and very difficult to control. It

is located just downstream of the cyclone separator, for which the suction power is provided to separate dust particle from the air. The discharge from the Dyson V2 centrifugal compressor is further used to cool the electric motor which supplies shaft work to the impeller. Figure 5- 3 presents the key components of Dyson V2 centrifugal compressor. The impeller design operation condition is given in Table 5- 1 (according to Dyson Ltd.), as well as the detailed geometric parameters for impeller and diffuser stages.

Operating Conditions	
Rotational speed (design)	85907 rpm
Mass flow rate	0.015252 kg/s
Reynolds number (inlet)	54000
Impeller	
Inlet inner diameter	0.76 mm
Inlet outer diameter	19.84 mm
Outlet diameter	33.10 mm
Blade leading edge span	6.10 mm
Blade trailing edge span	2.51 mm
Number of blades	7
Tip clearance height[*]	0.25-0.26 mm
Backsweep angle	47 deg
Diffuser	
Inlet diameter	36.41 mm
Outlet inner diameter	45.87 mm
Outlet outer diameter	51.80 mm
Number of diffusers	2
Number of blades	17
Radial diffuser blade span	2.76 mm
Axial diffuser blade span[*]	2.49-2.98 mm

Table 5- 1: Dyson V2 centrifugal compressor geometry parameters.

A number of simulation cases have been run at different operation conditions, which are constant power operation conditions according to Dyson Ltd., details are given in Table 5- 2. It is noted that Case 1 corresponds to the impeller design operation condition as presented in Table 5- 1.

	Rotational Speed (rpm)	Mass Flow Rate (kg/s)
Case 1	85907	1.5254E-2
Case 2	89146	1.3087E-2
Case 3	92818	1.0655E-2
Case 4	95084	9.3804E-3
Case 5	97945	8.0837E-3
Case 6	101729	6.8508E-3

Table 5- 2: Dyson V2 centrifugal compressor performance evaluation cases.

5.3.2. Numerical Conditions

Steady simulation is conducted for performance evaluation and flow field analysis, instead of simulating the full annulus configuration, a single passage is simulated for the sake of time and computational cost. Moving Reference Frame (MRF) is employed to account for the relative motion between the impeller and diffuser, k-ω SST turbulence model is applied to deal with the turbulence involved, SA and realisable k-ε turbulence models are also used, the results are compared with that of k-ω SST, more details are given in Appendix A. Figure 5- 4 shows the configuration for the steady simulation, two passages are presented for clarity. In order to enable the single passage steady simulation, rotational periodicity is specified to reduce the full annulus to a single passage, and mixing plane interface is employed to solve the impeller-diffuser blade pitch mismatch problem, thus pass the flow information properly from rotating impeller to downstream stationary diffuser. The block-structured mesh is generated with the aforementioned mesh generation method. Figure 5- 5 and Figure 5- 6 show the block-structured mesh for impeller and diffuser respectively. The mesh at one streamwise location for impeller is presented in Figure 5- 7, the tip clearance is well resolved with several layers of mesh. The inlet boundary is set to mass flow inlet, and static pressure is specified for the outlet, other boundaries are set to no-slip, adiabatic wall.

Figure 5- 4: Dyson V2 steady simulation configuration.

Impeller Blade
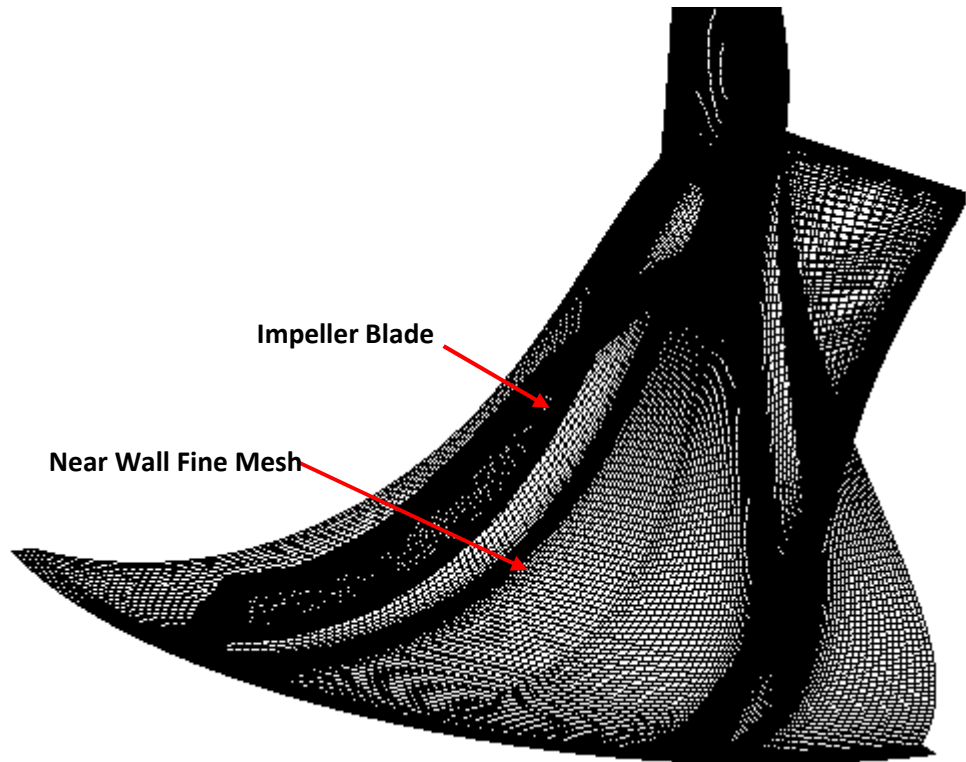
Near Wall Fine Mesh

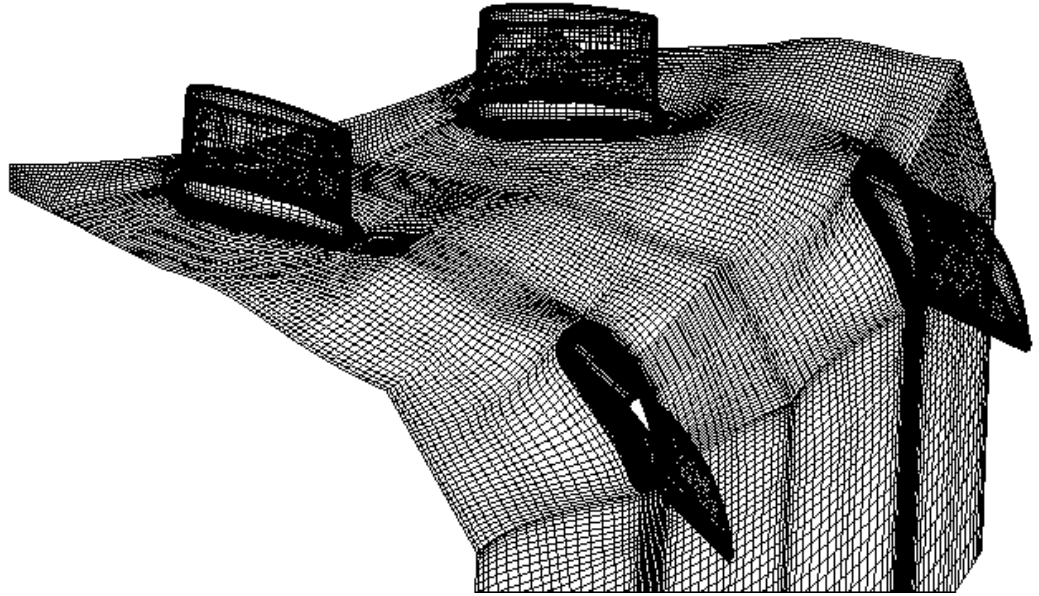Figure 5- 5: Dyson V2 impeller block-structured mesh.

Figure 5- 6: Dyson V2 vaned diffuser block-structured mesh.
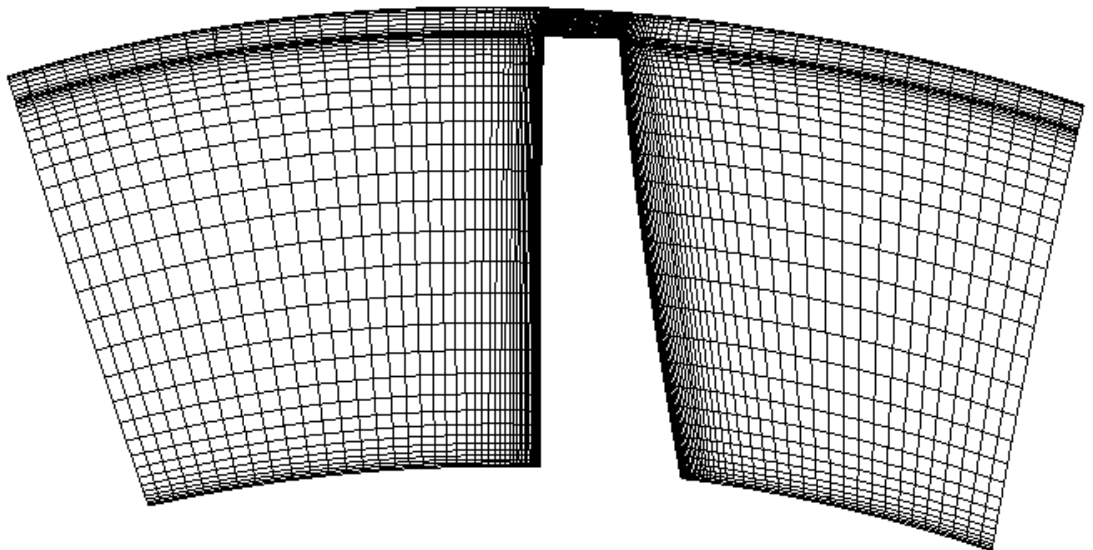

Figure 5- 7: Streamwise cross section mesh for Dyson V2 impeller.

5.3.3. Results

The overall performance curves are plotted in Figure 5- 8 to Figure 5- 10, with regard to airwatt, efficiency and pressure ratio respectively, the numerical results are compared with the experimental results when available. Referring to Figure 5-8, despite the airwatt is over-predicted by the numerical simulation, the computed

airwatt is generally in good agreement with the experimental results, the discrepancy between them is large at high and low mass flow rate, while exact match is observed in between them. It is known that the unexpected skin friction loss during the experiment is relatively higher at high mass flow rate, this could be one of the possible reasons for the discrepancy. It should be noted that turbulence model was employed to deal with the turbulence, and in fact, the flow inside the Dyson V2 centrifugal compressor is transitional, with laminar flow in part of the passage at the design operation condition (e.g. highest simulated mass flow rate), for which the Reynolds number is low, about 54000, and the flow should matches very well with the blade leading edge. It is expected that turbulence model cannot handle the laminar flow properly, as a result, the transition would be hardly predicted with acceptable accuracy. When the mass flow rate is very small, the flow inside the centrifugal compressor becomes highly unstable, from the basic compressor theory, it is known that this highly unsteady flow can be hardly predicted with steady simulation. When the mass flow rate is at the intermediate level, the flow is probably mostly turbulent with the presence of mild separation, while it is still possible to be described as statistically steady flow. Consequently,
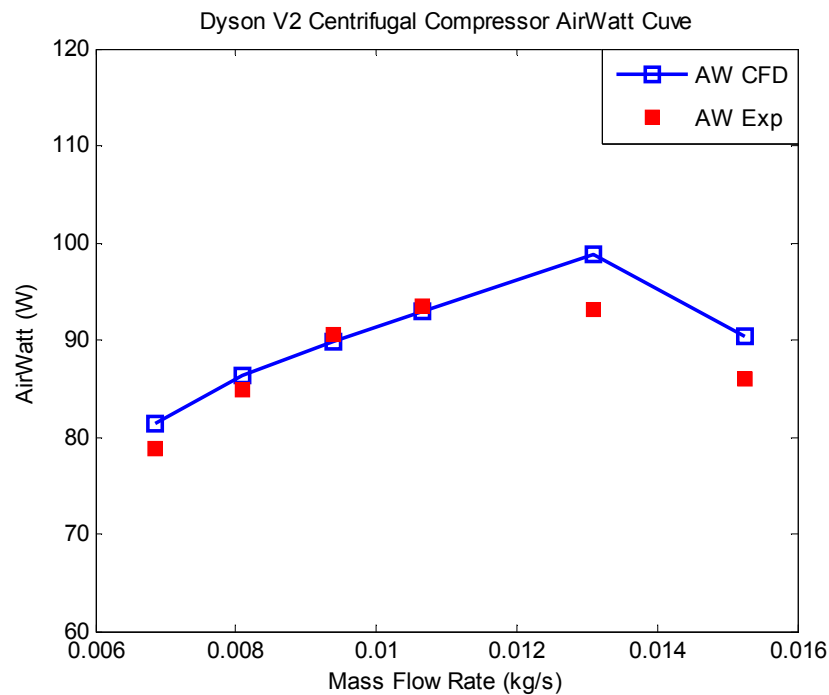

Figure 5- 8: Dyson V2 centrifugal compressor stage performance airwatt curve.

very good agreement can be obtained. The last possible reason for the discrepancy should arise from the turbulence model itself, which is essentially a mathematical model suffering from modelling errors.

Referring to Figure 5- 9, the total-to-total isentropic efficiency and the total-to-static isentropic efficiency for the centrifugal compressor stage are plotted, it was found that the total-to-total isentropic efficiency is higher than the total-to-static isentropic efficiency all the time, because the total-to-total isentropic efficiency considers the kinetic energy at outlet as the obtained energy as well. The general trend for these two curves is similar.
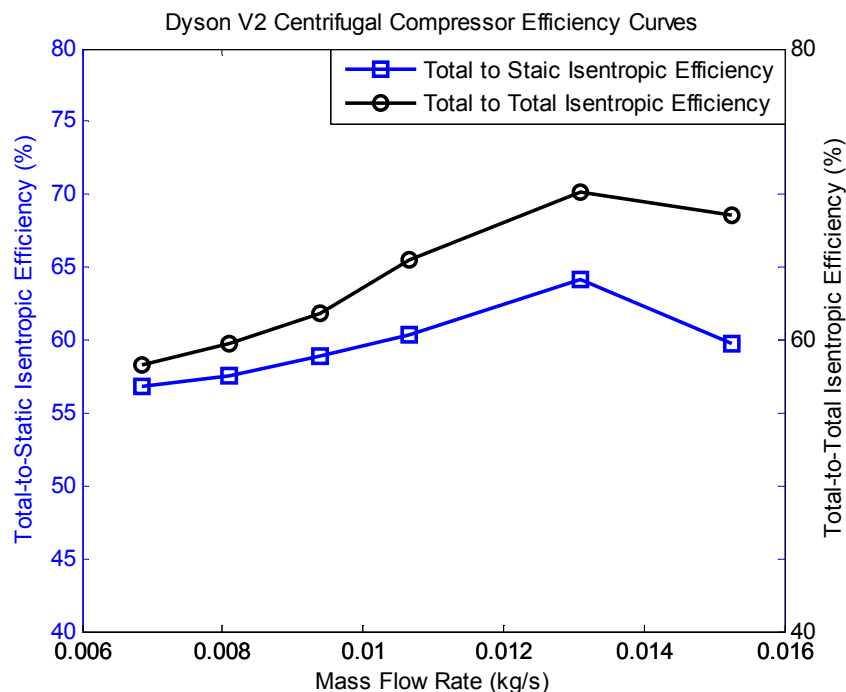
Figure 5- 9: Dyson V2 centrifugal compressor stage performance efficiency curves.

The static and total pressure ratios are plotted in Figure 5- 10, both the pressure ratios are over-predicted at low and high mass flow rate. It is also observed that the curves for these two pressure ratios are almost identical, this may be attributed to the low flow velocity involved. The pressure ratios tend to decrease with the increase in mass flow rate. Because the centrifugal compressor operates at constant power, the increase in mass flow rate would result in a reduction in rotational speed, and it is known that centrifugal force plays the most important role in increasing the pressure in a centrifugal compressor, the decrease in rotational

speed gives lower centrifugal force, and consequently brings about lower pressure ratios.
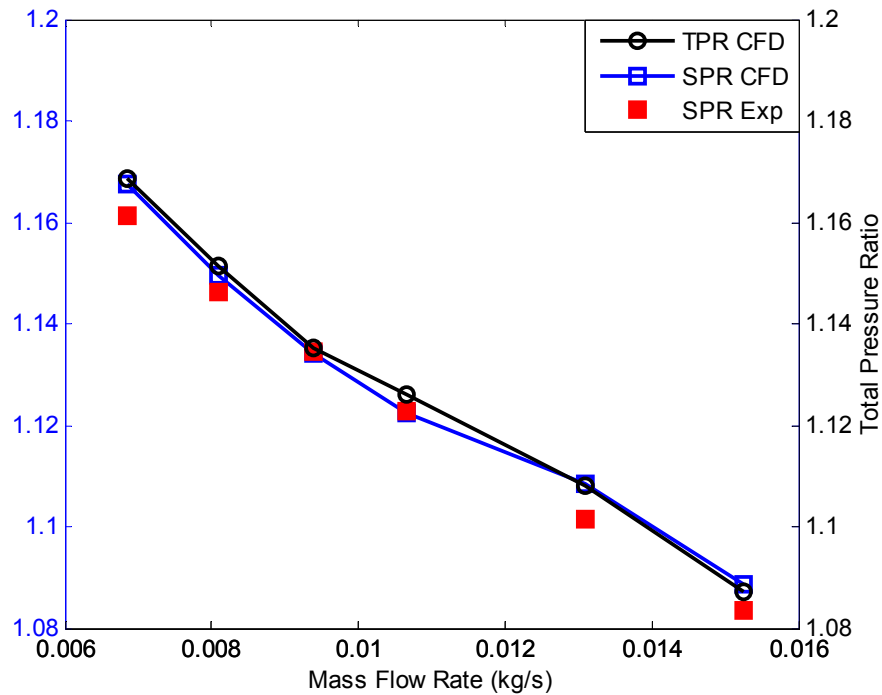

Figure 5- 10: Dyson V2 centrifugal compressor performance pressure ratio curves.

5.4. Validation with Flow Field Analysis

Due to the lack of experimental data on flow field for Dyson V2 centrifugal compressor, a validation centrifugal compressor was obtained from the literature, called ERCOFTAC centrifugal compressor.

5.4.1. ERCOFTAC Centrifugal Compressor

The ERCOFTAC centrifugal compressor is a simplified model with vaned diffuser. It was designed by a team led by Prof Ubaldi at the University of Genova for research purpose, so its size is well suited for taking flow measurements. To facilitate the investigation of different tip clearances, the casing position can be adjusted. With the available profile data provided in Ubaldi et al. (1996), the whole geometry was restored by the author in Solidworks. The casing and the diffuser hub were extended a bit to provide a better outlet boundary condition for the numerical simulation. Figure 5- 11 and Figure 5- 12 show the restored CAD models of

impeller hub & blades and diffuser hub & blades respectively. The basic geometric data and operating conditions are given in Table 5- 3. According to Ubaldi et al., the tip clearance was set to the minimum value of 0.4 mm during their experiment to reduce the tip leakage flow effect. A constant-temperature hot-wire anemometer with single sensor probes was used by Ubaldi et al. to measure the three dimensional unsteady flow field at the impeller outlet, and the static pressure distribution on the impeller casing was measured with fast response pressure transducers along the radial direction. Certain flow field measurements are available and extracted with Matlab, such as the radial and tangential velocities at the impeller outlet, the pressure coefficient on the casing. For more details, please refer to Ubaldi et al. (1996).
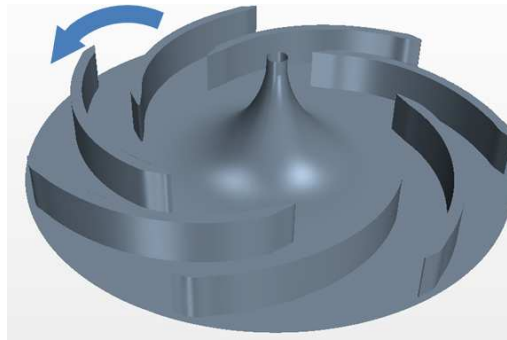
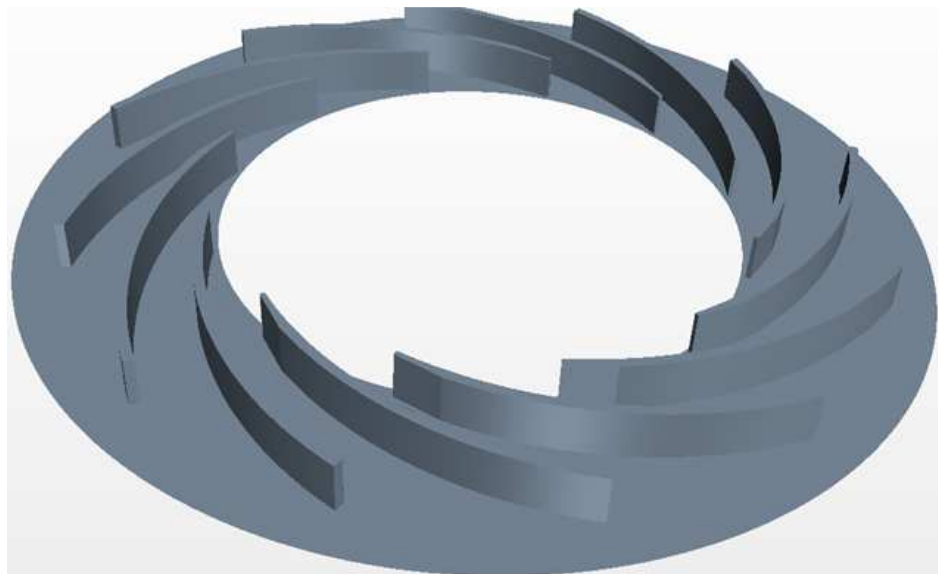Figure 5- 11: ERCOFTAC centrifugal pump 2D blade impeller.

Figure 5- 12: ERCOFTAC centrifugal pump 2D blade diffuser.

Impeller	
Inlet blade diameter	240 mm
Outlet diameter	420 mm
Blade span	40 mm
Number of blades	7
Inlet blade angle	-65 deg
Outlet blade angle	-70 deg
Diffuser	
Inlet vane diameter	444 mm
Outlet vane diameter	664 mm
Vane span	40 mm
Number of vanes	12
Inlet vane angle	-74 deg
Outlet vane angle	-68 deg
Operating Conditions	
Rotational speed	2000 rpm
Flow rate coefficient	0.048
Total pressure rise coefficient	0.65
Reynolds number	650000
Inlet air reference conditions	
Temperature	298 K
Air density	1.2 kg/m^3

Table 5- 3: ERCOFTAC centrifugal pump geometry and operation parameters (Ubaldi et al., 1996).

5.4.2. Numerical Conditions

Full annulus unsteady simulation is conducted for ERCOFTAC centrifugal compressor, sliding mesh strategy is employed to account for the relative motion between the impeller and diffuser. The parameters are updated implicitly in time. Steady simulation is performed with MRF at first to obtain the initialization of the flow field, and then the unsteady simulation is conducted with first-order temporal discretization, after certain iterations, if the residuals cannot go down further, the unsteady simulation is switched to second-order temporal discretization to achieve better convergence. Both k-ω SST and SA turbulence models are used here to deal with the turbulence to make comparisons. The time step is set to the time required by impeller to rotate 1 deg. Polyhedral unstructured mesh is applied, because it is generally easier to obtain, more importantly, all the validation experimental data

were collected by Ubaldi et al. (1996) at the narrow vaneless space between the impeller and diffuser, the resolution of the flow structure is not of interest.

5.4.3. Results

The instantaneous results were measured at different instants with reference to one specific time instant T and at specific radial and circumferential positions, which was chosen by Ubaldi et al. (1996) during their experiment. A non-dimensional time instant is defined as:

$$T = \frac{t}{T_i} \qquad \text{Eqn 5- 1}$$

Where T_i is the rotor blade passing period, as defined as:

$$T_i = \frac{2\pi}{\omega z_i} \qquad \text{Eqn 5- 2}$$

Where ω is the rotor angular speed, and z_i is the impeller blade number.

The instantaneous radial and tangential velocities were extracted from simulation results at the impeller outlet (at $2d/D_i$=1.02, where d is the distance from the centre, and D_i is the impeller diameter) for non-dimensional time instant 0.126, 0.226, 0.326 and 0.426. For example, T=0.426 would mean that the blade has moved a distance about half of the blade pitch.

The instantaneous non-dimensional radial velocities are plotted against non-dimensional circumferential distance and shown in Figure 5- 13 to Figure 5- 16 for different non-dimensional time instants, the corresponding experimental data are included for comparison. The non-dimensional circumferential distance is the circumferential distance normalized by the impeller blade pitch. The black tiangles denote the impeller blade positions, and the black squares denote the diffuser blade positions. It is observed that the computed instantaneous non-dimensioanl radial velocities are generally consistent with the experimental results, however, the peak values are under-estimated with numerical simulations, this could be
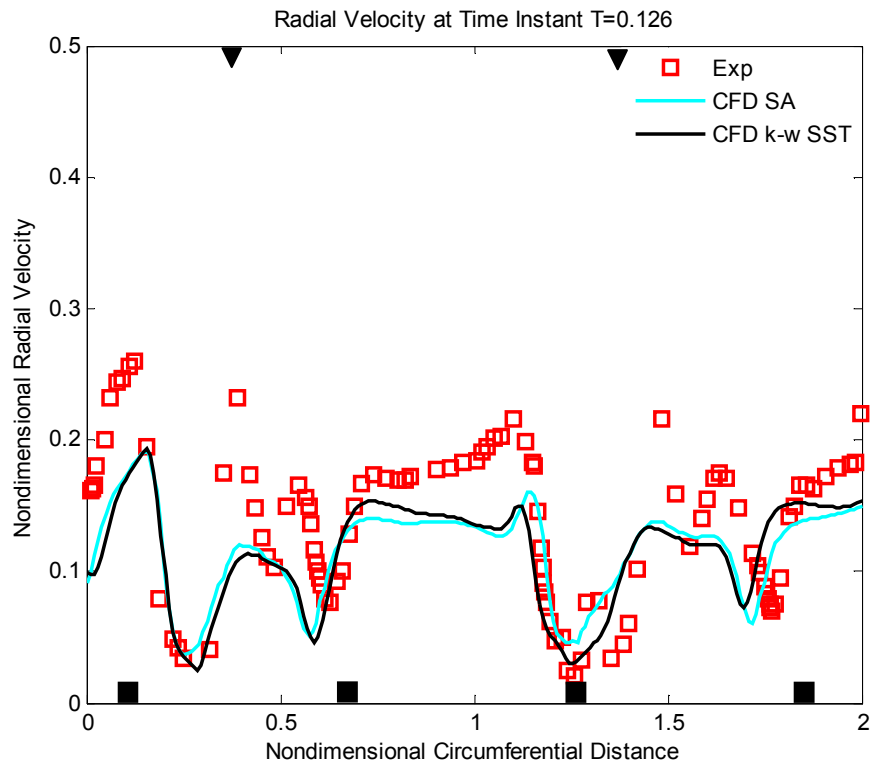
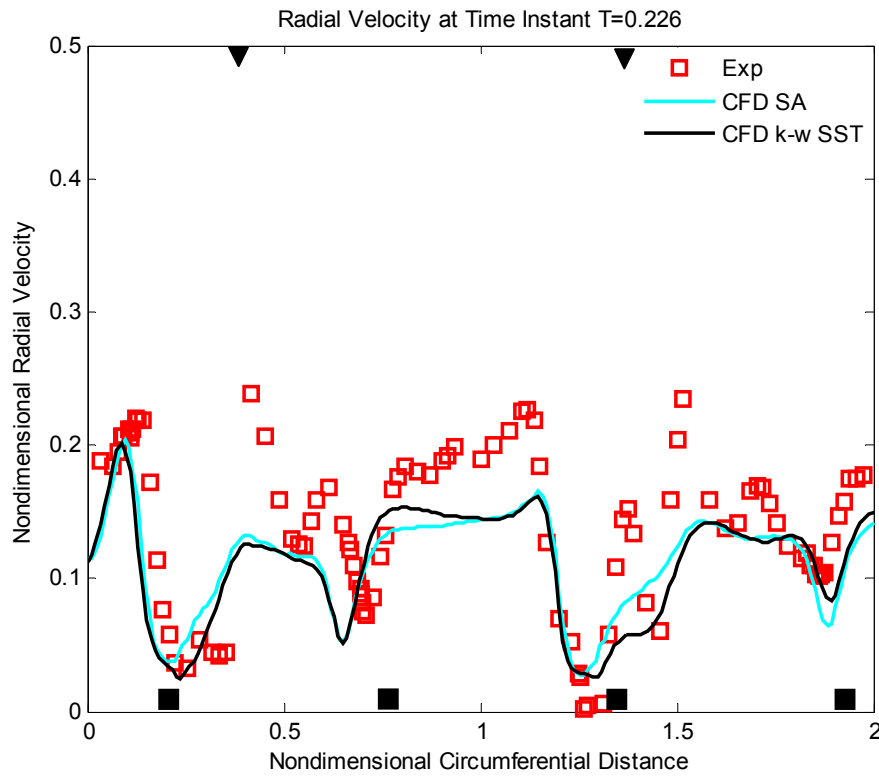Figure 5- 13: Non-dimensioanl radial velocity at time instant T=0.126.

Figure 5- 14: Non-dimensional radial velocity at time instant T=0.226.
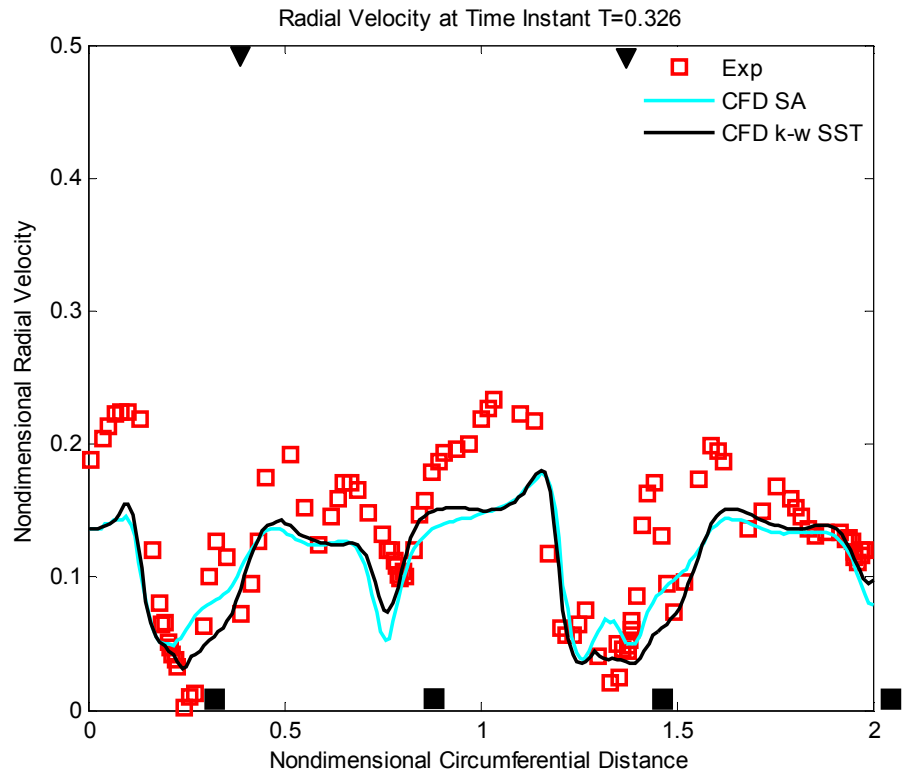
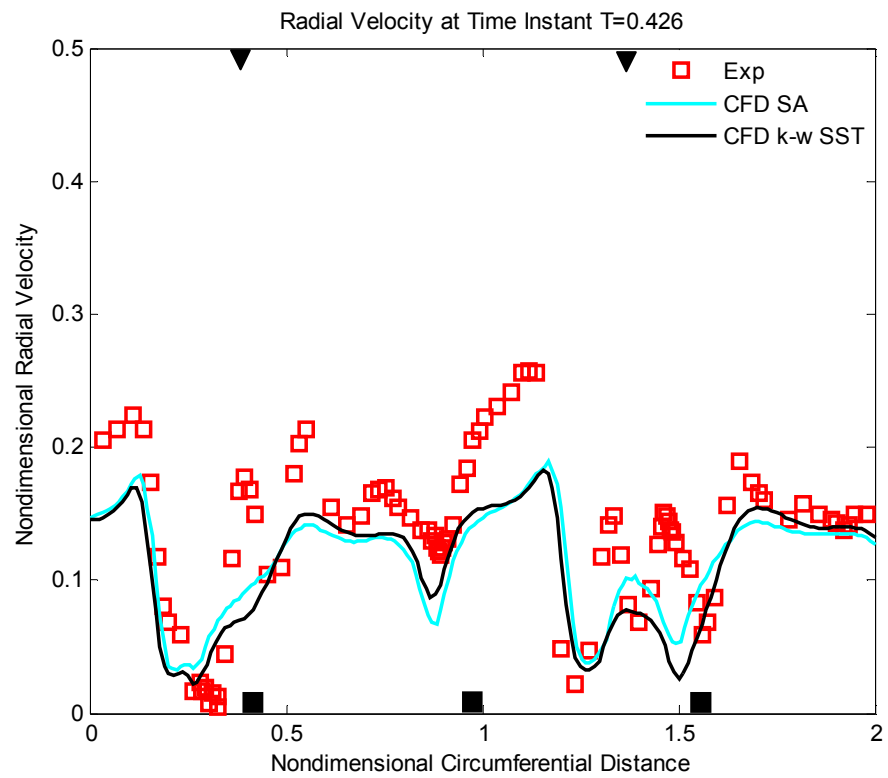Figure 5- 15: Non-dimensional radial velocity at time isntant T=0.326.

Figure 5- 16: Non-dimensional radial velocity at time instant T=0.426.

caused by the presence of diffuser blades, which generate disturbances (back propagation pressure) and cannot be modelled properly by both turbulence models. Another possible reason could be that the employed polyhedral mesh is not fine enough, the disturbances are subject to numerical diffusion, as a result, the magnitude is attenuated. The computed results from both turbulence models are extremely consistent, the flow details are almost eactly the same. It must be also noted that ensemble averaging was used for the experimental data, however, the computed results are instantaneous values due to the computational burden in conducting long physical time simulation, so it should be reasonable to expect certain degree of discrepancy. Well defined wake could also be observed just downstream of the impeller blades. The velocity mimima is generally located at the pressure side of the wake. And tiny troughs are observed to locate just upstream of the diffuser blades due to the deceleration of the air stream caused by the presence of diffuser blades, the "jet-wake structure" is clearly identified as well.
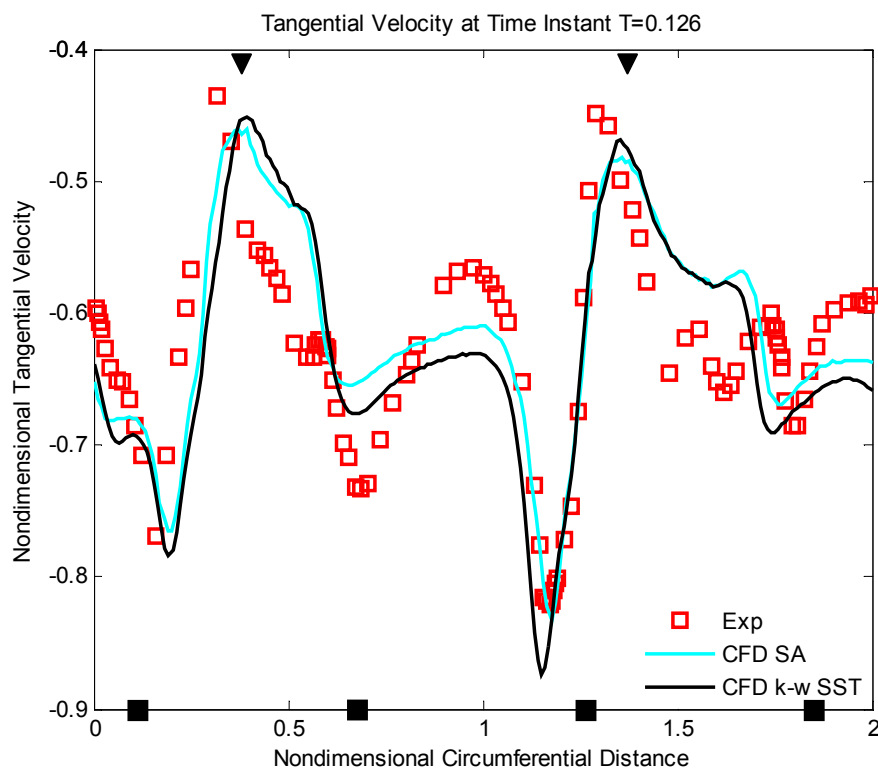

Figure 5- 17: Non-dimensional tangential velocity at time instant 0.126.
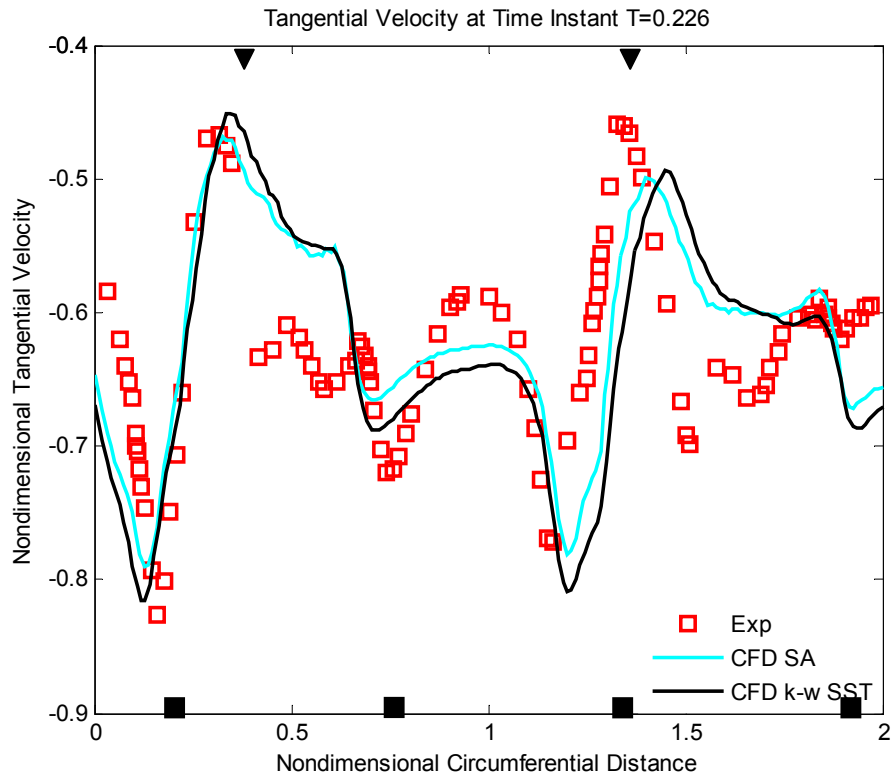
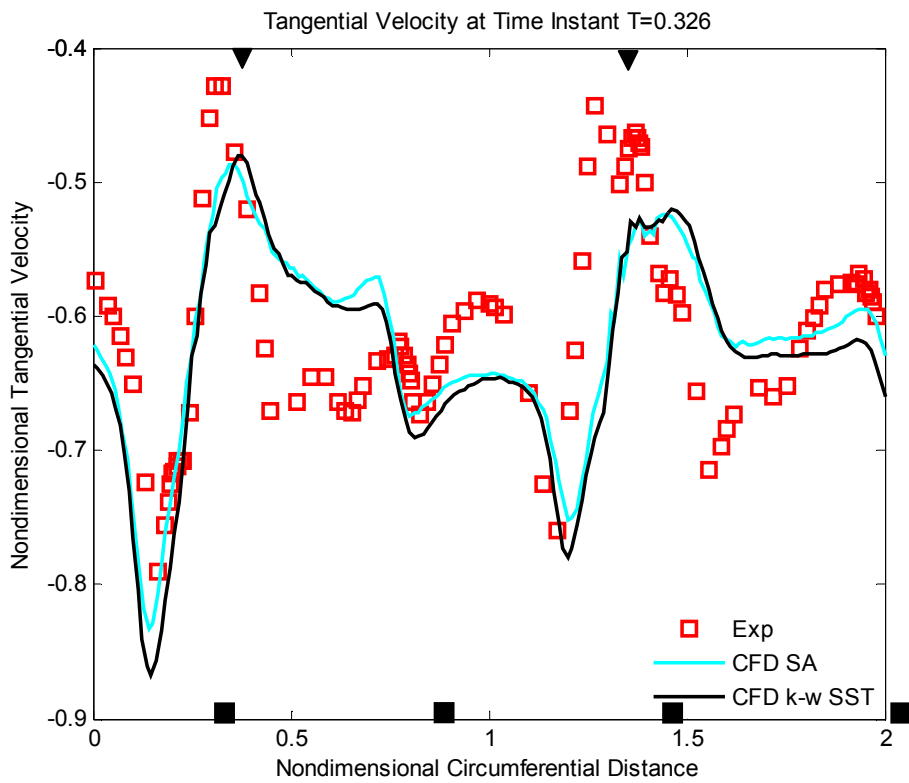Figure 5- 18: Non-dimensional tangential velocity at time instant 0.226.

Figure 5- 19: Non-dimensional tangential velocity at time instant 0.326.
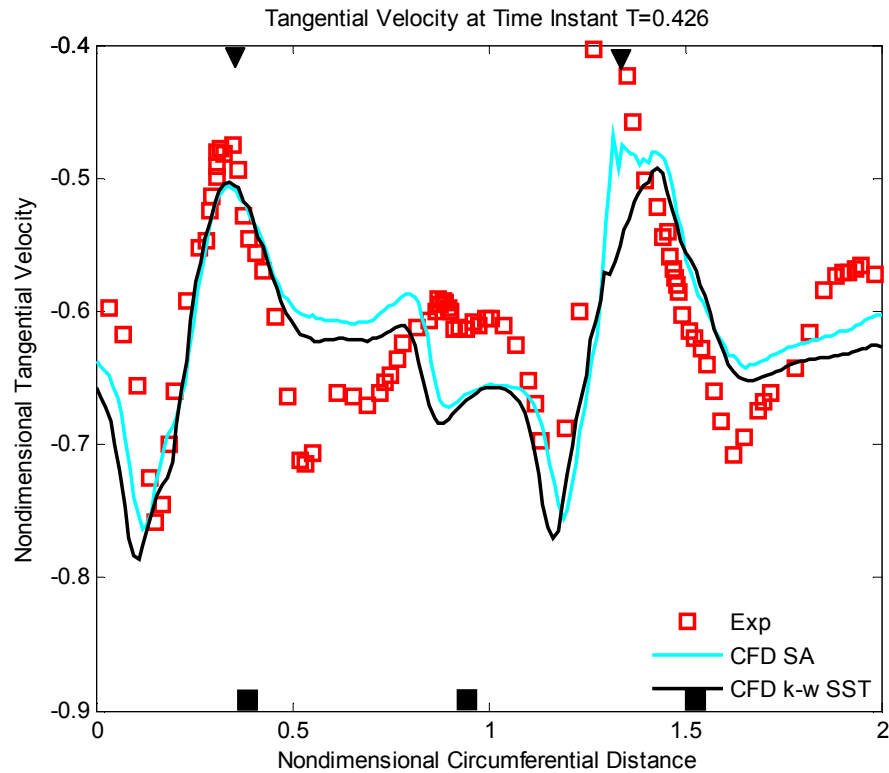
Figure 5- 20: Non-dimensional tangential velocity at time instant 0.426.

Similarly, the instantaneous non-dimensional tangential velocities were plotted against non-dimensional circumferential distance and presented in Figure 5- 17 to Figure 5- 20. The computed results are in good agreement with the experimental data, especially, the peak values are well predicted with both turbulence models. The difference between the predicted results with both turbulence models is extremely small. The minimum absolute tangential velocities corresponds to the presence of wakes, located downstream of the impeller blades, and the maximum absolute tangential velocities all located downstream of the impeller pressure side. Referring to Figure 5- 20, there is a very small absolute tangential velocity, which could be caused by measurement errors during the experiment, the corresponding computed values are well behaved.

5.5. Summary

A series of simulations were performed for the validation of Star CCM+ solver in terms of performance evaluation and flow field analysis.

The validation simulation on performance evaluation was conducted for Dyson V2 centrifugal compressor, with the experimental results provided by Dyson Ltd. Single passage steady simulation with mixing-plane interface and MRF was employed here. Performance curves were plotted, including airwatt, isentropic efficiencies and pressure ratios. The computed results show good agreements with the experimental data, although discrepancies were found due to possible turbulence modelling error, physical modelling error and experimental measurement uncertainties. The results with different turbulence models were presented in Appendix A, k-ω SST turbulence model gives slightly better results compared to SA and realizable k-ε turbulence models.

Due to the lack of flow field measurements on Dyson V2 centrifugal compressor, a validation case was obtained from literature, called the ERCOFTAC centrifugal compressor. Flow field measurements at the vaneless space between the impeller and diffuser are available, the results from the full annulus unsteady simulation were plotted against the experimental results, good agreements were found, although the peak values of radial velocity were generally under-predicted, the trend and flow patterns were similar. k-ω SST and SA turbulence models were compared, exact match between their predicted results were almost obtained, there is no conclusion on the superiority of either k-ω SST or SA turbulence models. However, k-ω SST turbulence model is supposed to have better performance in predicting flow with separation, and it is able to handle flow with complex geometry.

In total, the validation cases on performance evaluation and flow field analysis show that Star CCM+ is suitable for the current application, and can produce acceptable results. k-ω SST turbulence model will be employed in following chapter for further analysis.

Chapter 6

Flow Field Analysis

6.1. Introduction

In this chapter, the flow field analysis is conducted for Dyson V2 centrifugal compressor at Case 1 through single passage steady simulation with k-ω SST turbulence model, with emphasis on the impeller. Steady simulation is good for presenting a general picture of the flow field and much easier to obtain in terms of computational cost, thus it is generally useful during the design process. Different flow features are illustrated and discussed with reference to the performance, so are the primary losses. The predicted wall shear stress and skin friction lines on impeller hub will be used to determine the riblets size in chapter 8. The simulation set-up was given in section 5.1, and will not be described here again. The grid independence study is conducted, three different grid resolutions are examined, and the corresponding results are given in Appendix B.

6.2. Results

Some results are discussed with regard to different regions of the compressor, so Dyson V2 centrifugal compressor has been split into four different regions, impeller, radial diffuser, 90 deg bend and axial diffuser, respectively, as illustrated in Figure 6- 1, different streamwise stations are also shown, stations 1 to 4 are in the impeller region, stations 5 and 6 are in the radial diffuser region, station 7 is in the

90 deg bend region, stations 8 and 9 are in the axial diffuser region, some of the results will be presented for different stations.
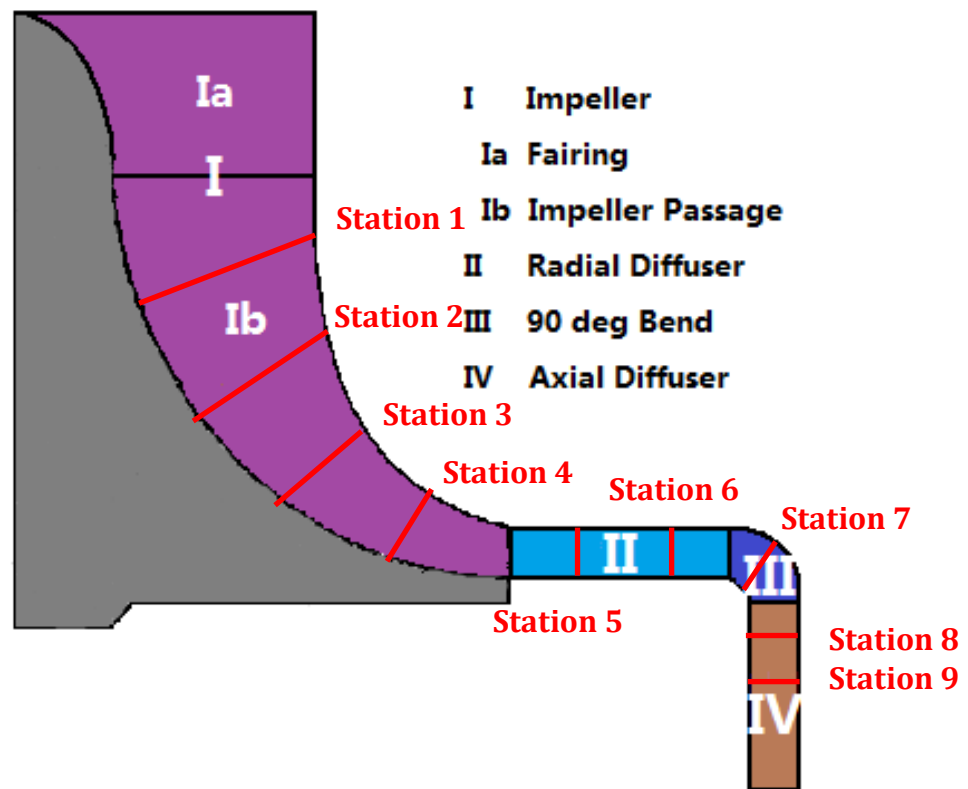

Figure 6- 1: Dyson V2 centrifugal compressor sub-regions.

Figure 6- 2 presents the circumferential-averaged relative Mach number in the impeller meridional plane (including the fairing section). The flow passage is convergent, however, due to the local curvature effect, the flow decelerates and accelerates locally. Near to the hub, the flow accelerates towards the impeller leading edge due to the convex curvature, and then decelerates slightly due to the concave curvature, the flow is gradually diverted from axial direction to the radial direction, and accelerates towards the interface, which is essentially the impeller outlet, concave curvature tends to destabilize the flow, while centrifugal force plays positive role here in accelerating and stabilizing the flow. In contrary, the casing is of convex curvature, the flow is expected to be stabilized, however, due to the tip leakage flow and high adverse pressure gradient, the boundary layer thickens and separates from the casing near to the interface, and then accelerates towards the interface. This restoration from the separation is suspected to be caused by the

strong centrifugal force, which overweighs the curvature effect and adverse pressure gradient, and consequently results in relatively stable flow field.
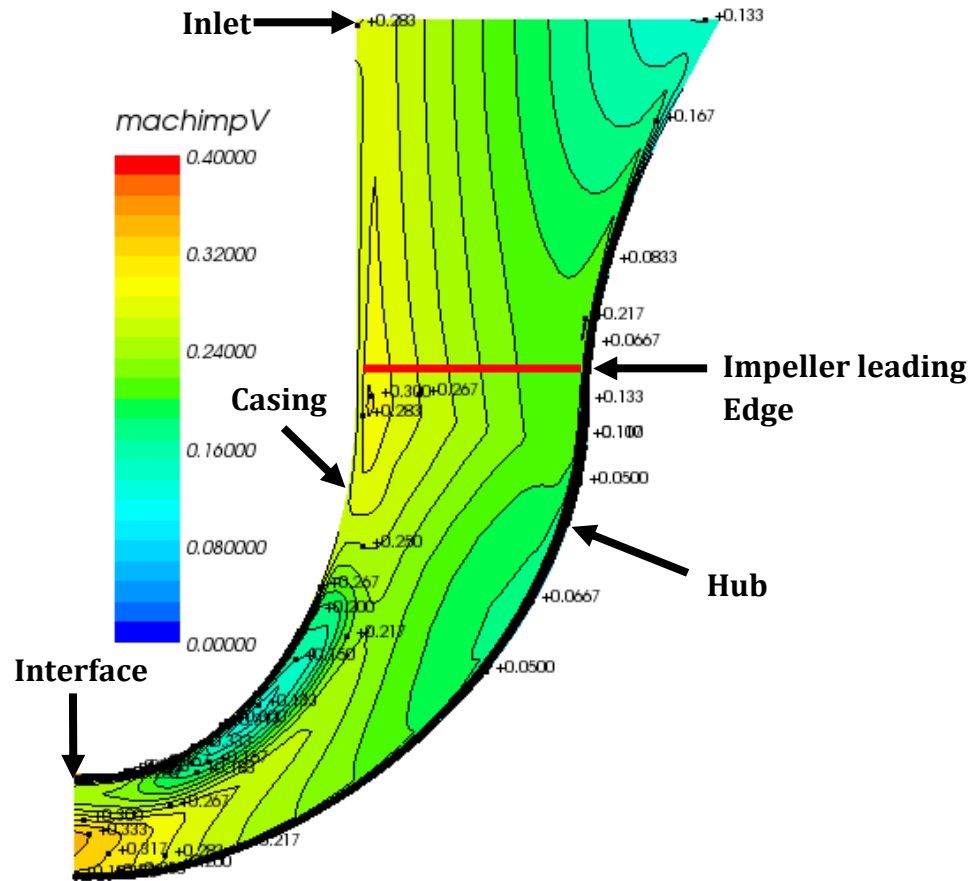

Figure 6- 2: Circumferential-averaged Relative Mach number contour for impeller meridional plane.

Figure 6- 3 and Figure 6- 4 show the relative Mach number contour in impeller S planes at different blade span positions (10%, 50% and 90%). The flow field is relatively smooth in S planes at 50% and 10% blade span, and accelerates towards the interface with only some local deceleration regions, possibly due to the hub/blade corner separation at blade pressure-side. While it is observed that low momentum regions exist in S plane at 90% blade span, which corresponds to the S plane very near to the casing. The flow field is highly distorted, these low momentum regions are attributed to interaction between the near casing endwall boundary layer and tip leakage flow, a vortex is created inside the passage (passage vortex), a clear picture of this vortex is shown in Figure 6- 5, the low momentum

core is marked with the black circle. Q-criterion is also employed to identify the formation path of this passage vortex, it is observed that this passage vortex is initialized near the leading edge and decays towards the impeller outlet, this could be attributed to the effect of centrifugal force, which accelerates the flow and prompts the mixing up. However, the whole evolution process is unknown. Referring to Figure 6- 3, high momentum regions are also observed, they are created due to the blockage effect of the low momentum fluid, the slightly compressible flow would need to accelerate to keep the constant mass flow rate. An interesting feature is that the high momentum fluid resides near to the suction-side, while low momentum fluid stays closer to the pressure-side, this may be caused by the relative motion of the casing and the inertia effect of the tip leakage flow and the fact that suction-side is of lower static pressure. The relative Mach number contour for the impeller outlet is shown in Figure 6- 6, the flow field is highly distorted, the "jet-wake structure" is clearly identified, low momentum fluid locates close to the casing, while high momentum fluid locates near the pressure-side/hub corner, this high momentum fluid is created by the leakage flow at the impeller blunt trailing edge, an extremely low momentum region exists just after the blade trailing edge, it is called the impeller blade wake, this is due to the presence of separation at the blunt trailing edge,
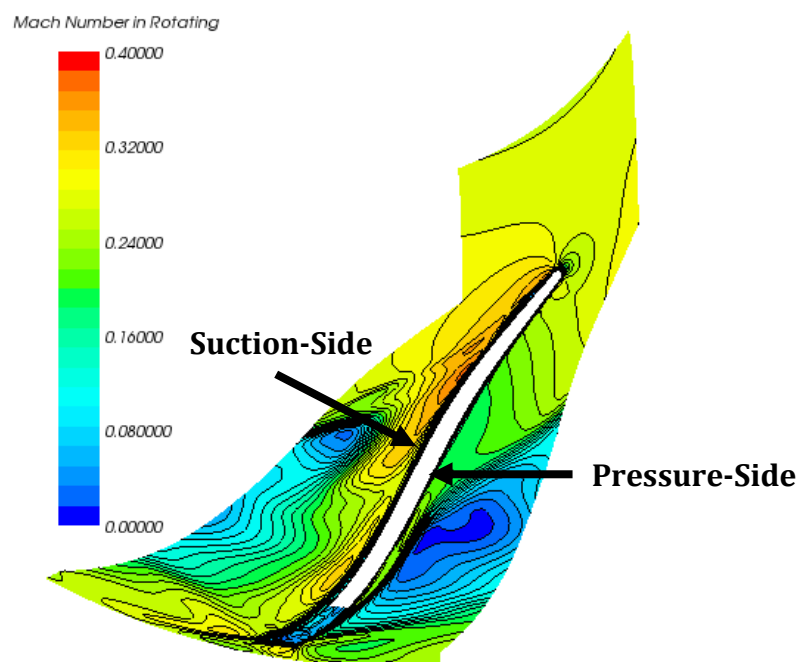

Figure 6- 3: Relative Mach number contour for impeller S plane at 90% blade span.
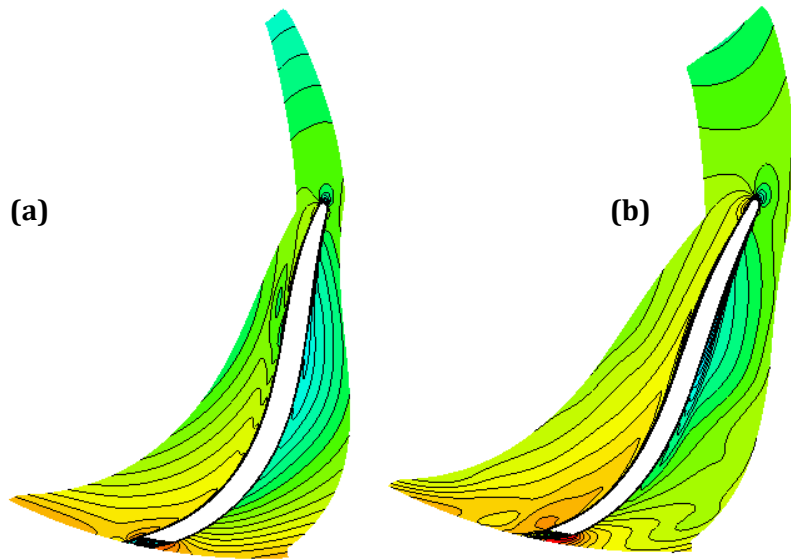
Figure 6- 4: Relative Mach number contour for impeller S planes at a) 10%, b) 50% blade span.
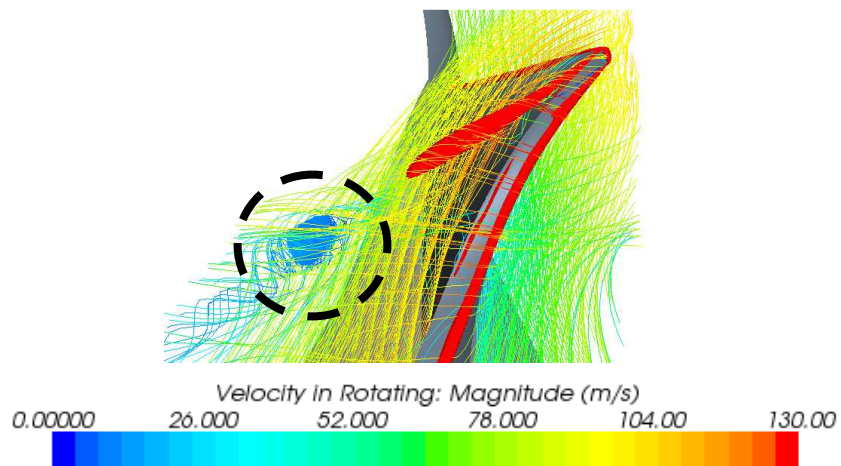

Figure 6- 5: Relative velocity contour on four streamwise stations with streamlines.
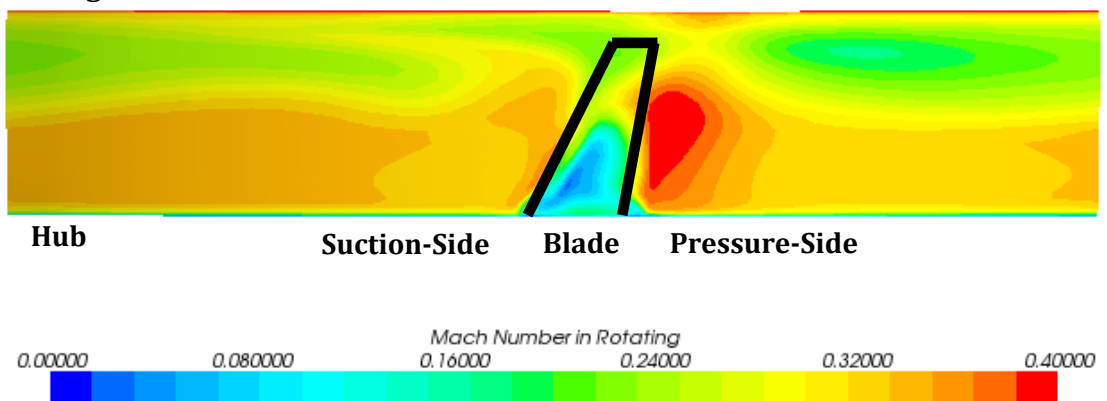

Figure 6- 6: Relative Mach number contour for impeller outlet.

Low momentum regions are observed to exist inside the passage, in order to have more information about these regions, relative velocity contour on stations 1 to 4 are shown in Figure 6- 7, low momentum and high momentum regions are observed and corresponding to those in Figure 6- 3. The premature "jet-wake structure" is very different from that in Figure 6- 6 and similar to that in Figure 6- 3 and Figure 6- 4. The huge difference may be caused by the impeller trailing edge leakage flow and impeller-diffuser interaction. The tip leakage flow is observed to separate from the blade pressure-side and leak to the suction-side without reattachment, possibly due to the very thin blade tip. It is also noted that, although the vortex decays towards the impeller outlet, the low momentum region actually increases in extent, possibly due to the roll-up effect of the vortex. Another distinct feature is that the extent of the tip leakage flow increases towards the impeller outlet, this is attributed to the increase in relative tip clearance size, which is defined as the ratio of local tip clearance to the local blade span, the increase in pressure difference between pressure-side and suction-side also plays a role here.
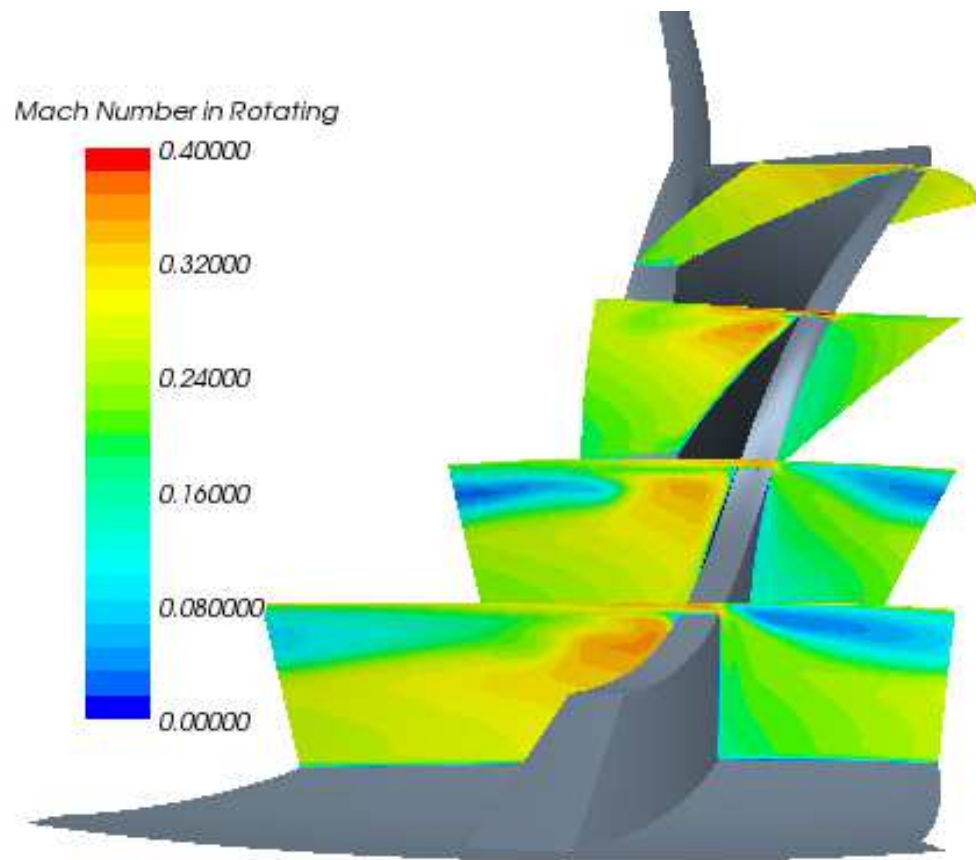

Figure 6- 7: Relative velocity contour on stations 1 to 4.

Figure 6- 8 shows the skin friction lines on the impeller casing, the blue bar indicates the approximate position of the impeller blade. Skin friction lines are generally applied to indicate the flow on the solid surface, and here the endwall flow pattern is clearly presented with the skin friction lines. A separation line is observed to originate from the impeller blade leading edge suction-side, and shed towards the pressure-side on the casing, and finally end near the mid-chord position. This separation line (marked with green bar) corresponds to the formation path of the vortex as shown in Figure 6- 5, the end of the separation line denotes the location of low momentum core and indicates the position where the vortex separates from the casing. It is thus shown that the vortex is created due to the interaction between the endwall flow on casing and the tip leakage flow. Backflow from the impeller outlet and secondary from pressure-side to suction-side are also found due to the adverse pressure gradient.
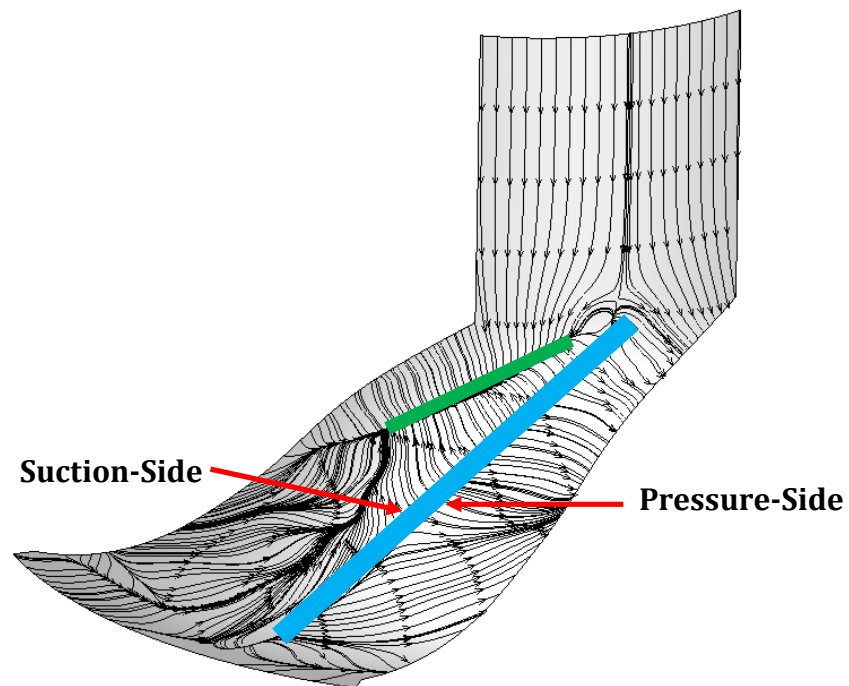

Figure 6- 8: Skin friction lines on impeller casing.

Figure 6- 9 shows the circumferential-averaged static pressure in the impeller meridional plane, the static pressure increases continuously from the impeller inlet to outlet (the impeller outlet is the interface between the impeller and radial diffuser), a low pressure region is observed near the impeller blade leading edge and casing, presumably due to the leading edge separation, while the flow
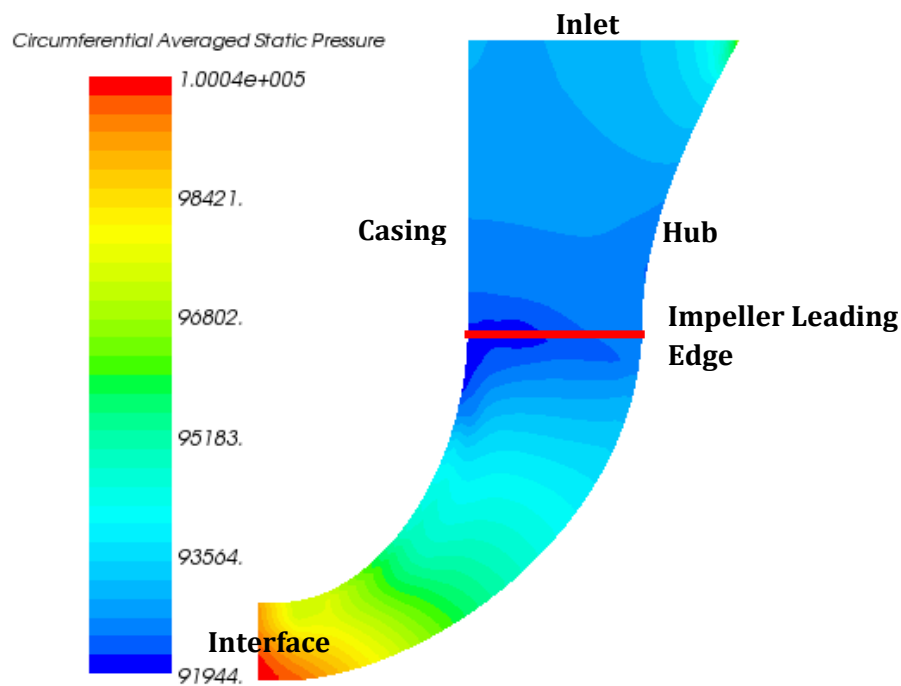
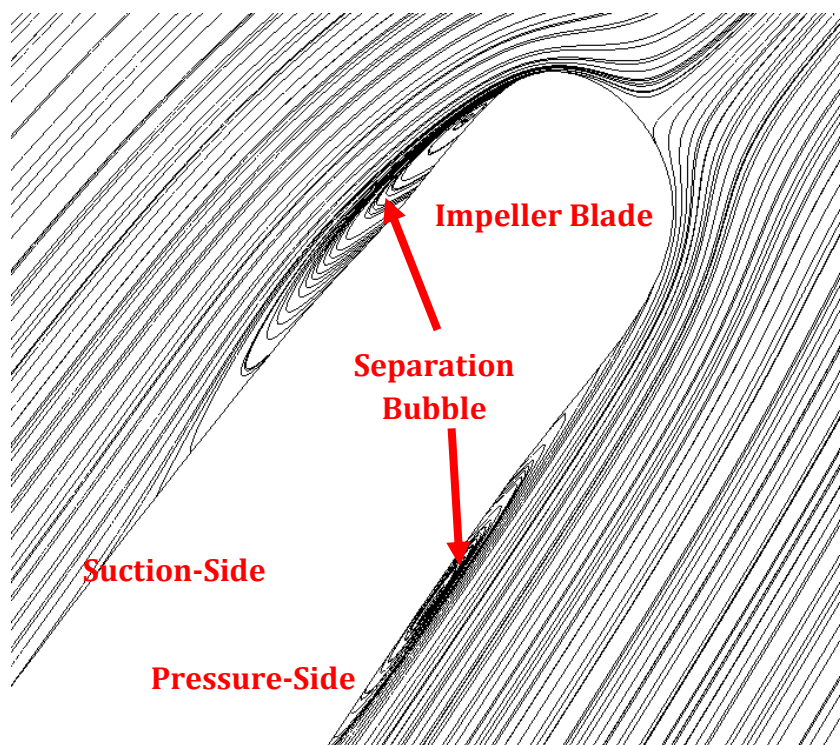Figure 6- 9: Circumferential-averaged static pressure (Pa) contour in the impeller meridional plane.

Figure 6- 10: Velocity vector for impeller S plane at 60% blade span.

reattaches the blade surface and forms a separation bubble, which is confirmed with Figure 6- 10, very near to the impeller blade leading edge, separations are clearly identified on both pressure-side and suction-side due to the local curvature and flow incidence angle.
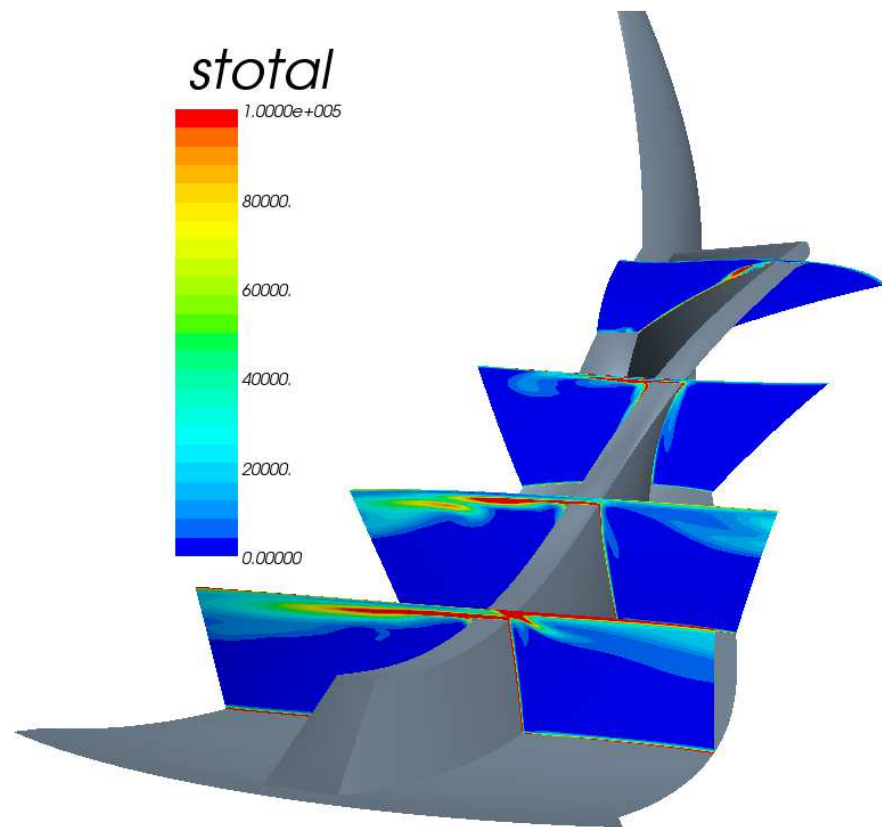

Figure 6- 11: Total entropy generation rate per unit volume $[W/(m^3 K)]$ on stations 1 to 4.

In order to have information on where the loss is actually generated, the loss localization method introduced in section 4.6 is employed. The total entropy generation rate per unit volume on stations 1 to 4 is presented in Figure 6- 11. It is observed that large amount of loss is generated near the blade tip due to the tip leakage flow, especially at the separation point on blade tip near the pressure-side and the interface between the tip leakage flow and the suction-side high speed streamwise main flow, this is caused by the significant shear strain rate at those positions. The loss associated with the passage vortex increases in the axial part of the impeller and corresponds to the vortex formation process, and then reduces

towards the impeller outlet possibly due to the decay of the vortex as described previously. The endwall loss and blade surface loss become significant near the impeller outlet due to the high flow velocity.

Figure 6- 12 illustrates the hub endwall flow and the impeller blade surface flow with the help of skin friction lines. It is observed that the hub endwall flow is in the streamwise direction before the blade leading edge and near to the impeller outlet. The blade surface flow almost goes radially towards the blade tip. These secondary flows are caused by the pressure gradient and centrifugal force. However, the centrifugal force also helps to overcome the adverse pressure gradient near the impeller outlet. Wall shear stress increases towards the impeller outlet due to the increase in flow velocity. The high wall shear stress regions correspond to high entropy generation as given in Figure 6- 11.
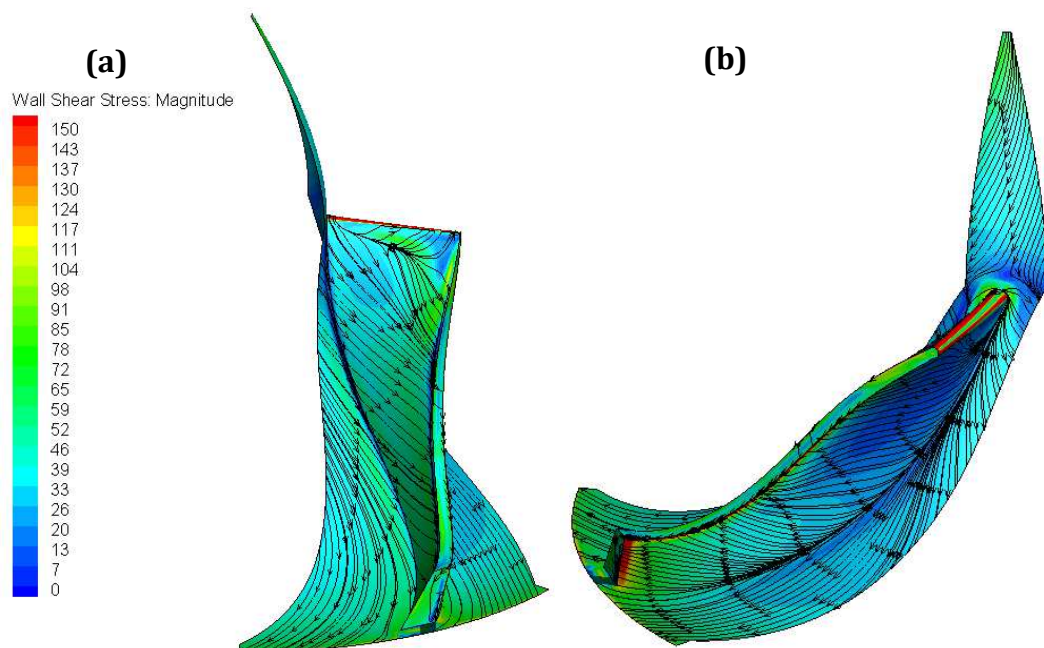

Figure 6- 12: Wall shear stress (Pa) contour with skin friction lines on impeller blade and hub (a) suction-side, (b) pressure-side.

The outflow from the impeller goes into the radial diffuser as the inlet condition, radial diffuser is very critical to the stage performance, the highly distorted flow field may impact the radial diffuser performance significantly due to blockage at the throat and stall inception. The radial diffuser blade sections in spanwise

direction would experience different inflow incidence angles, as a result, local separation may occur. Figure 6- 13 shows the Mach number contour for diffuser S planes at three spanwise positions, 10%, 50% and 90% respectively. Referring to part (a), flow separation is observed at both pressure-side and suction-side in radial diffuser, large regions of low momentum exist particularly inside the 90 deg bend and axial diffuser. Part (b) shows large region of separation only in the axial diffuser. In part (c), early flow separation is observed at suction-side of radial diffuser blade, trailing edge separation is found inside the axial diffuser. The flow separation can be attributed to boundary layer interaction at corner, adverse pressure gradient due to large curvature, and more importantly, the highly distorted inflow condition.
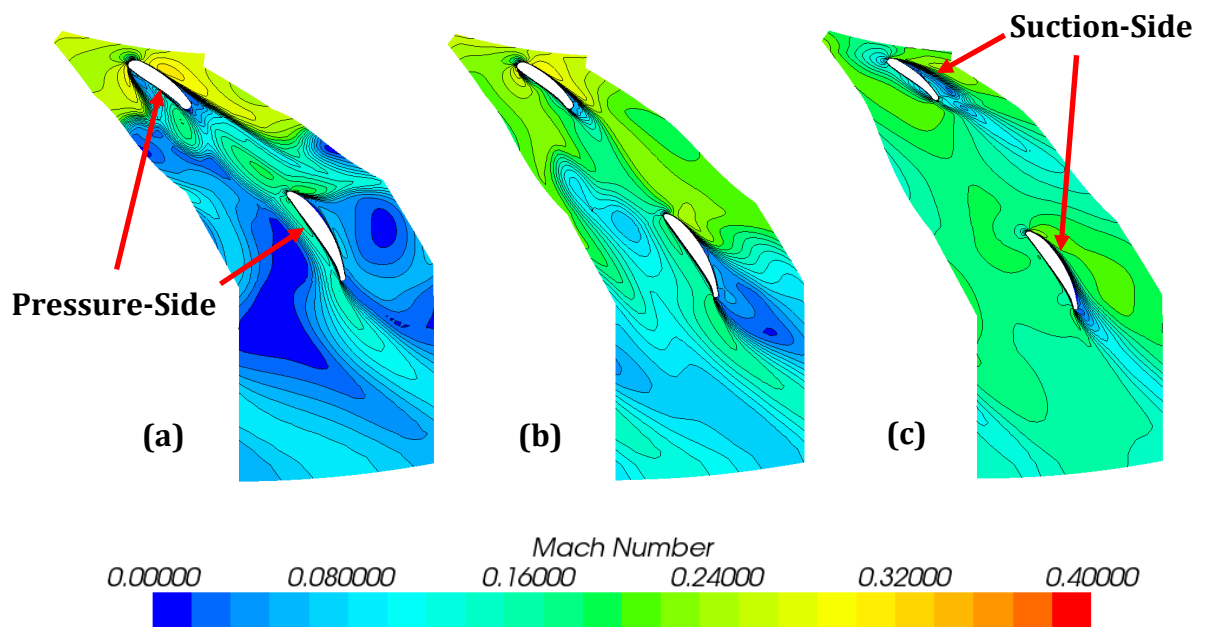

Figure 6- 13: Mach number contour for radial and axial diffusers S planes at (a) 10% span, (b) 50% span, (c) 90% span.

Figure 6- 14 shows the incidence angle for the radial diffuser blade section at different span locations, 10%, 50% and 90% respectively. The dashed box shows the region of interest, because the incidence angle is generally defined for the upstream. It is found that the incidence angle is negative for the blade section at 10% span, and this blade section is subject to pressure-side separation, the situation is very similar to the case of high mass flow rate operation, while for the blade section at 90% span, the incidence angle is positive, suction-side separation occurs at mid-
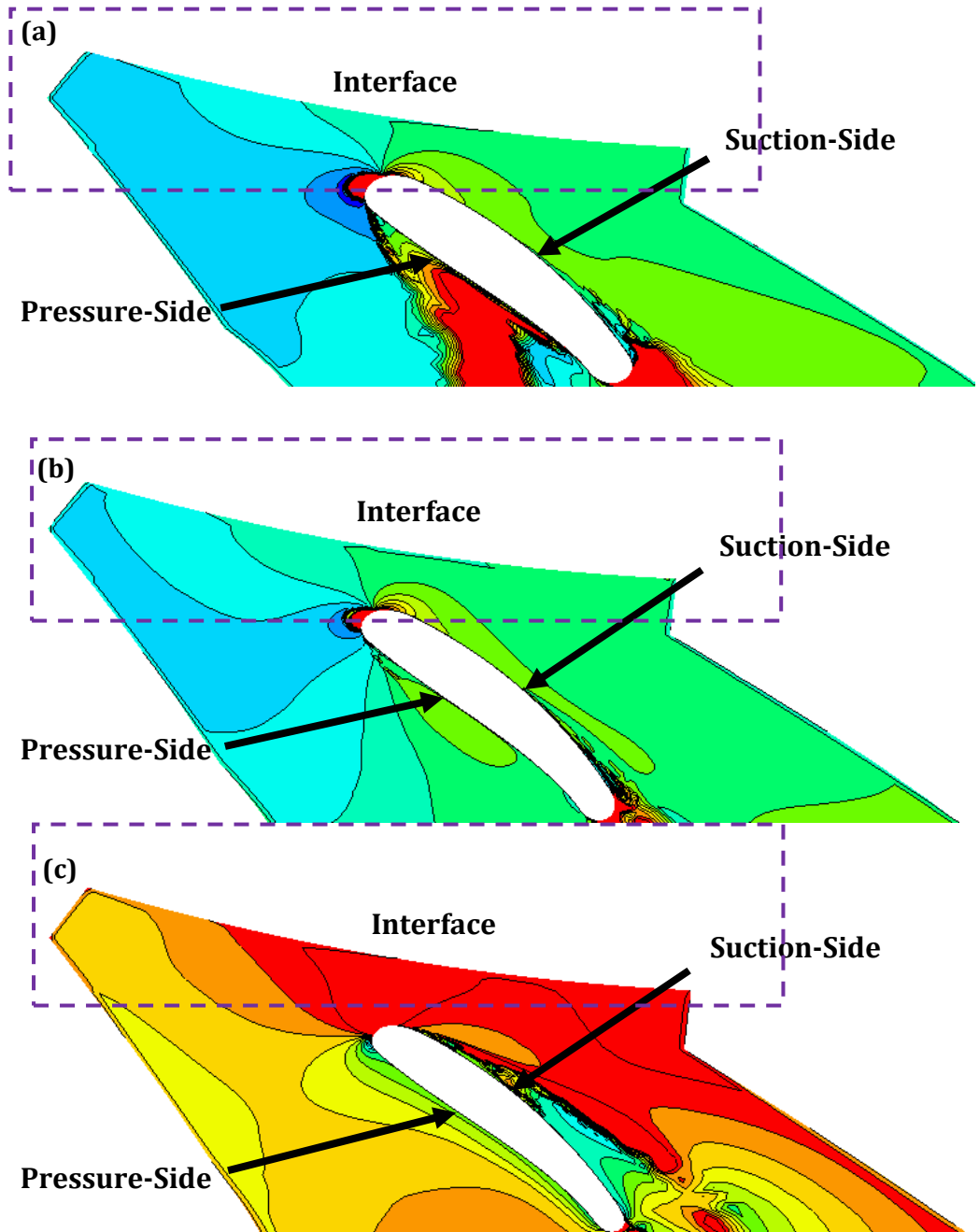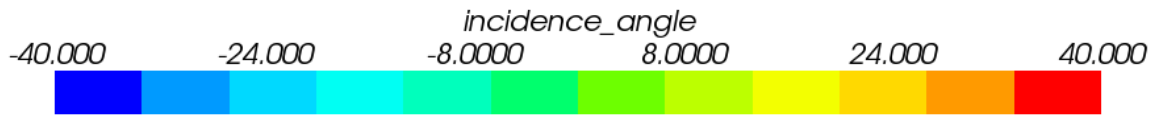
Figure 6- 14: Incidence angle (deg) contour for radial diffuser at (a) 10%, (b) 50%, (c) 90% blade span.

chord position, resembles the low mass flow rate operation. Only the blade section at 50% span works relatively efficiently. As a whole, it can be imaged that the radial diffuser is actually not very efficient, and perform badly even at near design operation condition (stage).
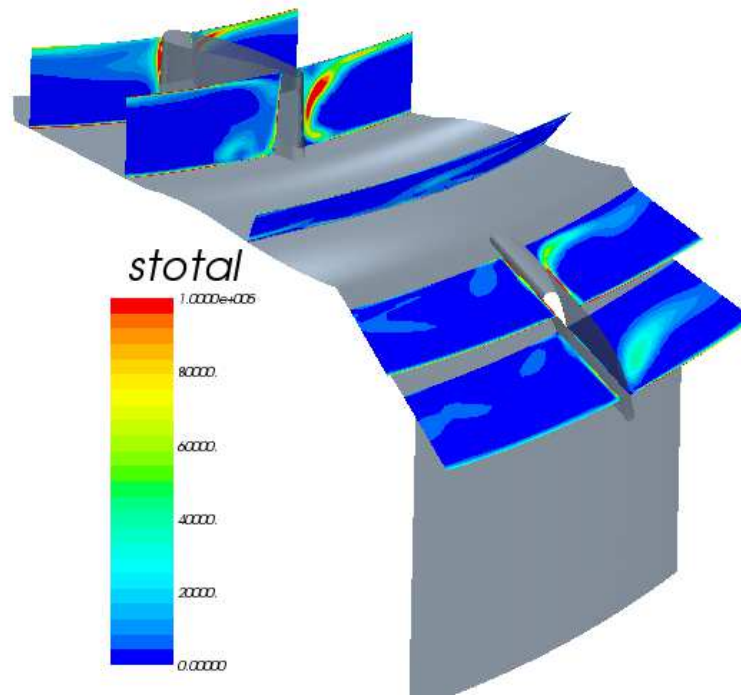

Figure 6- 15: Total entropy generation rate per unit volume [W/(m^{3}K)] on stations 5 to 9.

Figure 6- 15 shows the total entropy generation rate per unit volume on stations 5 to 9. Relatively high local loss generation is observed at both blade suction-side and pressure-side in radial diffuser due to the flow separation, similar high local loss generation is also observed at the axial diffuser suction-side. Hub endwall loss is significant near the radial diffuser inlet, while it is difficult to distinguish the blade surface loss from the separation induced loss.

The circumferential-averaged static pressure contour for the radial diffuser and axial diffuser is shown in Figure 6- 16, very low pressure region is observed near the interface due to the "jet-wake structure" from the impeller and previously mentioned severe separation at the radial diffuser blade. High pressure region is observed at the outer side the 90 deg bend, while low pressure region is observed at the inner side the 90 deg bend, this is due to the presence of centrifugal force induced pressure gradient.
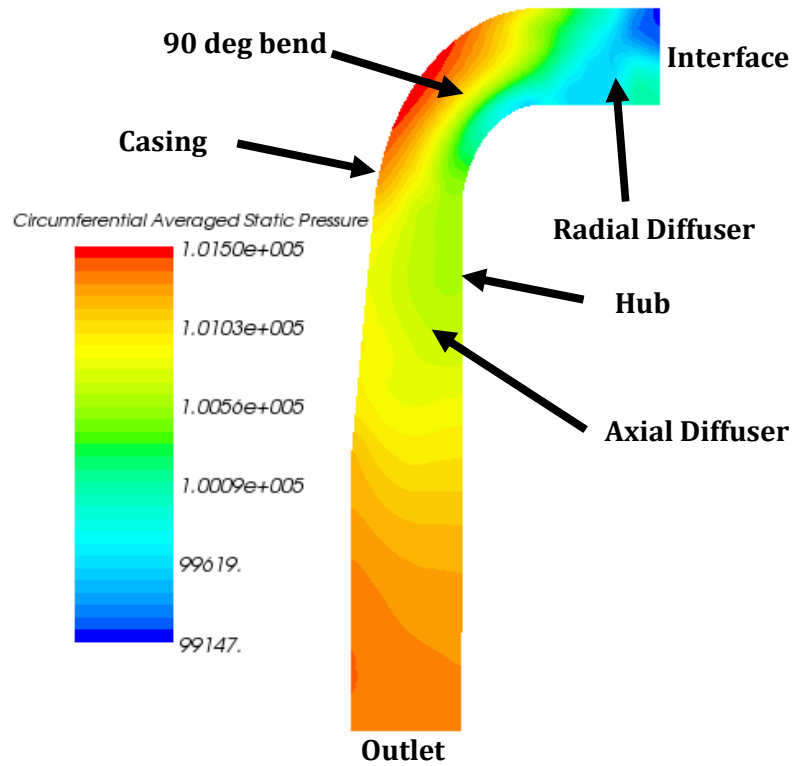
Figure 6- 16: Circumferential-averaged static pressure (Pa) contour for radial and axial diffusers at meridional plane.
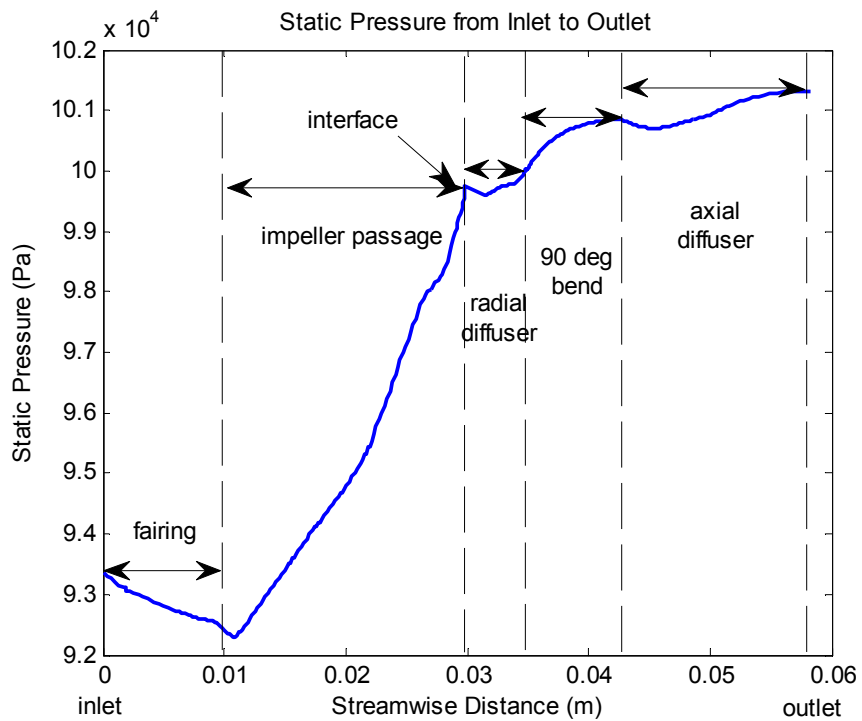

Figure 6- 17: Cross-section-averaged static pressure in streamwise direction.

Figure 6- 17 shows the cross-section-averaged static pressure plotted in the streamwise direction from compressor inlet to outlet, including fairing, impeller passage, radial diffuser, 90 deg bend and axial diffuser. It is observed that the static pressure drops in the fairing region, which is essentially a convergent section, the flow field is only slightly affected by the rotating hub via the skin frication, and it dips slightly after the impeller leading edge due to the previous mentioned leading edge separation bubble. After that, the static pressure rises continuously towards the impeller outlet, a striking feature is that almost 80% of the static pressure arises from the impeller. The static pressure only increases slightly in the radial diffuser due to the highly distorted inflow condition, the diffuser blade cannot recover the static pressure efficiently, very similar situation is observed for axial diffuser, except the impeller, the 90 deg bend contributes the greatest to the static pressure rise. In total, this plot shows that the diffusers are actually not designed to work efficiently under the highly distorted inflow condition.

6.3. Summary

The flow field inside the Dyson V2 centrifugal compressor was analysed in this chapter using steady simulation, with the impeller operating at design condition (Case 1), while the whole stage operated at near design operation condition. Distinct flow features were observed, such as tip leakage flow, separation bubble, the so called "jet-wake structure" and corner separation. The vortex roll-up process was identified, the tip leakage flow from the impeller leading edge plays the role of initializing the vortex roll-up, tip leakage flow from the first half of the impeller blade chord contributes to the formation of the vortex, while that from the rest of the blade chord plays an important role in the decay of the vortex, severe blockage and loss are associated with the vortex inside the passage. Towards the impeller outlet, the vortex decays presumably due to the accelerating effect of centrifugal force. The main mechanisms for loss generation were identified, tip leakage flow is the most significant source of loss generation in impeller, it induces losses from both vortex roll-up and blade tip high shear flow, in general, tip leakage flow is difficult to control and cannot be avoided. Endwall loss and blade surface loss also contribute to the loss generation in impeller, especially in the regions near the

impeller outlet. The losses in both radial diffuser and axial diffuser can be summarised as endwall loss, blade surface loss and separation induced loss. In this work, riblets is proposed to reduce the endwall loss on the impeller hub, the wall shear stress predicted with steady simulation will be used to design the riblets in chapter 8. The diffuser inflow condition is primarily characterized by the highly distorted flow, which makes the diffuser work very inefficiently, as a result, only about 8% of the static pressure rise is obtained through the diffuser. while the impeller accounts for about 80% of the static pressure rise due to the effect of centrifugal force. The current results suggest that the inflow condition into the diffuser may be improved to increase the diffuser performance.

Chapter 7

Effects of Unsteadiness

7.1. Introduction

Flow analysis has been conducted in the last chapter through single passage steady simulation. The general flow features have been discussed. However, it is well known that the flow inside a centrifugal compressor is highly unsteady, steady simulation would not be able to take into account the unsteadiness, thus the results may be not that accurate. Therefore, it is essential to examine to what extent this unsteadiness would affect the centrifugal compressor flow field. This chapter intends to analyse the effect of unsteadiness on the performance and flow field of Dyson V2 centrifugal compressor. The simulation conditions are very similar to those of ERCOFTAC centrifugal compressor as presented in section 5.4, and the unsteady flow field analysis is limited to the impeller design operation condition Case 1.

7.2. Results

It is generally useful to compare the performance prediction results between steady simulation and unsteady simulation, performance is the direct reflection of the flow field, so the difference in performance would imply the existence of different predicted flow behaviours. Figure 7- 1 presents the performance predictions from steady and unsteady simulations, it is found that unsteady simulation tends to predict the performance with higher values. It is known that

only unsteady simulation could resolve the unsteadiness, therefore, it is suspected that unsteadiness is responsible for the difference in performance.
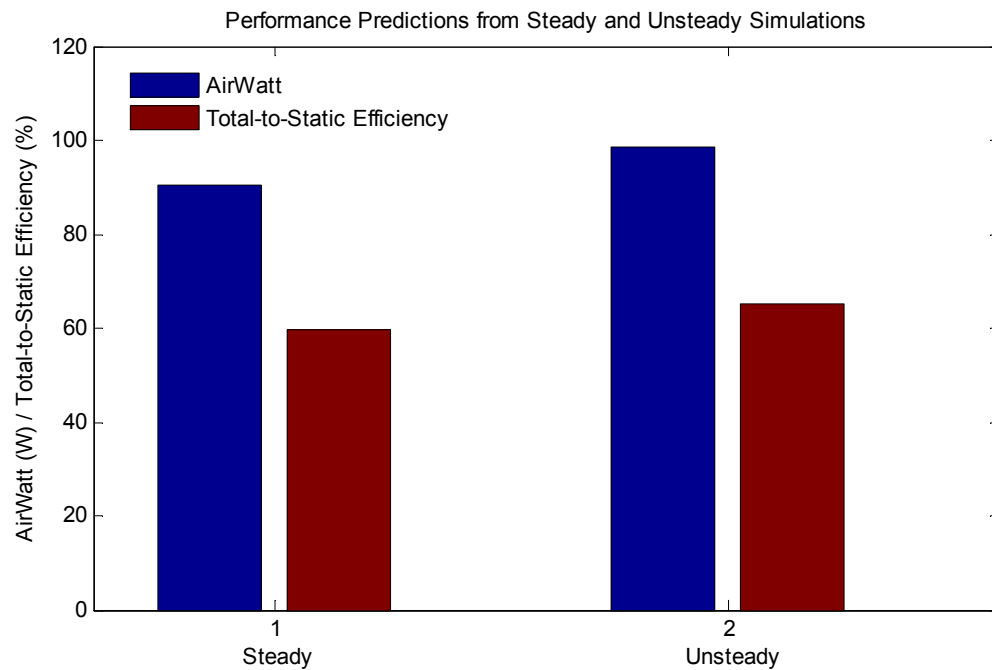

Figure 7- 1: Performance comparison between steady and unsteady simulations.

Figure 7- 2 presents the Mach number contour on stations 1 to 4 for both steady and unsteady simulations, the results from unsteady simulation are averaged in time. On station 1 and station 2, the prediction from both simulations are extremely similar, two low momentum regions are observed, one is located near the suction-side/casing corner and corresponds to the separation bubble at impeller blade suction-side near the leading edge, the other is located at the impeller blade pressure-side and corresponds to the pressure-side separation bubble. However, noticeable differences are found on station 3 and station 4, which are closer to the impeller outlet. A low momentum core region is located very near to the blade pressure-side from steady simulation, while that from unsteady simulation is in between the pressure-side and suction-side, although it is relatively closer to the pressure-side. It is also noted that the steady simulation predicts lower core velocity, it may imply that the unsteadiness affects the vortex decay process, actually, the vortex strength is weakened by unsteadiness, however, it does not

Steady Simulation   **Time-Averaged Unsteady Simulation**

Mach Number in Rotating

0.00000   0.080000   0.16000   0.24000   0.32000   0.40000
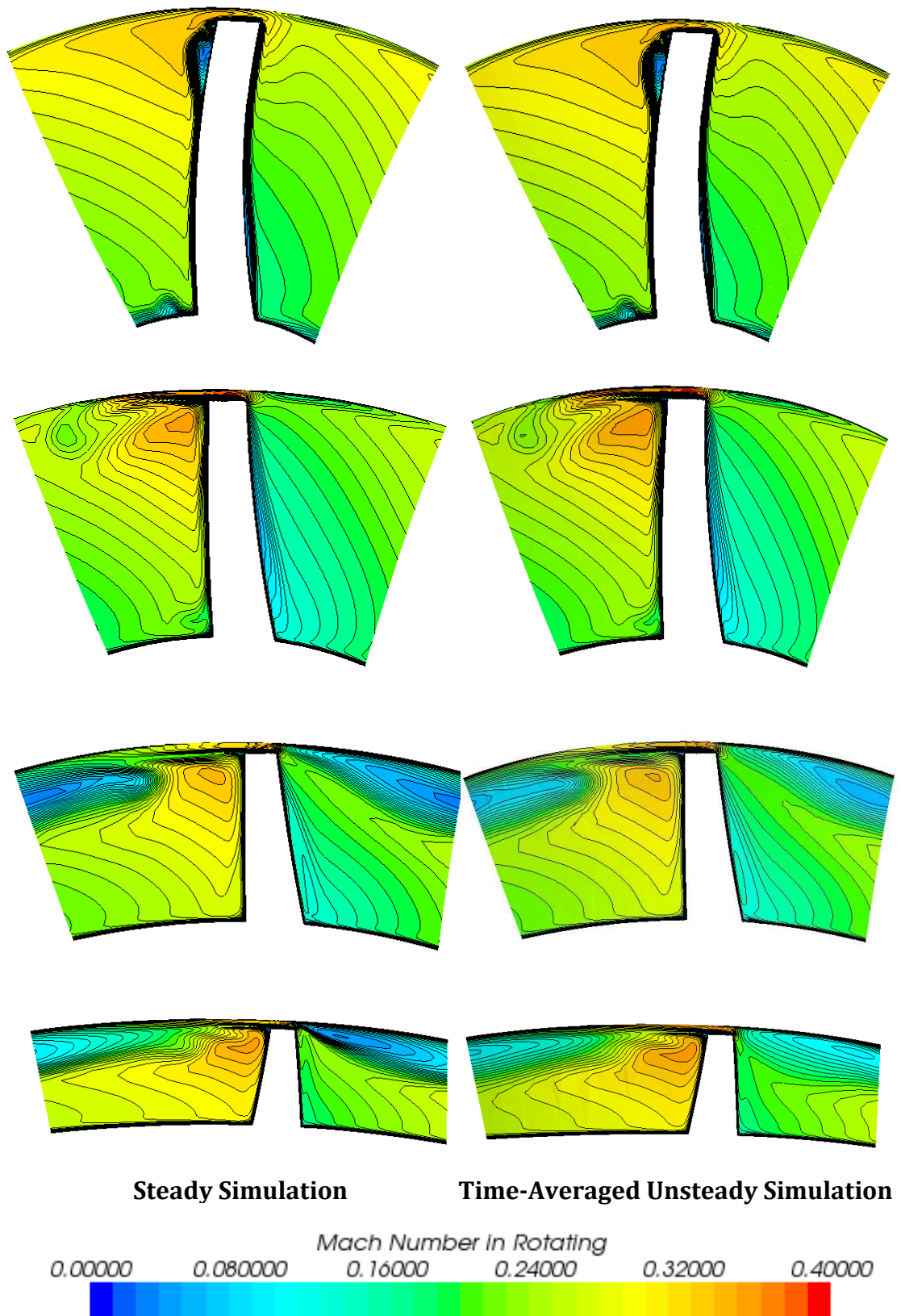
Figure 7- 2: Relative Mach number contour for steady and unsteady simulations on stations 1 to 4 (top to bottom) in impeller region.

Steady Simulation   **Time-Averaged Unsteady Simulation**
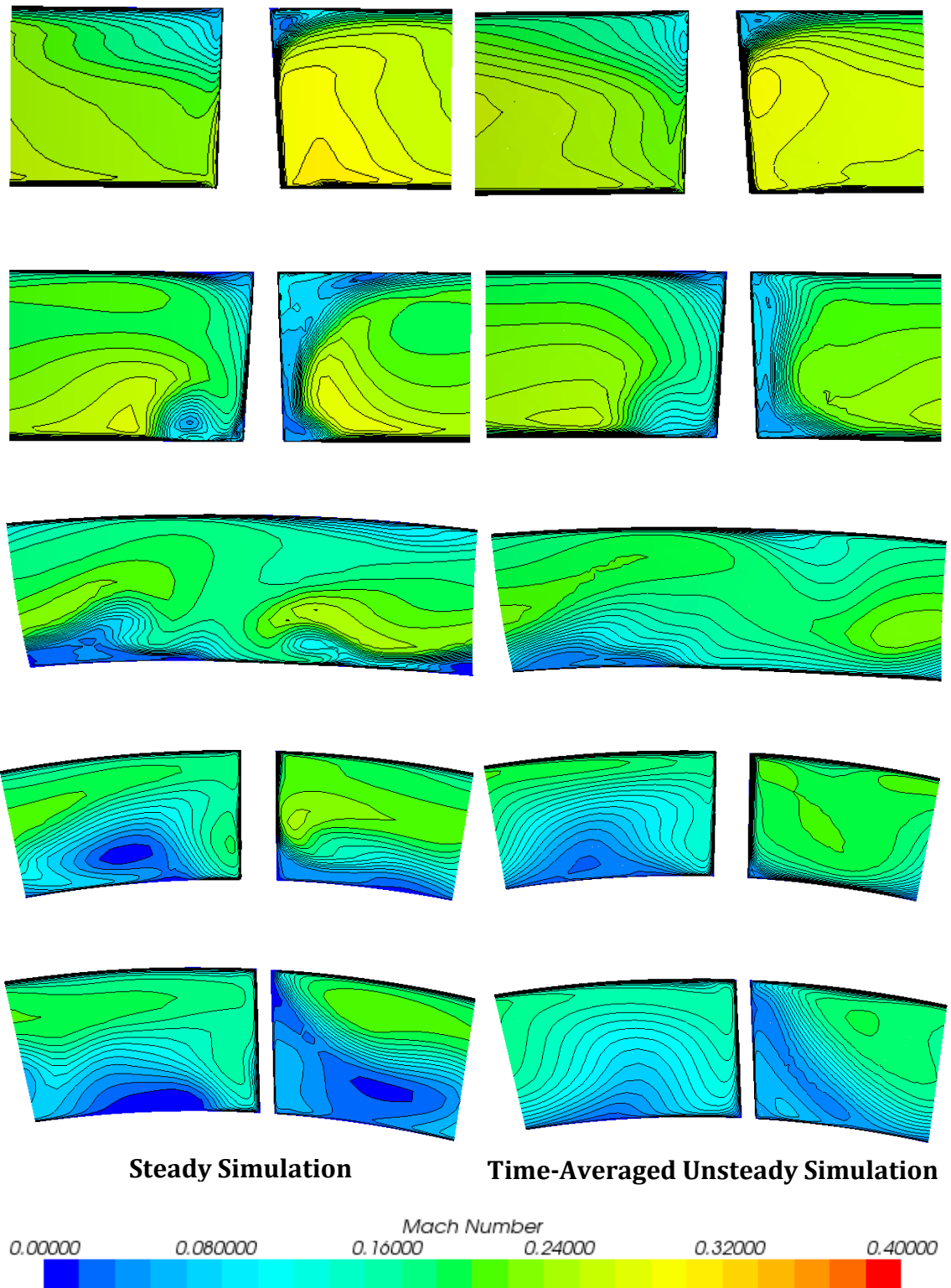
Figure 7- 3: Mach number contour for steady and unsteady simulations on stations 5 to 9 (top to bottom) in diffuser region.

have noticeable effects on the vortex formation process, and the unsteadiness may be primarily resulted from the impeller-diffuser interaction.

The diffuser Mach number contours predicted from both steady and unsteady simulations are compared in Figure 7- 3 on stations 5 to 9, Low momentum regions are observed across all stations. The low momentum regions should correspond to separations as discussed before. Steady simulation predicts relatively large regions of low momentum fluid compared to prediction from unsteady simulation, the difference between them increases towards the diffuser outlet. The difference may imply that unsteadiness could essentially prompt momentum exchange and help weaken or suppress the flow separation, it may be concluded that the blockage is reduced inside the diffuser passage due to the unsteadiness.

Referring to Figure 7- 4, the local entropy generation rate contours are presented on station 4 (impeller) and station 6 (diffuser) for different time instant (non-dimensionalised according to Eqn 5-1), comparison is also made between steady and unsteady simulations. On station 4, steady and unsteady simulations give different predictions on tip leakage flow induced local loss generation. It is obvious that steady simulation over-predicts the local loss generation, unsteadiness seems to weaken the tip leakage flow induced vortex. Similarly, steady simulation over-predicts the local loss generation on station 6, unsteadiness seems to weaken or suppress the flow separation in diffuser. At different time instants, the local loss contour only varies slightly, the effect of unsteadiness is very limited on station 4 and station 6.

As mentioned before, the unsteadiness generated by impeller-diffuser interaction is significant at positions near the impeller outlet. To understand the effects of impeller-diffuser interaction, Relative Mach number contours at different time instants are presented in Figure 7- 5, the black bar indicates the position of radial diffuser leading edge, the black trapezoid represents the position of the impeller blade trailing edge. The impeller blade moves to the right, while the diffuser blade is stationary. Two distinct features are observed, the first one is that the presence

Steady Simulation

Unsteady Simulation

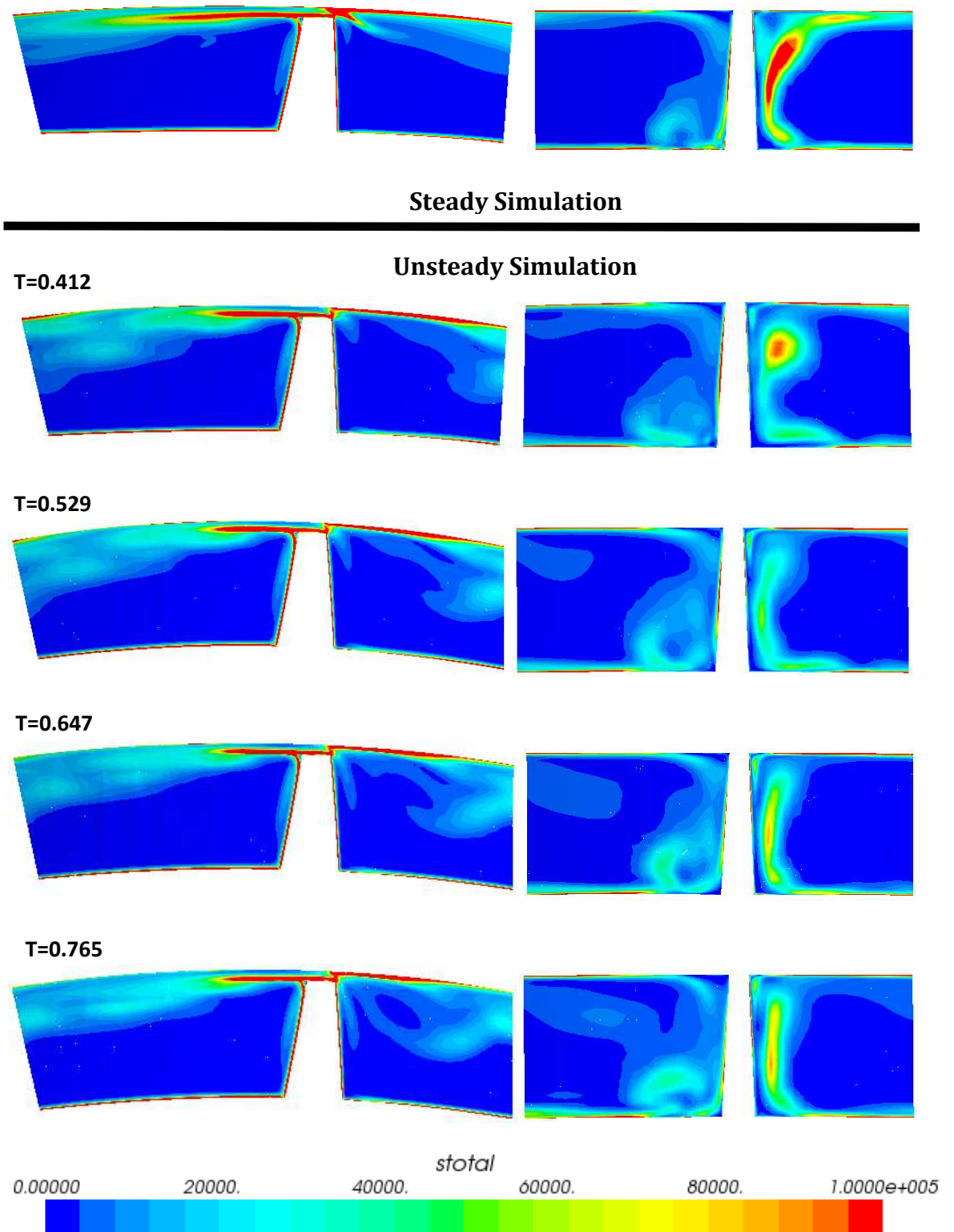**T=0.412**

T=0.529

T=0.647

T=0.765

Figure 7- 4: Local entropy generation rate per unit volume $[W/(m^3K)]$ contour from steady and unsteady simulations on station 4 (left column) and station 6 (right column) for different time instant.

of diffuser blade tends to migrate the high speed flow from impeller blade suction-side to pressure-side, the other is that the high speed flow at impeller blade suction-side is attenuated by the diffuser blade. In fact, both of them are originated from the impeller-diffuser interaction, the presence of the diffuser blade leading edge would induce adverse pressure gradient. When the diffuser blade leading is too close to the impeller blade suction-side, the adverse pressure gradient would tend to block the flow, as a result, part of the high speed flow is slowed down, the
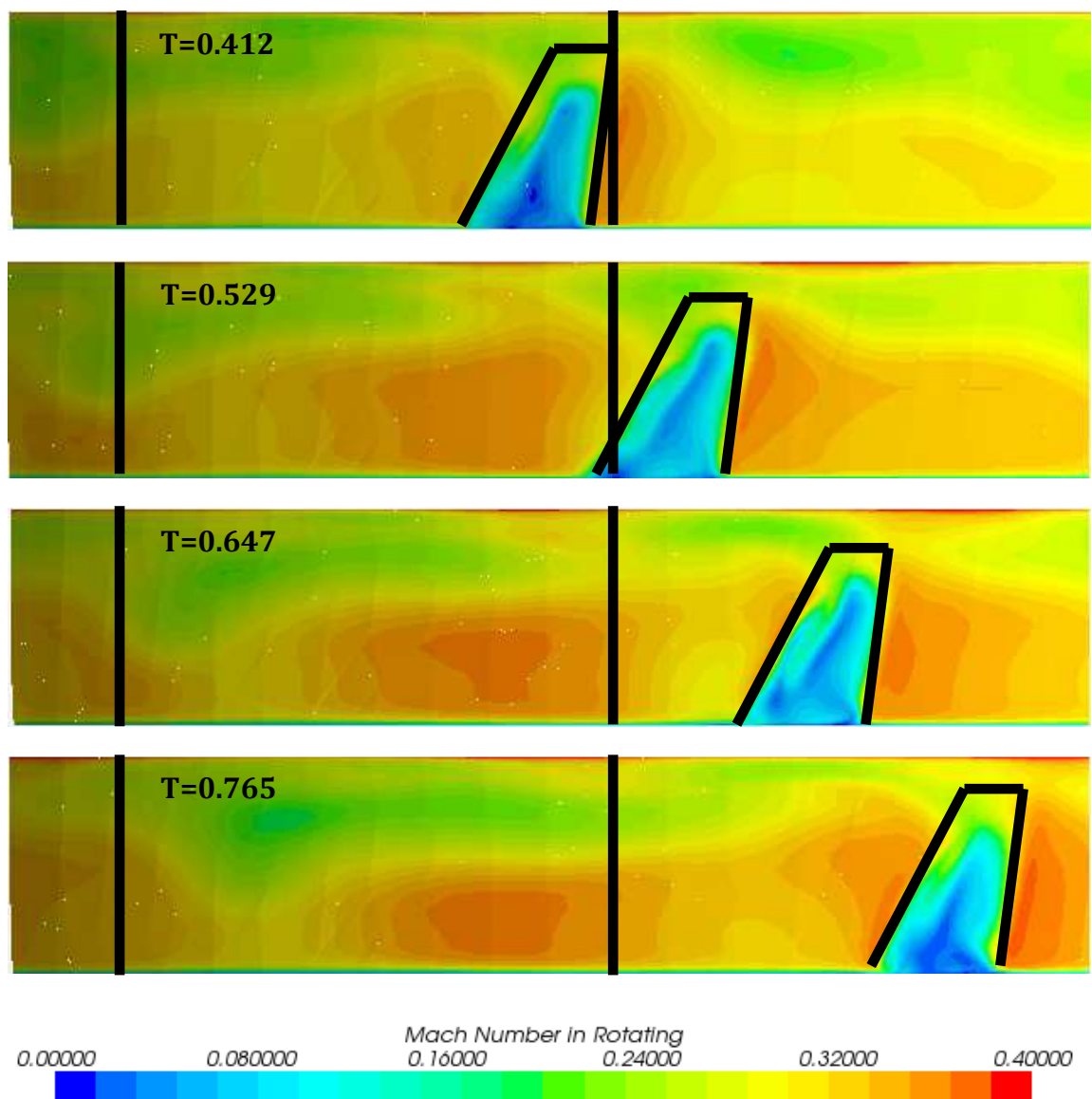

Figure 7- 5: Relative Mach number contour at impeller outlet from unsteady simulation. (The leading edge of radial diffuser blade is marked as black bar, the impeller blade trailing edge is marked as black trapezoid)

Figure 7- 6: Total entropy generation per unit volume [W/(m³K)] contour at impeller outlet from unsteady simulation. (The leading edge of radial diffuser blade is marked as black bar, the impeller blade trailing edge is marked as black trapezoid)
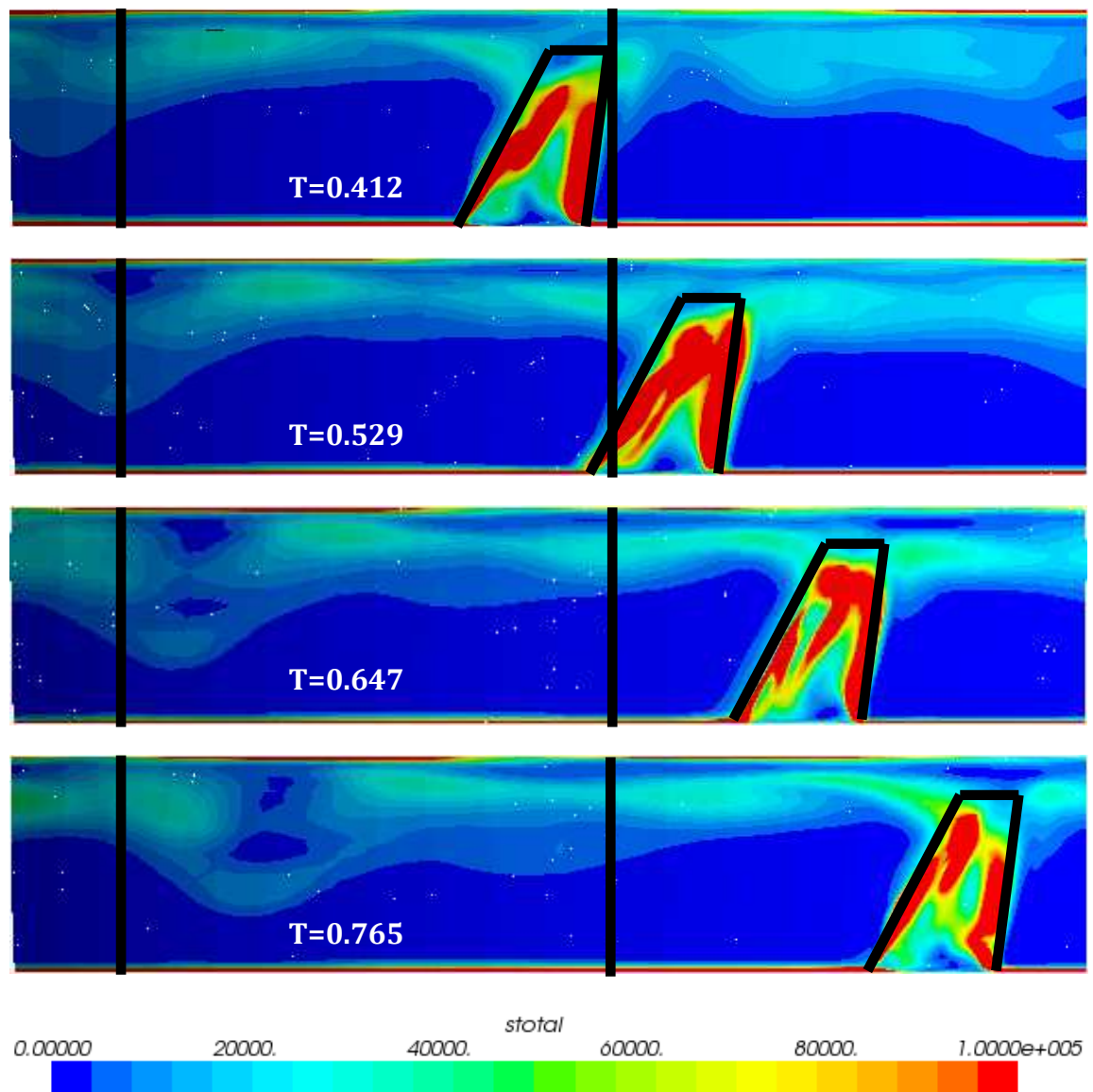
rest is directed away from the suction-side. As discussed previously, the low momentum region here corresponds to the impeller blade wake due to the blunt impeller trailing edge, and it is slightly affected by the impeller-diffuser interaction. It is also noted that the low momentum region near the casing is hardly affected by the impeller-diffuser interaction. Figure 7- 6 shows the total entropy generation rate per unit volume at the impeller outlet, the local loss generation patterns are very similar at different time instants, except in the impeller wake region (wake
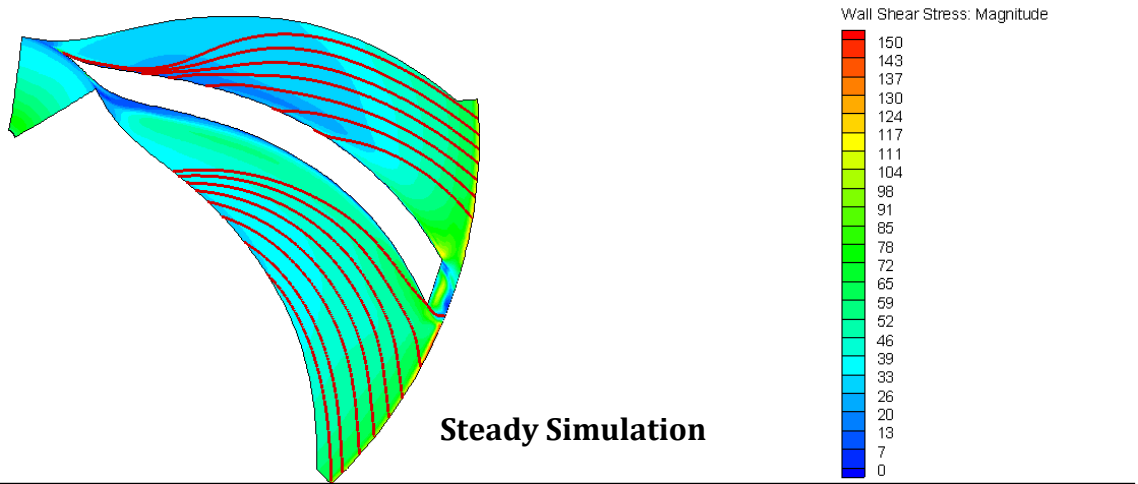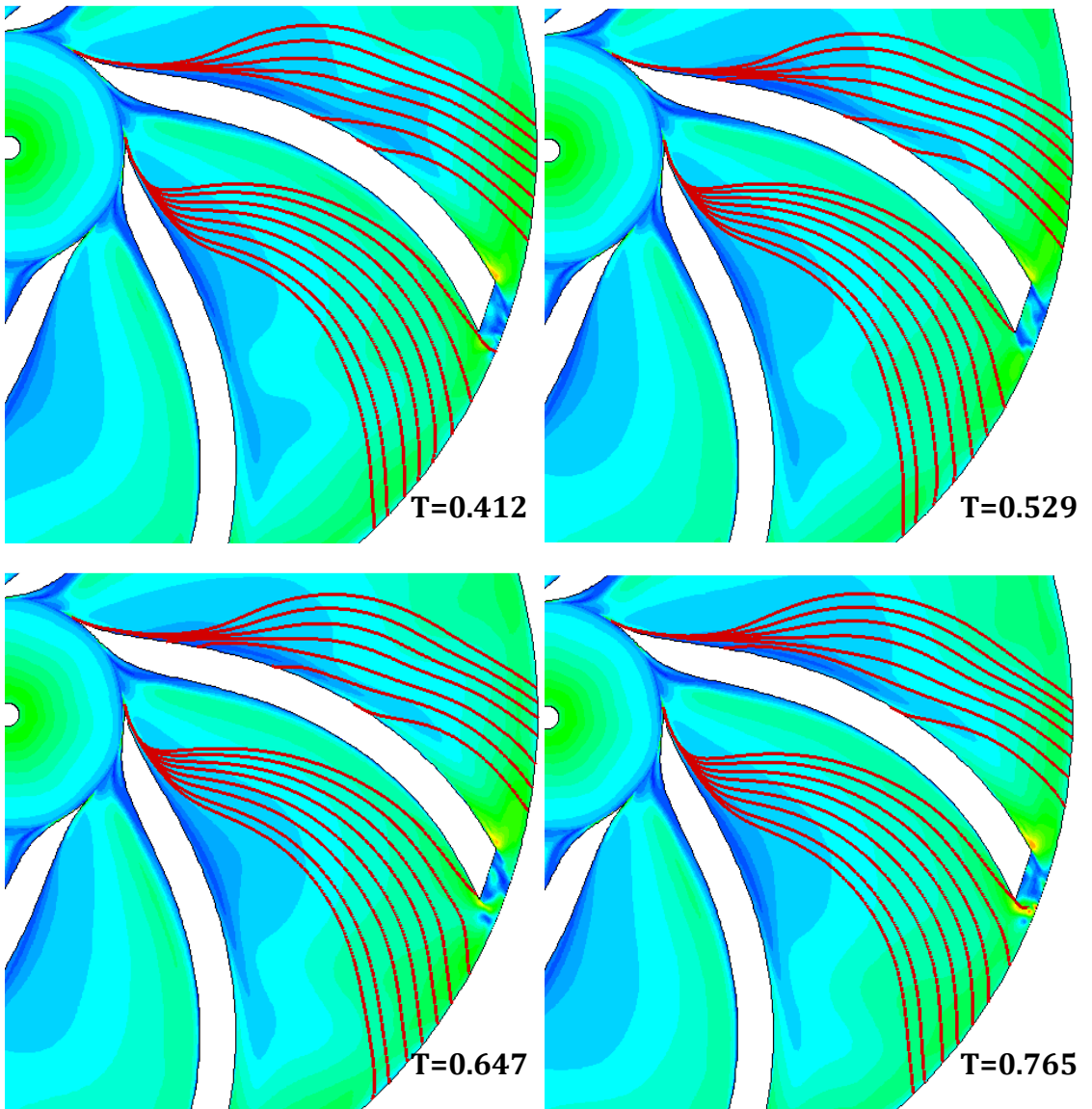
Figure 7- 7: Wall shear stress (Pa) contour with skin friction lines on impeller hub, predicted from steady and unsteady simulations (top view).

loss), it is thus concluded that the impeller-diffuser interaction only slightly affect the loss behaviour inside the impeller.

The wall shear stress contour with skin friction lines is presented in Figure 7- 7 from both steady and unsteady simulations. It is observed that the predicted wall shear stresses and skin friction lines only differ slightly between steady and unsteady simulations, perceivable variations are only found near the blade pressure-side and could be attributed to the presence of a very weak vortex, which may occur at the blade/hub junction due to boundary layer interaction.

7.3. Summary

Some of the important aspects of unsteadiness were discussed in this chapter, unsteadiness was found to help improve performance. The underlying reason is that unsteadiness would help weaken flow separation and associated vortex, as a result, both blockage and local loss generation were reduced considerably. Impeller-diffuser interaction had significant effects on the high speed flow at the impeller blade suction-side, the radial diffuser leading edge migrated high speed flow from impeller blade suction-side to pressure-side and slowed down the high speed flow at impeller blade suction-side. However, it has limited effects on the tip leakage flow induced passage vortex, the local loss generation was hardly affected. The effects of unsteadiness on the hub wall shear stress distribution were examined, both the magnitude and direction are changed slightly due to unsteadiness. To assess whether riblets designed based on steady simulation would perform acceptably in real operation, the effects of unsteadiness have to be investigated.

Chapter 8

Application of Riblets

8.1. Introduction

This chapter presents the application of riblets. First of all, further topics on riblets are discussed, including the riblets operation regimes, yaw-angle effect, optimization of riblets and etc, only sawtooth riblets are considered due to the availability of experimental data, an explicit expression is obtained to relate the wall shear stress reduction to the riblets non-dimensional spacing. Then riblets are proposed to be applied to the hub of Dyson V2 centrifugal compressor to help reduce the hub endwall loss, steady simulation results have been used to design the riblets. At the end, the effects of unsteadiness on riblets performance are discussed to check whether the designed riblets could achieve acceptable performance in real operation, for which the flow is essentially unsteady. And it should be noted that this preliminary work is limited to the impeller design operation condition Case 1.

8.2. Further Discussions on Riblets

Riblets surface is extensively studied in literature, and it is generally referred to as a kind of passive flow control method, which can manipulate the flow intentionally. Riblets can be applied in two ways, either delaying the laminar-turbulent transition, or reducing the skin friction drag in turbulent flow. Because the laminar-turbulent transition itself is still an open question, and flow is almost all turbulent in nature, most of the works on riblets have been focused on the turbulent skin friction drag

reduction. Here, attention has been paid to the turbulent skin friction drag reduction with riblets.

Generally, wall shear stress reduction is used to assess the effectiveness of riblets, wall shear stress reduction can be plotted against non-dimension spacing s^+ to obtain the riblets performance curve. In literature, it is found that the riblets performance curve can be split into segments corresponding to different features, as shown in Figure 8- 1, according to Bechert et al. (1997a), if s^+ is small enough, the viscous interaction is expected to be linear, as a result, the wall shear stress reduction is nearly linearly proportional to s^+, however, when s^+ increases, the interaction becomes nonlinear, if s^+ is large enough, the riblets will behave like a rough surface. In practice, the 'viscous regime' is likely to be valid for $s^+ < 10{\sim}15$ (Garcia-Mayoral and Jimenez, 2011), in the current work, a value of 10 is used to separate the linear 'viscous regime' and the nonlinear interaction counterpart. The expressions for wall shear stress reduction and s^+ are given as Eqn 8-1.

$$\begin{cases} \frac{\Delta\tau}{\tau}(\%) = As^+ & \text{If } s^+ \leq 10 \\ \frac{\Delta\tau}{\tau}(\%) = f(s^+) & \text{If } s^+ > 10 \end{cases} \qquad \text{Eqn 8- 1}$$

Where A is a constant and represents the slope, $f(\blacksquare)$ is a nonlinear function and obtained using nonlinear curve fitting.
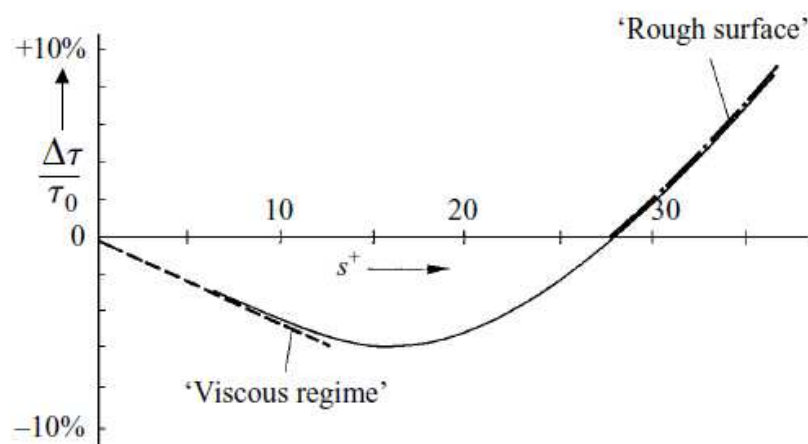

Figure 8- 1: General structure of a wall shear stress reduction curve with riblets (Bechert et al., 1997a).

As mentioned previously, sawtooth riblets will be employed due to the availability of experimental data in literature. The specific sawtooth riblets configuration used in this work is shown in Figure 8- 2, the corresponding experimental data are obtained from Walsh and Lindemann (1984) and plotted in Figure 8- 3. Only one geometric parameter is required to define the riblets size, spacing is used in this work. Curve fitting is employed to obtain the explicit expression between the wall shear stress reduction and non-dimensional spacing s^+, as given in Eqn 8-2 below. The fitted curve is plotted in Figure 8- 3, it is noted that the quality of the curve fitting is good.

$$\begin{cases} A & = -3.7778E - 1 \\ f(s^+) = (3.8959E - 6)(s^+)^4 - (5.9223E - 4)(s^+)^3 \\ \quad\quad -(6.7087E - 1)(s^+) + (1.6160E - 2) \end{cases} \quad \text{Eqn 8- 2}$$
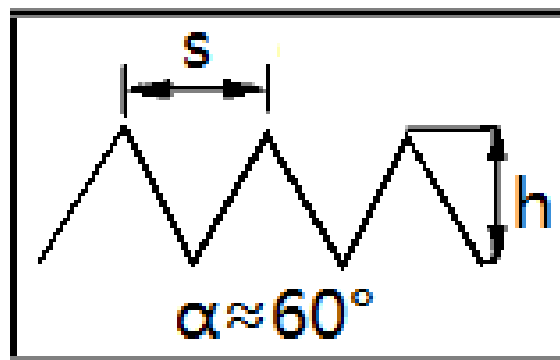

Figure 8- 2: Sawtooth riblets dimensions.

Curve fitting has been conducted to obtain the relationship between wall shear stress reduction and riblets non-dimensional spacing, the next step is to obtain the wall shear stress such that the riblets spacing can be calculated using Eqn 2-19. It is generally difficult to obtain the wall shear stress. Anderson, Macgillivray and Demont (1997) proposed to estimate the wall shear stress from the simple case of turbulent flow over a flat plate, it is of general practice to apply momentum integral equation to a 1/7 power velocity profile, and obtain:
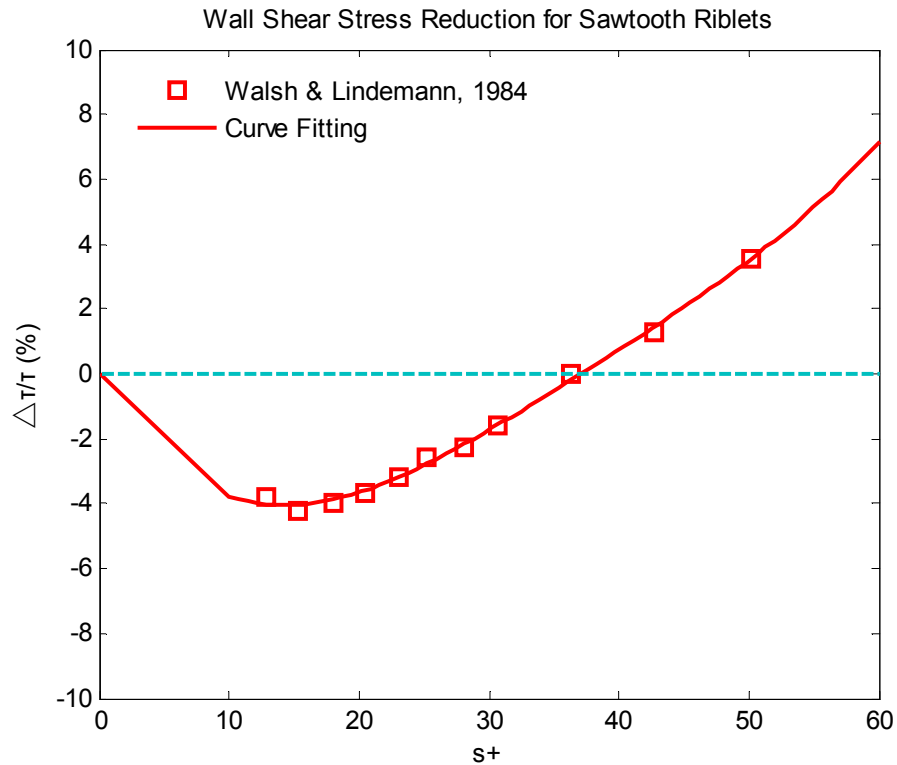
Figure 8- 3: Wall shear stress reduction for sawtooth riblets obtained from Walsh and Lindemann (1984) with curve fitting.

$$\tau_w = \frac{1}{2}\rho U^2 \frac{0.0594}{Re_x^{1/5}} \qquad\qquad \text{Eqn 8- 3}$$

Where $Re_x = \frac{Ux}{\nu}$, x is the distance measured from the leading edge, U is the flow velocity over the surface.

However, in the case of compressor, due to the complex geometry and flow behaviour involved, Eqn 8-3 is unlikely to give acceptable prediction on wall shear stress. Therefore, wall shear stress is obtained from numerical simulation in this work.

As already discussed in 2.4.1, riblets is subject to performance deterioration under yaw-angle effect, and the flow in practical application is seldom aligned with one fixed direction, instead, the flow direction varies. As a result, yaw-angle effect is needed to be considered carefully to ensure that the riblets performance is not severe impacted. In literature, only a few experimental data on yaw-angle effect are available. Those of Walsh and Lindemann (1984) are plotted in Figure 8- 4, wall

shear stress reduction data are available for three different yaw angles, 0 deg, 15 deg and 30 deg respectively, curve fitting is performed for each set of data, the corresponding fitted curve is plotted as well, a summary of the nonlinear curve fitting is given in Table 8- 1, polynomials of different orders are applied to obtain the most appropriate curve fitting. Although the explicit expressions for three yaw angles are available, the intermediate values cannot be obtained directly. A nonlinear interpolation (quadratic) is applied to relate the wall shear stress reduction to the yaw-angle at constant non-dimensional spacing. As a result, the
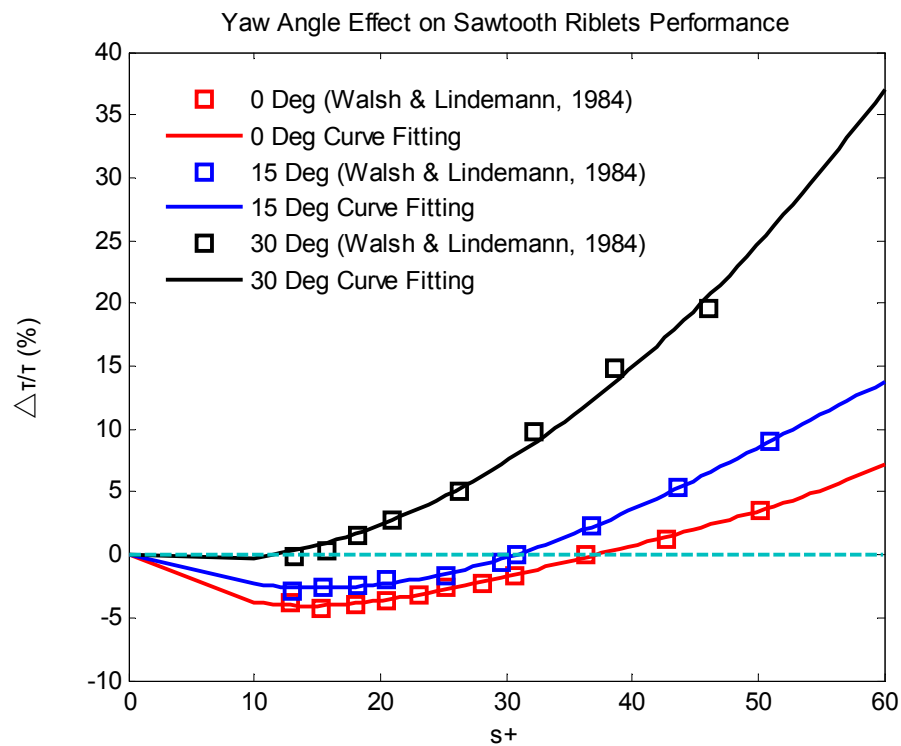

Figure 8- 4: Yaw-angle effect on riblets performance with data cited from Walsh and Lindemann (1984).

wall shear stress reduction can be expressed in terms of non-dimensional spacing and yaw-angle, and given as:

$$\frac{\Delta\tau}{\tau}\ (\%) = f_1(s^+)\psi^2 + f_2(s^+)\psi + f_3(s^+) \qquad \text{Eqn 8- 4}$$

Where f_1, f_2 and f_3 are functions of non-dimensional spacing and depend on whether the riblets operate in the linear regime or nonlinear regime.

Riblets Config.	Yaw Angle (deg)	Order	Expression
Sawtooth	0	Quartic	$A_1(s^+)^4 + B_1(s^+)^3 + C_1(s^+)^2 + D_1 s^+ + E_{S1}$
	15	Quartic	$A_{S2}(s^+)^4 + B_{S2}(s^+)^3 + C_{S2}(s^+)^2 + D_{S2} s^+ + E_{S2}$
	30	Quadratic	$A_{S3}(s^+)^2 + B_{S3} s^+ + C_{S3}$

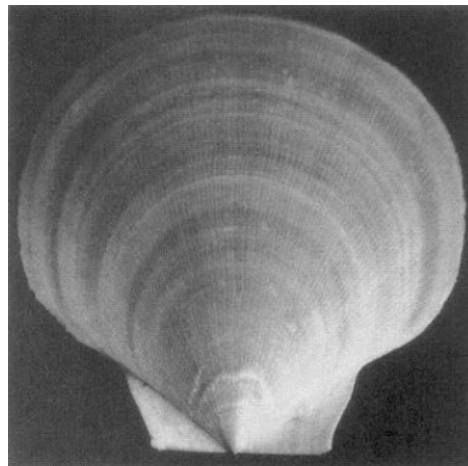Table 8- 1: A summary of the curve fitting for sawtooth riblets.

Figure 8- 5: Top view of the scallop shell. (Anderson, Macgillivray and Demont, 1997)
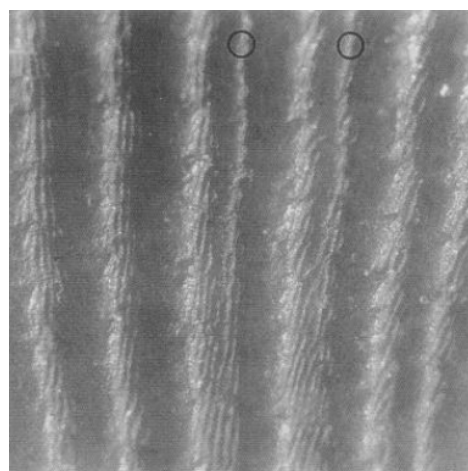

Figure 8- 6: Magnified view of scallop shell. (Anderson, Macgillivray and Demont, 1997)

In practical application, the surface to apply riblets may be convergent or divergent. For instance, the impeller hub is actually divergent, the length in circumferential direction increases towards the impeller outlet. If constant number of riblets are applied, the riblets spacing will inevitably increase towards the divergent direction, as a result, the riblets performance may be impacted. In nature, there are ways to resolving this problem. Anderson, Macgillivray and Demont (1997) found that scallop shells are covered with riblets to help reduce the turbulent skin friction drag, as shown in Figure 8- 5, they estimated the wall shear stress with Eqn 8-3, and concluded that riblets spacing should be smaller at the leading edge and increases in the downstream direction. However, referring to Figure 8- 5, the situation for scallop shells seem to be completely different. A magnified view reveals the magic feature, as shown in Figure 8- 6, the black circles indicate the newly added riblets. This feature is called intercalation, the newly added riblets effectively reduce the riblets spacing towards the leading edge and maintain the effectiveness of riblets at certain high level.

In literature, most of the experimental data on riblets are obtained with regard to the average wall shear stress for the whole testing plate or tube and measured with shear stress balance. The local wall shear is seldom measured due to the difficulty in taking measurements locally, in this case, only indirect method can be applied, for instance, Bechert et al. (1997a) applied Preston tube, which actually makes use of a Pitot tube, to measure the wall shear stress distribution, Figure 8- 7 presents the wall shear stress distribution on test plate (with riblets) and reference plate (smooth) at two different Reynolds numbers as measured by Bechert et al., the wall shear stress distributions for both plates are not uniform, compared to the reference plate, the wall shear stress distribution for test plate shifts horizontally to the left, indicating the existence of wall shear stress reduction, and it is found that the wall shear stress reduction is nearly constant across the plate at both Reynolds numbers, except at the upper corner of the test plate, this may be caused by the presence of pressure gradient control. The experimental data used in this work are the average wall shear stress as measured by Walsh and Lindemann (1984) in a wind tunnel, in this preliminary study, it is assumed that the local wall shear stress reduction distribution and local wall shear stress distribution are uniform for their

experiment, and thus the measured averaged wall shear stress reduction can be treated as local quantity and corresponds to local wall shear stress in the following studies.
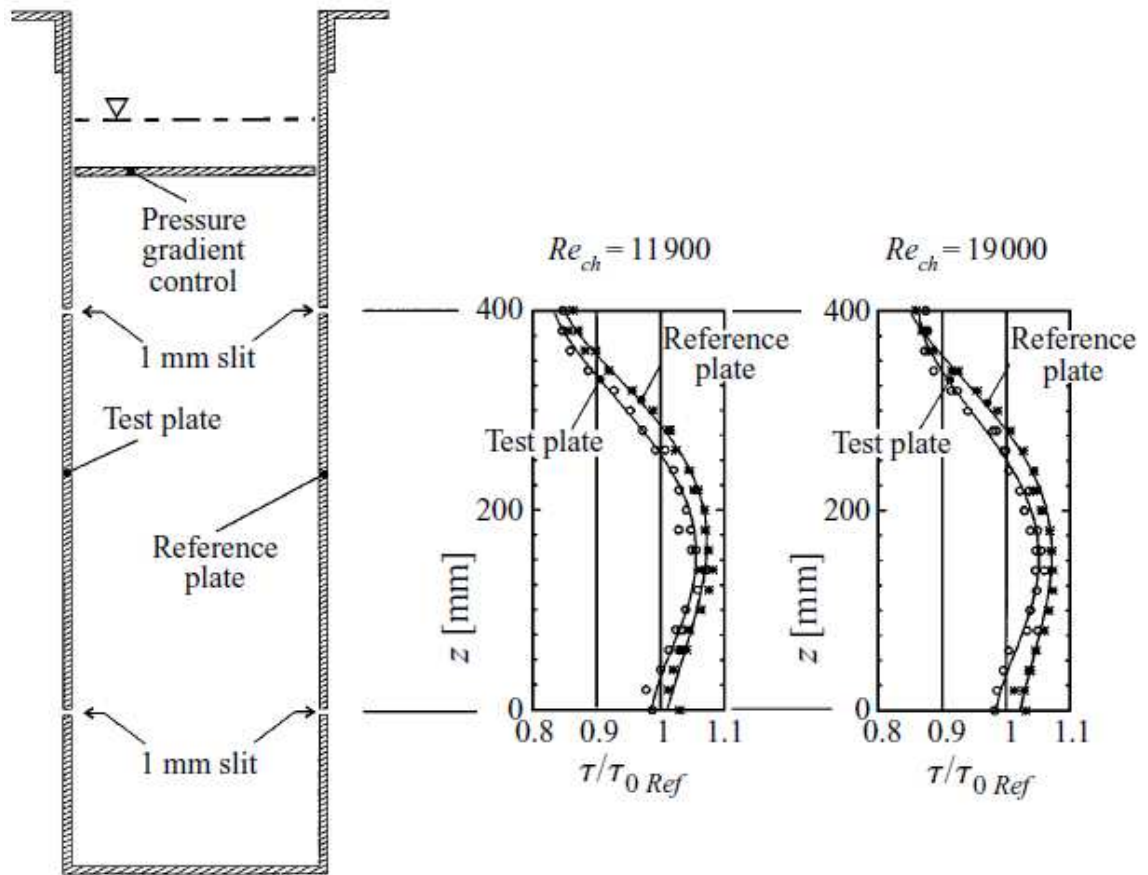

Figure 8- 7: Wall shear stress distribution on test plate. (Bechert et al., 1997)

8.3. Riblets on Dyson V2 Impeller

Tremendous amount of efforts have been devoted to improving the centrifugal compressor performance, improvements have been achieved, however, most of them are on operation range and operation stability, the reduction in loss generation is seldom achieved, possibly due to the complex flow behaviour involved. Dyson V2 centrifugal compressor is of small size, as a result, the flow behaviour is even more complicated. As discussed previously, the tip leakage flow in Dyson V2 impeller is the primary source of loss generation, the flow separates from the blade tip at the pressure-side and generally leaks to the suction-side without reattachment due to the nature of the very thin blade tip, it is thus difficult

to control the tip leakage flow. Despite tip structures may help reduce the amount of tip leakage flow slightly, the additional loss due to friction of these structures usually overweighs the benefits. Endwall loss and blade surface loss are another two sources of losses and affected by the skin friction drag, which is usually characterized with the wall shear stress. In other words, the loss generation will be less if the wall shear stress is reduced. Referring to Figure 6- 11, the hub endwall loss near the impeller outlet is significant, the reduction in wall shear stress here would result in significantly less loss generation. Riblets surface is proposed to attack the problem in this work, due to the extremely high computational cost involved in computing the flow field around riblets, curve fitting approach is employed as introduced previously.

It is known that riblets should be designed properly, otherwise, they may work the other way around and give rise to increase in wall shear stress. The flow field prediction from steady simulation will be used to design the riblets. As mentioned before, sawtooth riblets are employed here, so only three design aspects have to be considered, i.e. riblets location, riblets orientation and riblets size. The application of riblets should not prompt flow separation, so riblets should be applied to the region where skin friction lines are directed towards and ended at the impeller outlet. Referring to Figure 6- 12, it is noted that there is a region on the hub where skin friction lines are properly directed, the flow in this region is expected to be turbulent and free from separation. So it is determined that riblets will be applied to this region on hub, as shown in Figure 8- 8 and marked with the circular band, and the riblets are aligned with the skin friction lines such that the yaw-angle effect is avoided in the context of steady simulation, however, due to the effect of unsteadiness, yaw-angle effect cannot be avoided in the real operation, it will be discussed in section 8.4. As shown in Figure 8- 2, the ratio of riblets height to spacing is already known, so only riblets spacing has to be determined such that the largest wall shear stress reduction can be achieved, in fact, it is an optimization process. First of all, the wall shear stress distribution is extracted at discrete circumferential stations, as shown in Figure 8- 9, here, only 15 stations are selected, the stations are named from the pressure-side (station 1) to the suction-side
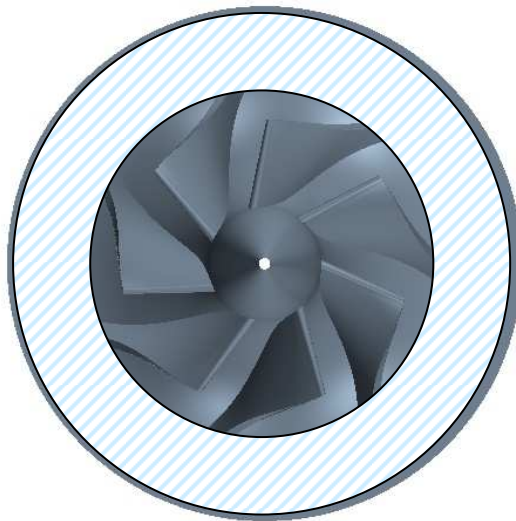
Figure 8- 8: Top view of Dyson V2 impeller with the application of riblets.
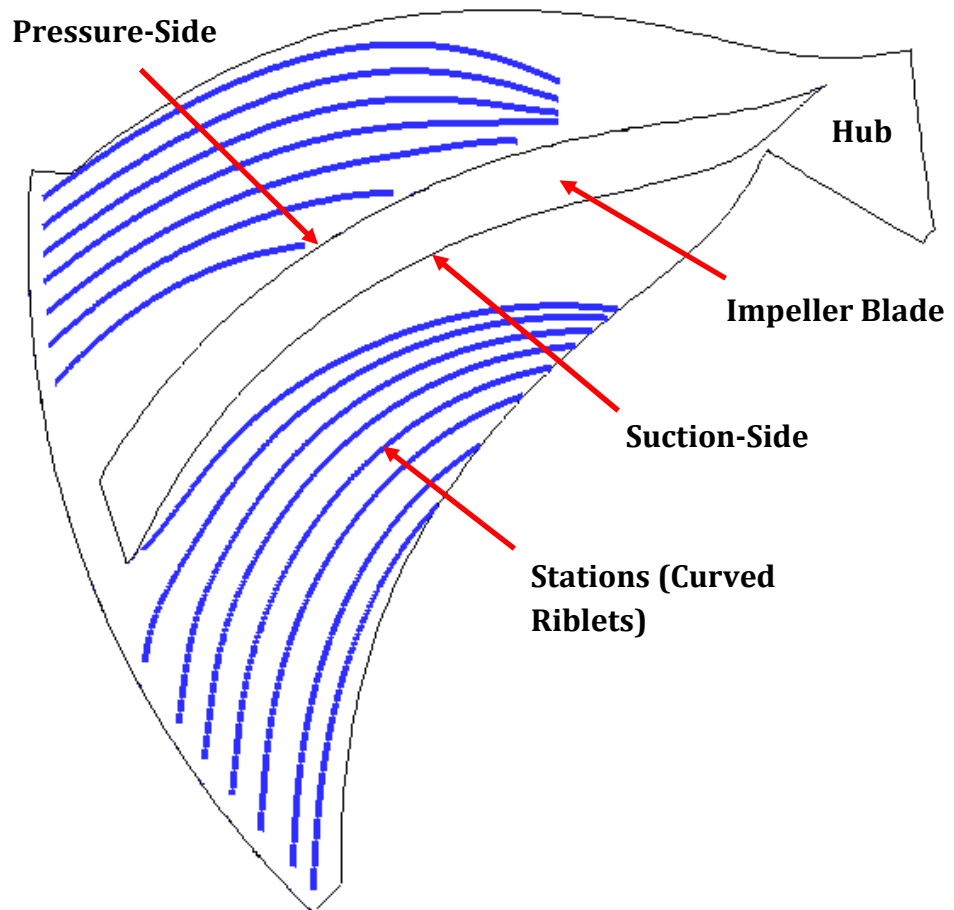

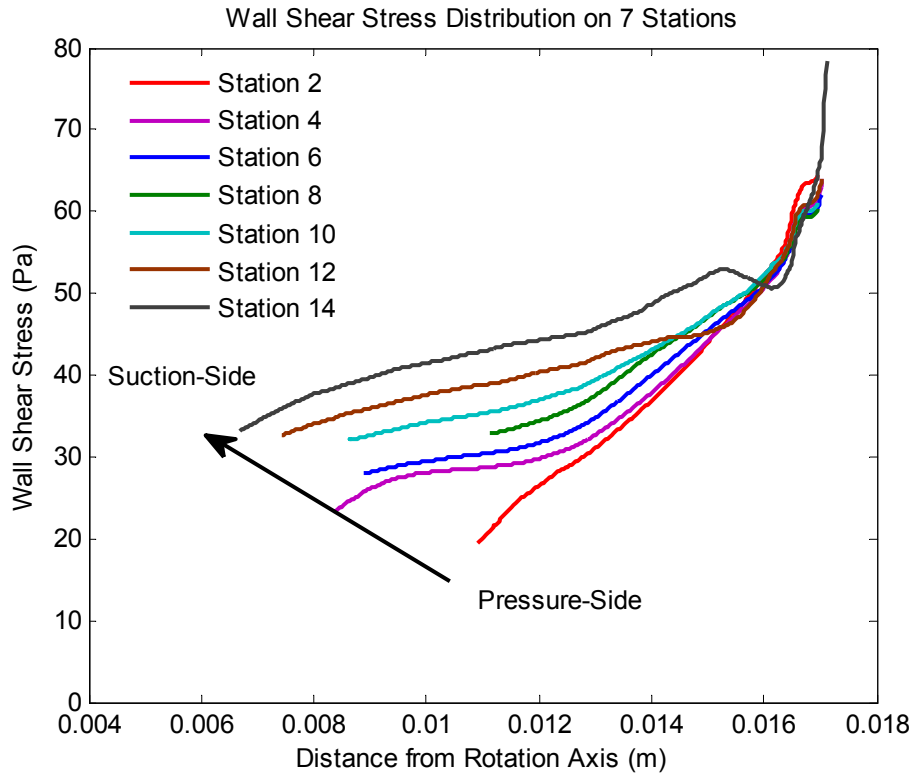Figure 8- 9: Circumferential stations on hub to apply riblets.

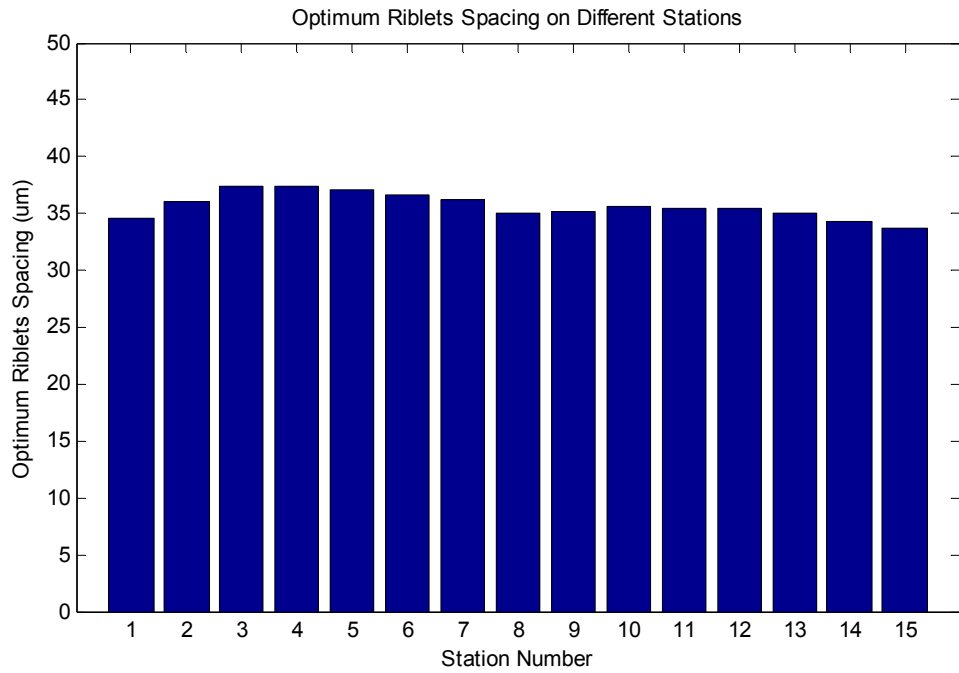Figure 8- 10: Wall shear stress distribution on 7 stations.

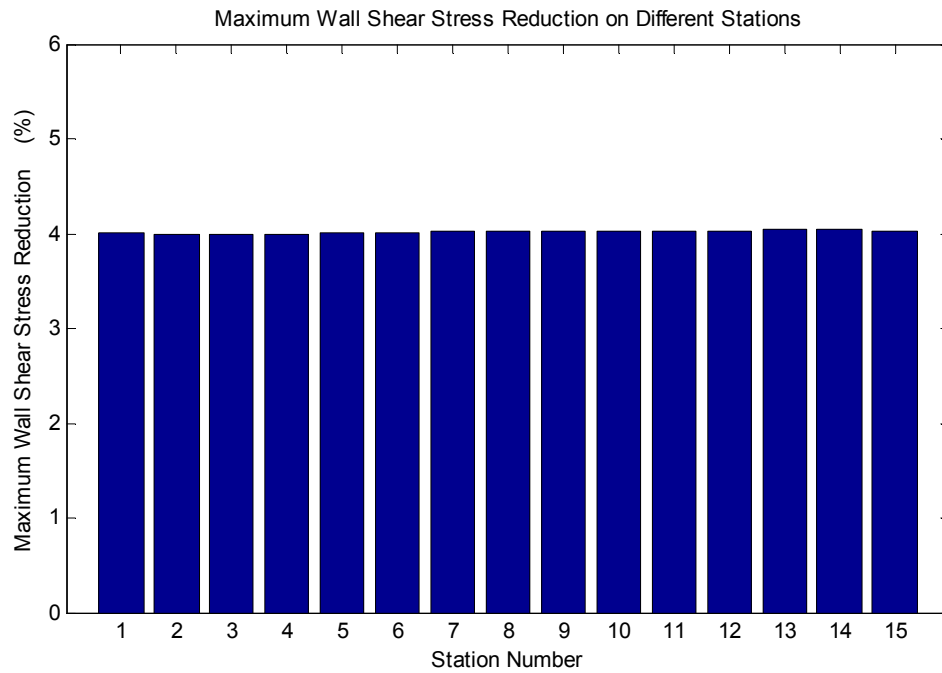Figure 8- 11: Optimum riblets spacing on different stations.

Figure 8- 12: Maximum wall shear stress reduction on different stations.

(station 15). Optimization is conducted on each station with enumeration method. In the future, more stations can be selected to represent the hub endwall more accurately. The wall shear stress distributions for 7 stations are plotted in Figure 8-10. The general trend for wall shear stress is observed that it increases from pressure-side to suction-side due to the higher velocity at the suction side.

The riblets size has been optimized on each station, the optimum riblets spacing is given in Figure 8- 11 for each station, it is found that the optimum spacings are all around 35µm. The corresponding maximum wall shear stress reduction on each station is plotted in Figure 8- 12, almost 4% wall shear stress reduction can be achieved across all stations. In total, the spacing for the designed riblets is around 35µm, a wall shear stress reduction about 4% could be achieved. Because the explicit relation between the wall shear stress reduction and the endwall loss is unknown, the exact percentage of endwall loss reduction cannot be determined, however, it is known that endwall loss would be reduced if wall shear stress is reduced (Eqn 2-10).

8.4. Effects of Unsteadiness

The effects of unsteadiness on flow field have been investigated in chapter 7, it was found that both the wall shear stress magnitude and direction are affected by the unsteadiness. As mentioned previously, in this work, riblets are designed based on steady simulation results, because steady simulation is of lower computational cost and feasible during the engineering design process. In real application, the flow is highly unsteady, therefore, the effects of unsteadiness have to be examined to determine whether riblets designed based on steady simulation could perform acceptably. The effects of unsteadiness should be considered in two aspects, variation in wall shear stress magnitude and yaw-angle respectively. The wall shear stress distribution and direction are extracted on 15 stations at 4 time instants. The wall shear stress distribution and yaw-angle distribution on station 7 are shown in Figure 8- 13 and Figure 8- 14, respectively. Variations are found in both wall shear stress magnitude and yaw-angle magnitude at different time instants. Figure 8- 15 presents the wall shear stress reduction under the effects of unsteadiness, almost 4% wall shear stress reduction can be achieved across all stations, it is thus concluded that the riblets designed based on steady simulation could perform very well under the effects of unsteadiness.
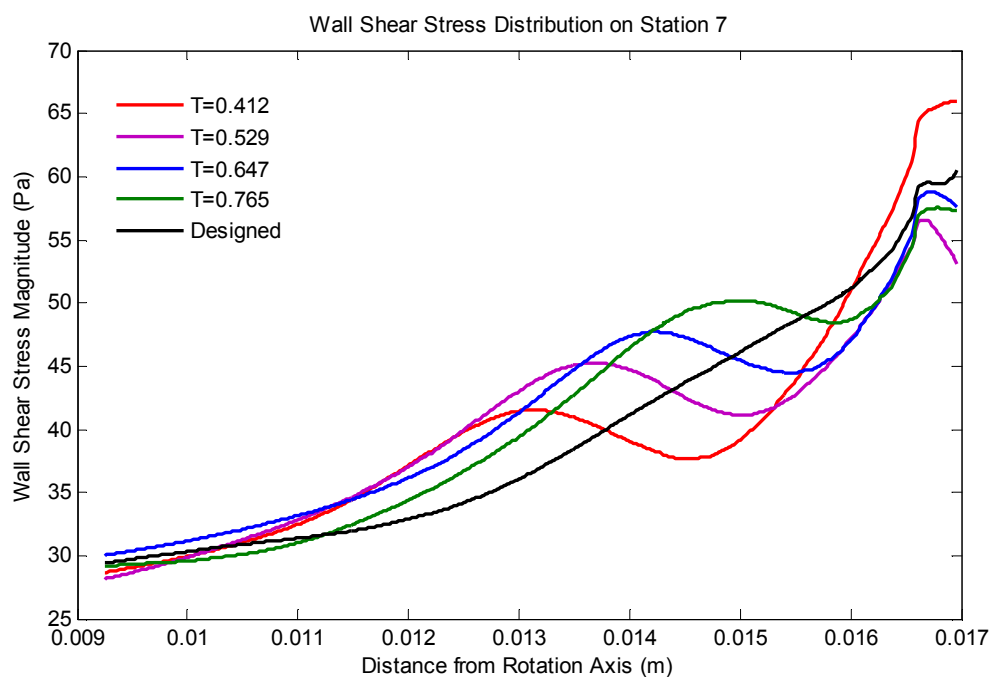

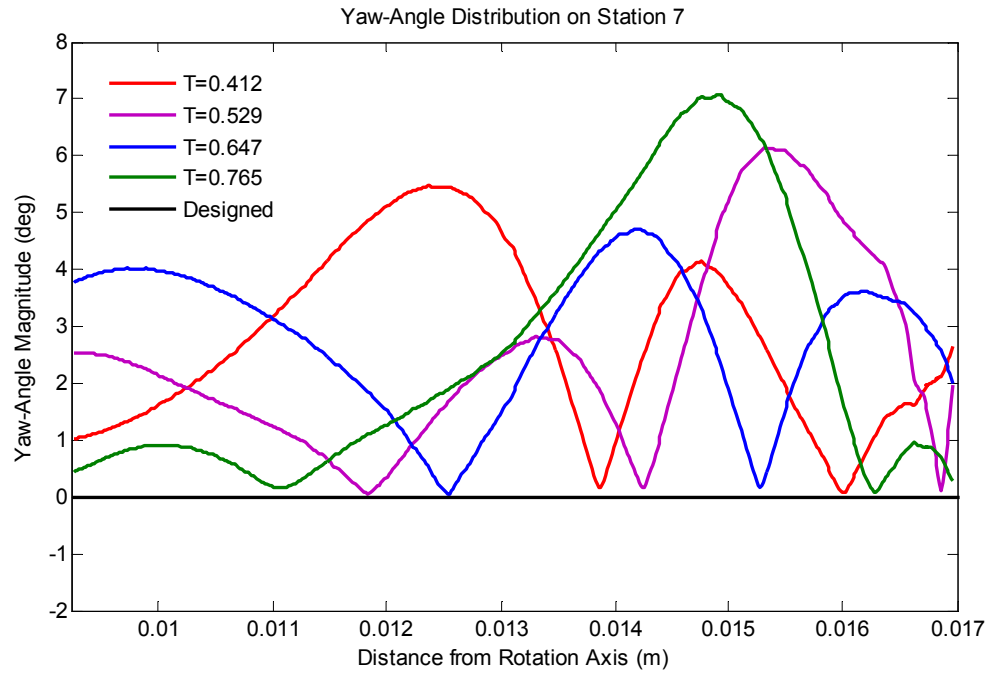Figure 8- 13: Wall shear stress distribution on station 7.
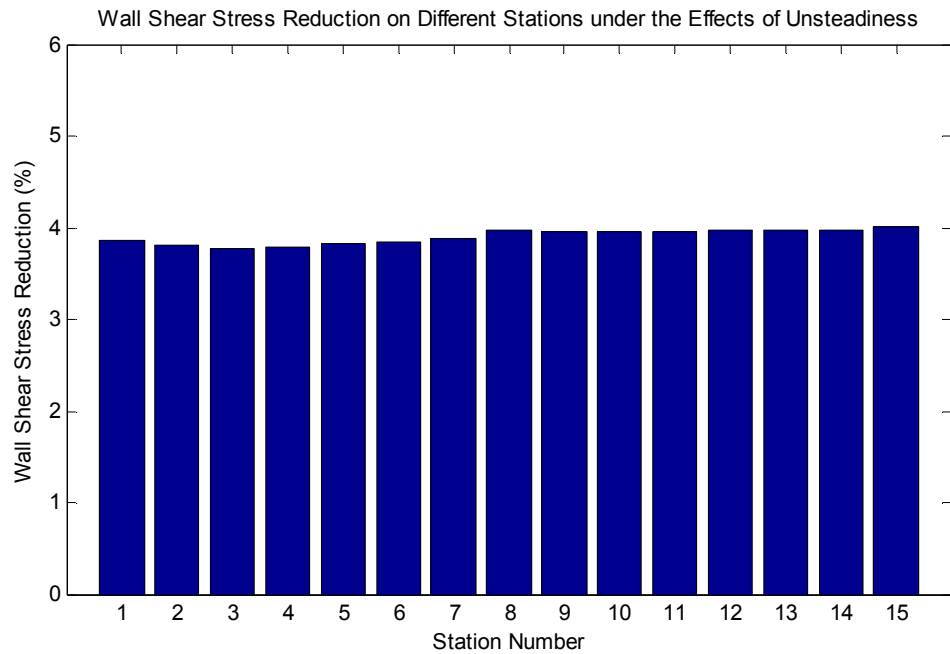
Figure 8- 14: Yaw-angle distribution on station 7.

Figure 8- 15: Wall shear stress reduction on different stations under the effects of unsteadiness.

8.5. Summary

In this chapter, further discussions on riblets have been made, an explicit expression has been obtained for sawtooth riblets through curving fitting on available experimental data in literature, yaw-angle effect has also been taken into account. Then riblets was proposed to be applied to help reduce the impeller endwall loss for Dyson V2 centrifugal compressor. With the explicit expression and the wall shear stress predicted from steady simulation, the riblets have been designed, the spacing is around 35µm, a wall shear stress reduction about 4% could be achieved. Later, the performance of the designed riblets was assessed using unsteady simulation, thus the effects of unsteadiness could be considered. It was confirmed that the designed riblets could perform very well, even under the effects of unsteadiness (similar to real operation), a wall shear stress reduction around 4% could be achieved. However, it should be noted that the current design is not optimized for operation conditions other than Case 1.

Chapter 9

Conclusions and Future Work

9.1. Conclusions

This work is part of the project support by Dyson Ltd., aims at improving the aerodynamic performance of Dyson V2 centrifugal compressors, and serves as the preliminary study on understanding the flow behaviour involved and proposing possible methods for future improvements.

Single passage steady simulation was conducted to predict the performance and flow field of Dyson V2 centrifugal compressor. Different flow features were observed, including tip leakage flow, separation bubble, the so called "jet-wake structure" and corner separation. The vortex roll-up process was identified, the passage vortex was initialized near the impeller leading edge due to tip leakage flow, and grew in the axial part of the impeller, finally, it decayed towards the impeller outlet under the effects of centrifugal force. A loss localization method was employed to identify regions of high local loss generation, it was found that tip leakage flow is the most significant source of loss generation, losses were generated both directly (cross-flow interface at suction-side) and indirectly (passage vortex). Endwall loss and blade surface loss were also significant, however, they were limited to high speed flow regions, such as hub endwall near impeller outlet and blade suction-side. The last significant source of loss generation is the corner separation, commonly occurred in diffuser. Due to the presence of "jet-wake structure" and 90 deg bend, both the radial diffuser and axial diffuser

inflow conditions were severely impacted, as a result, the diffuser stage was not that effective in terms of pressure rise, almost 80% of the pressure rise occurred in impeller due to strong centrifugal force. The effects of unsteadiness were also examined using full annulus unsteady simulation, it was concluded that unsteadiness could help reduce blockage and loss generation, and thus leads to performance improvement.

Riblets were proposed to help reduce the impeller hub endwall loss. Although the explicit relation between wall shear stress reduction and endwall loss is unknown, it is sure that endwall loss will be reduced if wall shear stress is lowered. The design was done based on flow field predicted from steady simulation, a wall shear stress reduction about 4% could be achieved, with the optimum spacing around 35μm. Later, the effectiveness of riblets was confirmed using unsteady simulation, even under the effects of unsteadiness, it was still possible to achieve a wall shear stress reduction about 4%.

9.2. Future Work

Centrifugal compressor has been a very important and widely studied topic, tremendous efforts have been expended, and the trend will continue. Only a preliminary study has been done in this work due to the limited time (1 year). Further studies are required to devise more methods for improving the centrifugal compressor performance, such as:

- It has been shown that the tip leakage flow induces large amount of losses, in small turbomachinery, it is of particular importance, although it is not possible to be avoided, measures could be taken to weaken it. For example, the application of vortex generator at some specific position could generate possibly beneficial vortex, that may affect the formation path.
- In this preliminary study, the concept of applying riblets on the impeller hub has been exploited to reduce the hub skin friction drag, and thus reduce the associated loss generation. The explicit expression relating maximum wall shear stress reduction to non-dimensional spacing was obtained from a single

set of data, in the future, more data can be collected to have more confidence in the expression, different riblets configurations can also be considered.

- Tiny suction holes may be distributed at/near the leading edge of impeller blade, and connect to slots at the base of impeller blunt trailing edge with a plenum in between. The suction effects may help avoid the appearance of separation bubble near the leading edge, thus reduce the loss generation (a concept very similar to the hybrid laminar flow control technology onboard B787). On the other hand, the jets coming out of these slots may help energize the low momentum fluid at the base of impeller blunt trailing edge, and prompt wake mixing, thus may help reduce the deleterious effects of wake on diffuser performance.

Reference

Acosta, A. J. and Bowerman, R. D., 1957, "A Experimental Study of Centrifugal Pump Impeller", Trans. of ASME, Vol. 79, pp.1821-1839.

Anderson, E. J., Macgillivray, P. S. and Demont, M. E., 1997, "Scallop Shells Exhibit Optimization of Riblet Dimensions for Drag Reduction", Biol. Bull., Vol. 192, pp. 341-344.

Arndt, N., Acosta, A. J., Brennen, C. E. and Caughey, T. K., 1990, "Experimental Investigation of Rotor-Stator Interactions in a Centrifugal Pump with Several Vaned Diffusers", ASME J. Turbomach., Vol. 112, No. 1, pp. 98-108.

Bacher, E. V. and Smith, C. R., 1985, "A Combined Visualization-Anemometry Study of Turbulent Drag Reducing Mechanisms of Triangular Micro-Groove Surface Modification", AIAA Paper, No. 85-0548.

Bechert, D. W., Bruse, M., Hage, W., Van Der Hoeven, J. G. T. and Hoppe, G., 1997a, "Experiments on Drag-Reducing Surfaces and Their Optimization with an Adjustable Geometry", J. Fluid Mech., Vol. 338, pp. 59-87.

Bechert, D. W., Bruse, M., Hage, W. and Meyer, R., 1997b, "Biological Surfaces and Their Technological Application-Laboratory and Flight Experiments on Drag Reduction and Separation Control", AIAA Paper, No. 1997-1960.

Boese, M. and Fottner, L., 2002, "Effects of Riblets on the Loss Behavior of a Highly Loaded Compressor Cascade", ASME Paper, No. GT-2002-30438.

Boncinelli, P., Ermini, M., Bartolacci, S. and Arnone, A., 2007, "Impeller-Diffuser Interaction in Centrifugal Compressors: Numerical Analysis of Radiver Test Case", AIAA J. propulsion Power, Vol. 23, No. 6, pp. 1304-1312.

CD-adapco, 2013, Star CCM+ User Guide Version 8.04.

Cebeci, T. and Carr, L. W., 1978, "A Computer Program for Calculating Laminar and Turbulent Boundary-Layers for Two-Dimensional Time Dependent Flows", NASA Report, No. TM 78470.

Chen, N. X., Papailiou, K. and Huang, W. G., 1999, "Numerical Study on the 3-D Viscous Flow in a Centrifugal Compressor Impeller With and Without Consideration of Tip Clearances", ISABE Paper, No. 99-7223.

Choi, K. S., 1989, "Near Wall Structure of Turbulent Boundary Layer with Riblets", J. Fluid Mech., Vol. 128, No. 11, pp. 417-458.

Choi, H., Moin, P. and Kim, J., 1993, "Direct Numerical Simulation of Turbulent Flow over Riblets", J. Fluid Mech., Vol. 255, pp. 503-539.

Clements, W. and Artt, D., 1989, "The Influence of Diffuser Vane Leading Edge Geometry on the Performance of a Centrifugal Compressor", ASME Paper, No. 89-GT-163.

Coustols, E., 1989, "Behaviour of Internal Manipulators: 'Riblet' Models in Subsonic and Transonic Flows", AIAA Paper, No. 89-0963.

Dean, B. D., 2011, "The Effect of Shark Skin Inspired Riblet Geometries on Drag in Rectangular Duct Flow", Master Thesis, The Ohio State University.

Dean, Jr., R. C. and Senoo, Y., 1960, "Rotating Wakes in Vaneless Diffusers", ASME J. Basic Eng., Vol. 82, No. 3, pp. 563-570.

Denton, J. D., 1993, "Loss Mechanisms in Turbomachines", ASME J. Turbomach., Vol. 115, No. 4, pp. 621-656.

Dixon, S. L. and Hall, C. A., 2010, *Fluid Mechanics and Thermodynamics of Turbomachinery*, 6th ed., Butterworth-Heinemann, Elsevier, USA.

Eckardt, D., 1975, "Instantaneous Measurements in the Jet-Wake Discharge Flow of a Centrifugal Compressor Impeller", ASME J. Eng. Gas Turbines Power, Vol. 97, No. 3, pp. 337-345.

El-Samni, O. A., Chun, H. H. and Yoon, H. S., 2007, "Drag Reduction of Turbulent Flow over Thin Rectangular Riblets", Int. J. Eng. Sci., Vol. 45, pp. 436-454.

Enyuntin, G. V., Lashkov, Y. A. and Samoilova, N. V., 1995, "Drag Reduction in Riblet-Lined Pipes", Fluid Dynamics, Vol. 30, No. 1, pp. 45-48.

Erdos, J. I. and Alzner, E., 1977, "Computation of Unsteady Transonic Flows Through Rotating and Stationary Cascades", NASA Report, No. CR-2900.

Farge, T. Z., Johnson, M. W. and Maksoud, T. M. A., 1989, "Tip Leakage in a Centrifugal Impeller", ASME J. Turbomach., Vol. 111, No. 3, pp. 244-249.

Fransson, T. H., Hillon, F. and Klein, E., 2000, "An International Electronic and Interactive Teaching and Life-Long Learning Platform for Gas Turbine Technology in the 21st Century", ASME Paper, No. 2000-GT-0581.

Garcia-Mayoral, R. and Jimenez, J., 2011, "Drag Reduction by Riblets", Phil. Trans. R. Soci., Vol. 369, pp. 1412-1427.

Gottfried, D. and Fleeter, S., 2002, "Impeller Blade Unsteady Aerodynamic Response to Vaned Diffuser Potential Fields", AIAA J. Propulsion Power, Vol. 18, No. 2, pp. 472-480.

Grek, G. R., Kozlov, V. V. and Titarenko, S. V., 1996, "An Experimental Study of the Influence of Riblets on Transition", J. Fluid Mech., Vol. 315, pp. 31-49.

Hall, K. C., Thomas, J. P. and Clark, W. S., 2002, "Computation of Unsteady Nonlinear Flows in Cascades Using a Harmonic Balance Technique", AIAA J., Vol. 40, No. 5, pp. 879-886.

Hathaway, M. D., Chriss, R. M., Wood, J. R. and Strazisar, A. J., 1993, "Experimental and Computational Investigation of the NASA Low-Speed Centrifugal Compressor Flow Field", NASA Tech. Memo., No. 4481.

Ishida, M. and Senoo, Y., 1981, "On the Pressure Losses due to the Tip Clearance of Centrifugal Blowers", ASME J. Eng. Gas Turbines Power, Vol. 103, No. 2, pp. 271-278.

Ishida, M., Senoo, Y. and Ueki, H., 1990, "Effect of Blade Tip Configuration on Tip Clearance Loss of a Centrifugal Impeller", ASME J. Turbomach., Vol. 112, No. 1, pp. 14-18.

Johnson, M. W. and Moore, J., 1980, "Development of Wake Flow in a Centrifugal Impeller", ASME J. Eng. Gas Turbines Power, Vol. 102, No. 2, pp. 382-390.

Klassen, H. A., Wood, J. R. and Schumann, L. F., 1977a, "Experimental Performance of a 16.10-Centimeter-Tip-Diameter Sweptback Centrifugal Compressor Designed for a 6:1 Pressure Ratio", NASA Tech. , No. X-3552.

Klassen, H. A., Wood, J. R. and Schumann, L. F., 1977b, "Experimental Performance of a 13.65-Centimeter-Tip-Diameter Tandem-Bladed Sweptback Centrifugal Compressor Designed for a Pressure Ratio of 6", NASA Tech., No. 1091.

Koch, C. C. and Smith, L. H., 1976, "Loss Sources and Magnitudes in Axial Flow Compressors", ASME J. Eng Gas Turbines Power, Vol. 98, No. 3, pp. 411-424.

Kolmogorov, A. N., 1942, "Equations of Turbulent Motion of an Incompressible Fluid", Izvestia Acad. of Sci., USSR Phys., Vol. 6, No. 1, pp. 56-58.

Kozlov, V. F., Kuznetsov, V. R., Mineev, B. I. and Secundov, A. N, 1990, "The Influence of Free Stream Turbulence and Surface Ribbing on the Characteristics of a Transitional Boundary Layer", Proc. 1988 Zorian Zaric Mem., *Near Wall Turbulence*, Hemisphere.

Krain, H., 1988, "Swirling Impeller Flow", ASEM J. Turbomach., Vol. 110, No. 1, pp. 122-128.

Launder, B. E., Reece, G. J. and Rodi, W., 1975, "Progress in the Development of a Reynolds Stress Turbulence Closure", J. Fluid Mech., Vol. 3, pp. 269-289.

Launder, B. E. and Spalding, D. B., 1974, "The Numerical Computation of Turbulent Flows", Comput. Methods Appl. Mech. Eng., Vol. 3, pp. 269-289.

Lietmeyer, C., Oehlert, K. and Seume, J. R., 2013, "Optimal Application of Riblets on Compressor Blades and Their Contamination Behaviour", ASME J. Turbomach., Vol. 135, No. 1, 011036.

Lino, T. and Kasai, K., 1985, "An Analysis of Unsteady Flow Induced by Interaction Between a Centrifugal Impeller and a Vaned Diffuser", Trans. of JSME, Vol. 51, No. 471, pp. 154-159.

Litvinenko, Y. A., Chernoray, V. G., Kozlov, V. V., Loefdahl, L., Grek, G. R. and Chun, H. H., 2006, "The Influence of Riblets on the Development of a Λ Structure and Its Transformation into a Turbulent Spot", Doklady Phys., Vol. 51, No. 3, pp. 144-147.

Liu, K. N., Christodoulou, C., Riccius, O. and Joseph, D. D., 1990, "Drag Reduction in Pipes Lined with Riblets", AIAA J., Vol. 28, No. 10, pp. 1697-1698.

Liu, Z. X., Ping, Y. and Zangenen, M., 2013, "On the Nature of Tip Clearance Flow in Subsonic Centrifugal Impellers", Sci. China Tech., Vol. 56, No. 9, pp. 2170-2177.

Mashimo, T., Watanabe, I. and Ariga, I., 1979, "Effects of Fluid Leakage on Performance of a Centrifugal Compressor", ASME J. Eng. Gas Turbines Power, Vol. 101, No. 3, pp. 337-342.

Menter, F. R., 1992a, "Performance of Popular Turbulence Models for Attached and Separated Adverse Pressure Gradient Flow", AIAA J., Vol. 30, No. 8, pp. 2066-2072.

Menter, F. R., 1992b, "Improved Two-Equation k-ω Turbulence Models for Aerodynamic Flows", NASA Tech. Memo., No. TM-103975.

Menter, F. R., 1994, "Two-Equation Eddy Viscosity Turbulence Model for Engineering Applications", AIAA J., Vol. 32, No. 8, pp. 1598-1605.

Menter, F. R., Kuntz, M. and Langtry, R., 2003, "Ten Years of Industrial Experience with the SST Turbulence Model", Proc. 4th Int. Symp. Turbulence, *Heat and Mass Transfer*, Begell House, Redding, CT.

Neumann, D. and Dinkelacker, A., 1991, "Drag Measurements on V-Grooved Surfaces on a Body of Revolution in Axial Flow", J. Appl. Sci. Res., Vol. 48, pp. 105-114.

Nitschke, P., 1983, "Experimental Investigation of the Turbulent Flow in Smooth and Longitudinal Grooved Pipes", Max-Planck Ins. fur Stromungsforschung, Gottingen.

Oehlert, K. and Seume, J. R., 2006, "Exploratory Experiments on Machined Riblets on Compressor Blades", FEDSM Paper, No. 2006-98093.

Pampreen, R. C., 1973, "Small Turbomachinery Compressor and Fan Aerodynamics", ASME J. Eng. Gas Turbines Power, Vol. 95, No. 3, pp. 251-256.

Peric, M., 2004, "Flow Simulation using Control Volumes of Arbitrary Polyhedral Shape", ERCOFTAC Bulletin, No. 62.

Petit, O. and Nilsson, H., 2013, "Numerical Investigations of Unsteady Flow in a Centrifugal Pump with a Vaned Diffuser", Int. J. Rotating Mach., Vol. 2013, ID 961580.

Plamer, D. L. and Waterman, W. F., 1995, "Design and Development of an Advanced Two-Stage Centrifugal Compressor", ASME J. Turbomach., Vol. 117, No. 2, pp. 205-212.

Prandtl, L., 1925, "Bericht Liber Untersungen Zur Ausgebideten Turbulenz", ZAMM, Vol. 5, pp. 136-139.

Rai, M. M. and Madavan, N. K., 1988, "Multi-Airfoil Navier-Stokes Simulations of Turbine Rotor-Stator Interaction", AIAA Paper, No. 88-0361.

Reynolds, O., 1901, *Papers on Mechanical and Physical Subjects*, Vol. 2, Forgotten Books.

Richardson, L., 1922, *Weather Prediction by Numerical Process,* Cambridge University Press, Cambridge.

Rodgers, C., 1982, "The Performance of Centrifugal Compressor Channel Diffusers", ASME 27th Int. Gas Turbine Conf. Ex., London, England.

Rodi, W., 1980, *Turbulence Models and Their Application in Hydraulics-A State of the Art Review*, IAHR, Delft, The Netherlands.

Schlichting, H., 1966, *Boundary Layer Theory*, 6th ed., McGraw-Hill, New York.

Schleer, M., Song, S. J. and Abhari, R. S., 2008, "Clearance Effects on the Onset of Instability in a Centrifugal Compressor", ASME J. Turbomach., Vol. 130, No. 3, 031002.

Sciubba, E., 1994, "Entropy Production Rates as a True Measure of Viscous and Thermal Losses in Thermodynamical Components", NATO Heat & Mass Transfer, Bucharest.

Senoo, Y. and Ishida, M, 1987, "Deterioration of Compressor Performance due to Tip Clearance of Centrifugal Impellers", ASME J. Turbomach., Vol. 109, No. 1, pp. 55-61.

Shapiro, A. H., 1953, *The Dynamics and Thermodynamics of Compressible Fluid Flow*, Wiley, New York.

Shum, Y. K. P., Tan, C. S. and Cumpsty, N. A., 2000, "Impeller-Diffuser Interaction in a Centrifugal Compressor", ASME J. Turbomach., Vol. 122, No. 4, pp. 777-786.

Spalart, P. R. and Allmaras, S. R., 1992, "A One-Equation Turbulence Model for Aerodynamic Flows", AIAA Paper, No. 92-0439.

Storer, J. A., 1991, "Tip Clearance Flow in Axial Compressors", PhD Thesis, Cambridge University, United Kingdom.

Sundaram, S., Viswanath, P. R. and Rudrakumar, S., 1996, "Viscous Drag Reduction Using Riblets on NACA 0012 Airfoil to Moderate Incidence", AIAA J., Vol. 34, No. 4, pp. 676-682.

Sundaram, S., Viswanath, P. R. and Subaschandar, N., 1999, "Viscous Drag Reduction Using Riblets on a Swept Wing", AIAA J., Vol. 37, No. 7, pp. 851-856.

Syed, D. N., Ma, C. C. and Yang, C., 2006, "Numerical Investigation of Tip Clearance Effect on the Stage of a Tamdem-Bladed Centrifugal Compressor for Turbocharger Application", WSEAS Trans. Fluid Mech., Vol.1, No. 6, pp. 720-725.

Tomita, I., Ibaraki, S., Furukawa, M. and Yamada, K., 2013, "The Effect of Tip Leakage Vortex for Operating Range Enhancement of Centrifugal Compressor", ASME J. Turbomach., Vol. 135, No. 5, 051020.

Ubaldi, M., Zunino, P., Barigozzi, G. and Cattanei, A., 1996, "An Experimental Investigation of Stator Induced Unsteadiness on Centrifugal Impeller Outflow", ASME J. Turbomach., Vol. 118, No. 1, pp. 41-51.

Walsh, M. J., 1980, "Drag Characteristics of V Groove and Transverse Curvature Riblets", AIAA Progress in Astro. and Aero., Vol. 72, edited by R. G. Hough, New York, pp. 168-184.

Walsh, M. J., 1982, "Turbulent Boundary Layer Drag Reduction Using Riblets", AIAA Paper, No. 82-0169.

Walsh, M. J., 1983, " Riblets as a Viscous Drag Reduction Technique", AIAA J., Vol. 21, No. 4, pp. 485-486.

Walsh, M. J. and Lindemann, A. M., 1984, "Optimization and Application of Riblets for Turbulent Drag Reduction", AIAA Paper, No. 84-0347.

Walsh, M. J. and Weinstein, L. M., 1978, "Drag and Heat Transfer on Surfaces with Small Longitudinal Fins", AIAA Paper, No. 78-1161.

Wang, S. L., Shi, X. J., Liu, D. and Sun, Q., 2008, "Application Studying of PIV on Groove Drag Reduction Characteristics", ICEM 2008, edited by X. Y. He, H. M. Xie and Y. L. Kang, Proc. of SPIE, Vol. 7375, 737520.

Wilcox, D. C., 1988, "Reassessment of the Scale-Determining Equation for Advanced Turbulence Models", AIAA J., Vol. 26, No. 11, pp. 1299-1310.

Ziegler, K. U., Gallus, H. E. and Niehuis, R., 2003, "A Study on Impeller-Diffuser Interaction Part I Influence on the Performance", ASME J. Turbomach., Vol. 125, No. 1, pp. 173-182.

Appendix A

Comparisons Between Turbulence Models

The prediction of the performance and flow field inside a turbomachine will inevitably involve the turbulence modelling, thus it is of great interest in examining different turbulence models. In this work, three turbulence models were applied to the steady simulation, SA, Realizable k-ε and k-ω SST, respectively.
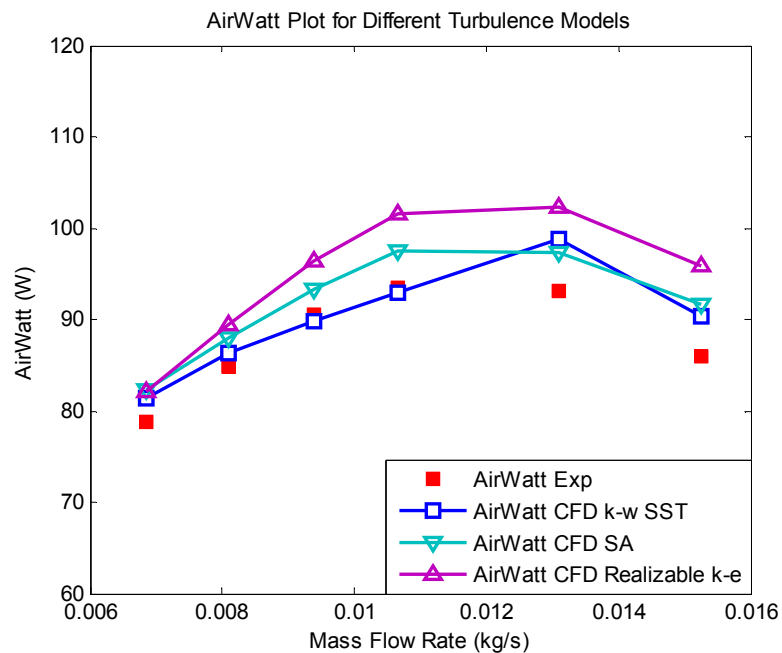

Figure A- 1: AirWatt Plot for different turbulence models.

The performance prediction results are given in Figure A- 1 to Figure A- 3. Good agreements are achieved with the experiment results. As a whole, k-ω SST turbulence model performs slightly better.
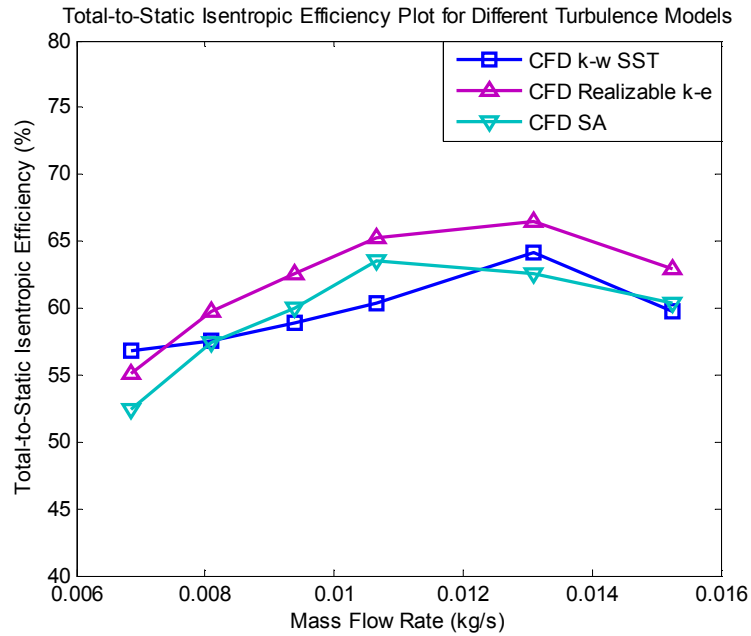
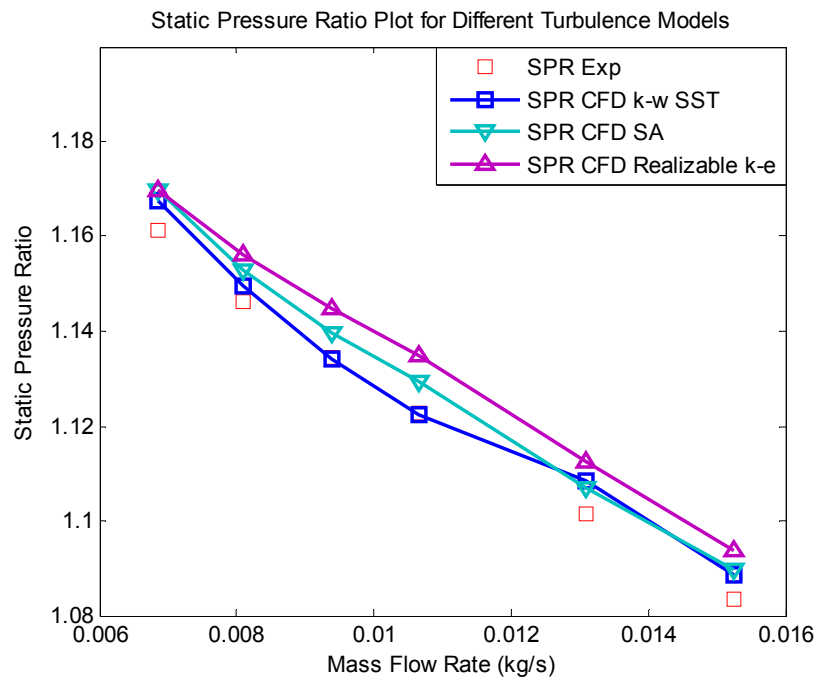Figure A- 2: Total-to static isentropic efficiency for different turbulence models.

Figure A- 3: Static pressure ratio for different turbulence models.

Appendix B

Grid Independence Study

Grid independence study is generally required for assessing the sensitivity of the predicted results with the grid resolution. In this work, grid independence study is conducted for Case 1 with steady simulation. In order to obtain the fine mesh and coarse mesh, the original mesh is doubled and halved, respectively. A summary of the cell count is given in Table B- 1.

		Cell Count	Sum
Coarse	Impeller	290,000	480,000
	Diffuser	190,000	
Medium	Impeller	530,000	900,000
	Diffuser	370,000	
Fine	Impeller	990,000	1,640,000
	Diffuser	650,000	

Table B- 1: Summary of block-structured mesh.

Impeller is the primary concern of the current work, so only results related to impeller are presented here. Figure B- 1 and Figure B- 2 present the static pressure and wall shear stress plots at the impeller hub mid-pitch respectively, computed with different grid resolutions, while the corresponding plots at the impeller blade mid-span are shown in Figure B- 3 and Figure B- 4 respectively. It is observed that the computed results are very close for different grid resolutions. Therefore, the medium resolution grid would be adequate for the current work, and the general flow field results in the next section are obtained with medium resolution grid.
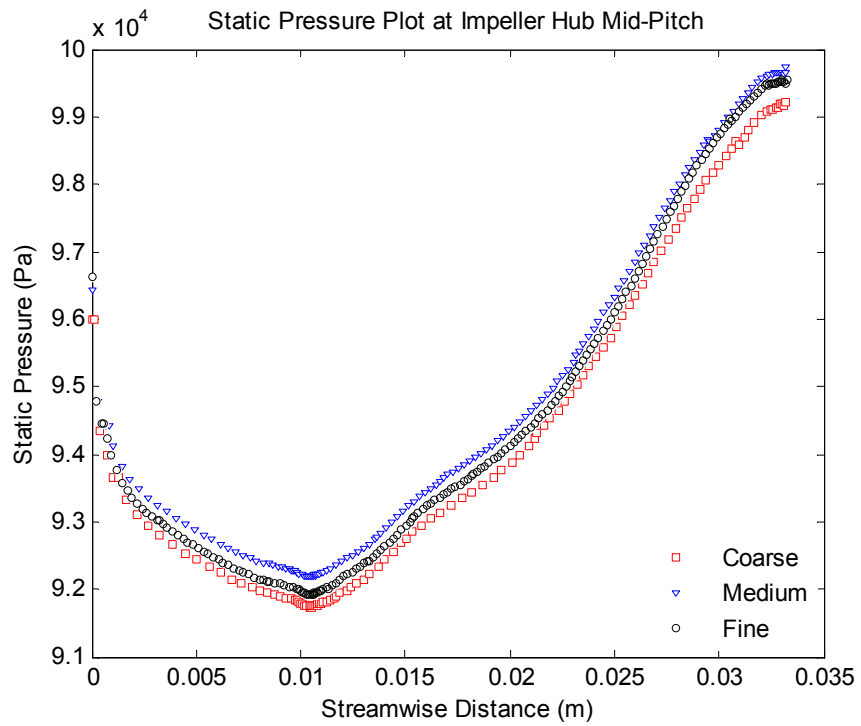
Figure B- 1: Static pressure plot at impeller hub mid-pitch for different grid resolutions.
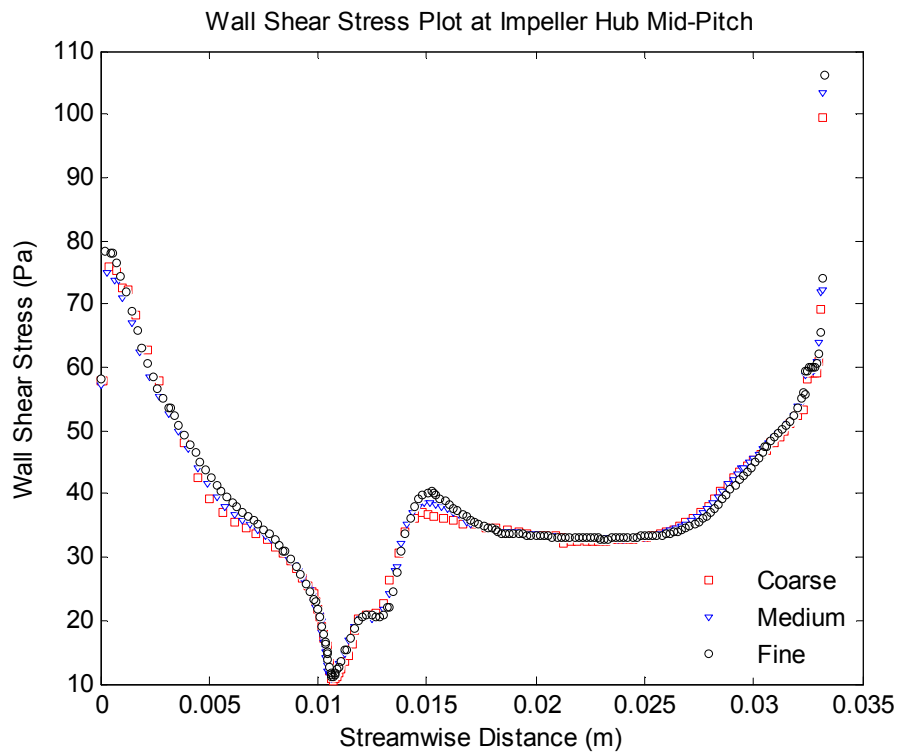

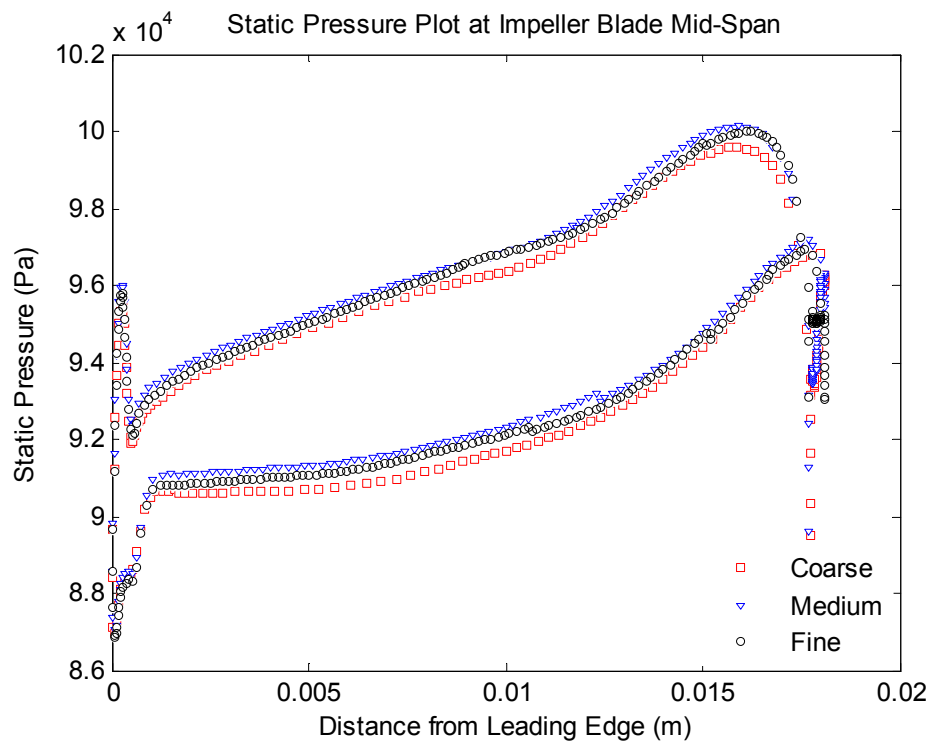Figure B- 2: Wall shear stress plot at impeller hub mid-pitch for different grid resolutions.

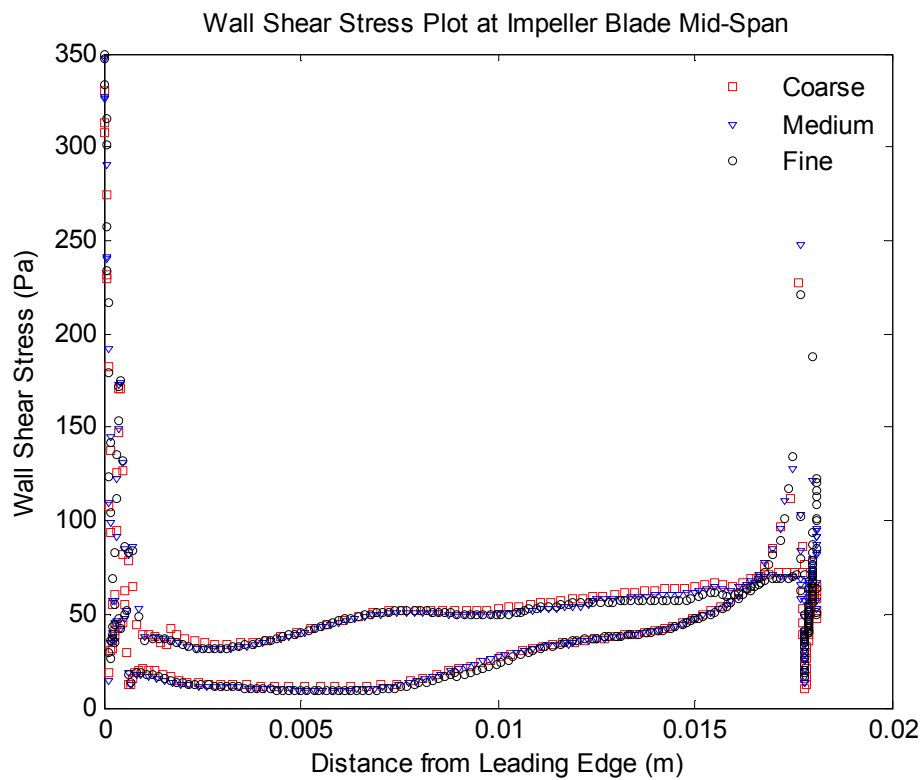Figure B- 3: Static pressure plot at impeller blade mid-span for different grid resolutions.

Figure B- 4: Wall shear stress plot at impeller blade mid-span for different grid resolutions.